HAL
open science

Use of lignocellulosic materials and 3D printing for the elaboration of conductive carbon strutures

Ying Shao

To cite this version:

Ying Shao. Use of lignocellulosic materials and 3D printing for the elaboration of conductive carbon strutures. Materials and structures in mechanics [physics.class-ph]. Université Grenoble Alpes, 2017. English. NNT : 2017GREAI106 . tel-01737416

HAL Id: tel-01737416

https://theses.hal.science/tel-01737416v1

Submitted on 19 Mar 2018

HAL is a multi-disciplinary open access archive for the deposit and dissemination of scientific research documents, whether they are published or not. The documents may come from teaching and research institutions in France or abroad, or from public or private research centers.

L'archive ouverte pluridisciplinaire **HAL**, est destinée au dépôt et à la diffusion de documents scientifiques de niveau recherche, publiés ou non, émanant des établissements d'enseignement et de recherche français ou étrangers, des laboratoires publics ou privés.

Communauté UNIVERSITÉ Grenoble Alpes

THÈSE

Pour obtenir le grade de

DOCTEUR DE LA COMMUNAUTE UNIVERSITE GRENOBLE ALPES

Spécialité : **Matériaux, Mécanique, Génie Civil, Electrochimie**

Arrêté ministériel : 25 mai 2016

Présentée par

Ying SHAO

Thèse dirigée par **Davide BENEVENTI, Directeur de recherche, CNRS,** et **Didier CHAUSSY, Professeur, Grenoble INP**
codirigée par **Philippe GROSSEAU, Directeur de recherche, Ecole des Mines de Saint-Etienne**

préparée au sein du **Laboratoire Génie des Procédés Papetiers (LGP2)**
dans **l'École Doctorale Ingénierie - Matériaux, Mécanique, Environnement, Energétique, Procédés, Production (I-MEP2)**

Utilisation de matériaux lignocellulosiques et du procédé d'impression 3D pour élaborer des structures conductrices

Thèse soutenue publiquement le **29 Septembre, 2017**,
devant le jury composé de :

Mme. Pascaline Pré
Professeur, Ecole des Mines de Nantes, Présidente
M. Sylvain Salvador
Professeur, Ecole des Mines d'Albi, Rapporteur
M. Salaheddine Skali-Lami
Maître de conférences HDR, Université de Lorraine, Rapporteur
M. Davide Beneventi
Directeur de recherche, CNRS, Directeur de thèse
M. Didier Chaussy
Professeur, Grenoble INP, Co-directeur de thèse
M. Philippe Grosseau
Directeur de recherche, Ecole des Mines de Saint-Etienne, Co-encadrant

Abbreviations

A

AM Active material

ASTM American standard test methods

B

BNC Bacterial nanocellulose

C

C Cellulose

CaLS Calcium lignosulfonate

CDCs Carbide-derived carbons

CNT Carbon nanotube

CP Cellulose powder

CVD Chemical vapor deposition

D

DAP Di-ammonium phosphate

DHP Diguanidine hydrogen phosphate

DMA Dynamic mechanical analyzer

DP Degree of polymerization

DTG/DTA Differential thermogravimetric analysis

DS Degree of sulfonation

E

EES Electrical energy storage

F

FTIR Fourier transform infrared spectroscopy

G

GDP Guanidine dihydrogen phosphate

H

H-B Herschel-Bulkley equations

HC Hemicellulose

HRTEM High resolution transmission electron microscopy

HTT Heat treatment temperature

K

KAS Kissinger-Akahira-Sunose equation

K-D Krieger-Dougherty equation

L

L Lignin

LIB Li-ion battery

LS Lignosulfonate

M

MCC Microcrystalline cellulose

MFC Microfibrillated cellulose

MS Mass spectrometry

N

NaLS Sodium lignosulfonate (completed name for LS)

NCC Nanocrystalline cellulose

P

PAN Polyacrylonitrile

PVD Physical vapor deposition

R

RT Room temperature

S

SEM Scanning electron microscope

SSL Spent sulphite liquors

T

TG/TGA Thermogravimetric analysis

X

XRD X-ray diffraction

Table of contents

Introduction 11
1 State of art 15
1.1 Conductive engineering carbon materials& composites: state of art 15
1.1.1 A general introduction to carbon materials 15
1.1.2 Engineering carbon materials 16
1.1.3 Engineering carbons from biomass 17
1.1.4 Applications of engineering carbons in energy storage devices 21
1.2 MFC and LS as bio-carbon precursors: extraction methods, rheological and mechanical properties 24
1.2.1 MFC precursor 24
1.2.1.1 MFC hydrogel elaboration 26
1.2.1.2 Rheological properties of MFC hydrogel 28
1.2.1.3 Mechanical properties of MFC films and composites 30
1.2.2 NaLS precursor 31
1.2.2.1 Production and main properties of NaLS 31
1.2.2.2 Rheological properties of NaLS solutions 33
1.3 Pyrolysis of MFC/LS system and its kinetic modelling 34
1.3.1 A short review of experimental thermoanalytical methods 34
1.3.2 Pyrolysis kinetics 35
1.3.2.1 Biomass pyrolysis kinetic modelling 35
1.3.2.2 Model-free isoconversional method for the estimation of kinetic parameters 37
1.3.3 Pyrolysis of three main components of biomass 39
1.3.3.1 A review of thermal decomposition of cellulose, hemicellulose and lignin39
1.3.3.2 Impacting factors for biomass kinetics: environmental components and ash content 43
1.3.3.3 Improvement of conductive carbon production during pyrolysis 44
1.4 Microstructural and electrical conductivity evolution of biomass during pyrolysis . 46
2 Materials and methods 50
2.1 Materials: 50
2.2 Solution preparation 50
2.3 Rheological tests 51

2.4 Forming methods of MFC/LS and MFC/LS/CP carbon precursors 51
2.4.1 Casting followed by air drying 51
2.4.2 3D printing followed by air drying or freeze drying 52
2.5 Pyrolysis and its thermal characterization 53
2.5.1 Pyrolysis 53
2.5.2 Thermal characterization by TG/MS 53
2.5.3 Kinetic analysis 53
2.6 Characterization of carbonaceous chars 55
2.6.1 Microscopies 55
2.6.2 Fourier transform infrared spectroscopy 55
2.6.3 X-ray tomography 55
2.6.4 Electrical conductivity measurement 55
2.6.5 Density measurements 55
2.6.6 Raman spectrometry 56
2.6.7 X-ray diffraction 56
2.6.8 Mechanical characterization 57
3 Experimental results 59
3.1 Use of MFC/LS blends as carbon precursors: impact of hydrogel rheology on 3D printing 59
3.1.1 Introduction 59
3.1.2 Pure LS/water solutions of different concentrations 59
3.1.3 Pure MFC hydrogels of different concentrations 60
3.1.4 MFC/LS slurries of different concentrations 62
3.1.5 Thixotropy of mixed slurries 64
3.1.6 Relationship between the rheology and hydrogel printing 65
3.1.7 Characterization of printed aerogels before and after pyrolysis 66
3.1.8 Conclusions 68
3.2 Use of MFC/LS blends as carbon precursors: pyrolytic process characterization and kinetics study 70
3.2.1 Introduction 70
3.2.2 Morphological and structural characterization 70
3.2.3 Thermal characterization 72
3.2.4 Catalytic effect of sodium 73

3.2.5 Pyrolysis gas analysis by mass spectrometry (MS) 75
3.2.6 Kinetic analysis 76
3.2.6.1 Estimation of activation energies by KAS isoconversional method 76
3.2.6.2 Kinetic triplets provided by model-fitting method 78
3.2.6.3 Comparison between isoconversional and model-fitting methods 79
3.2.6.4 Kinetic analysis of MFC/NaLS composites 80
3.2.7 Conclusions 81
3.3 Use of MFC/LS blends as carbon precursors: characterization of MFC/LS carbons 82
3.3.1 Introduction 82
3.3.2 Morphology of MFC/LS sheet before and after pyrolysis 82
3.3.3 Chemical characterization by FTIR 83
3.3.4 Density evolution 84
3.3.5 Electrical conductivity evolution 85
3.3.6 Microstructural evolution 86
3.3.6.1 Raman analysis 86
3.3.6.2 XRD analysis 89
3.3.7 Discussion 91
3.3.7.1 Development of electrical conductivity during pyrolysis: impact of porosity 91
3.3.7.2 Development of electrical conductivity during pyrolysis: impact of microstructures and HTTs 91
3.3.7.3 Comparison of biocarbons from various precursors in terms of electrical property 93
3.3.8 Conclusions 94
3.4 Optimization of the formulation of carbon precursors for 3D printing and carbon quality 96
3.4.1 Introduction 96
3.4.2 Rheological properties of MFC/LS/CP hydrogel 96
3.4.3 Macro- and micro-morphology of MFC/LS/CP precursor and the resulting carbons 97
3.4.4 Analysis of pyrolytic process of MFC/LS/CP composite 98
3.4.5 Characterization of MFC/LS/CP carbons 100
3.4.5.1 Density evolution 100

3.4.5.2 Microstructural evolution 102
3.4.5.3 Electrical conductivity 102
3.4.5.4 Mechanical properties 103
3.4.6 Conclusions 105
4 Conclusions and perspectives 107
5 References 110
6 Appendices 123
A: Elemental analysis data of the used NaLS 123
B.Elemental analysis data of MFC 123
7 Published/submitted papers 125
8 French abstract 127

Introduction

Introduction

The increasing concerns about the environmental issues are promoting the use of renewable and environmentally-friendly materials in all domains. As the most abundant polymer resources in nature, lignocellulosic materials, such as cellulose and lignin, have attracted special attention nowadays for being widely used in medical, packaging, construction and energy industries. In energy storage domain, carbon materials have been considered as ideal candidates for electrode materials owing to their high specific surface area (>2000m^2g^{-1}), high electrical conductivity, good charge-discharge stability and good corrosion resistance[1]. However, in order to achieve the advantages mentioned before, "noble" carbon precursors, such as carbon nanotube and graphene, are used whose production is quite complex and expensive. In such context, this work examined the use of biomass-derived engineering carbons as active material in energy storage devices. Engineering carbons are commercial and green carbons that are elaborated using a one-step pyrolysis from organic precursors[2].

Biomass-derived carbons have been used as active carbon in a wide range of applications, including soil improvement[3], pollutant removal[4], greenhouse gas emission reduction[5], *etc.*, thanks to their high specific surface area and low cost[3,4]. Its use as active electrode material, as was investigated in the current thesis, was inspired by Perepelkin[6] who summarized an electrical resistivity decrease of nearly 12 magnitudes for biomass precursor heat-treated at 350°C and 950°C, despite the fact that biomass has been considered as non-graphitizing carbon precursor. More recently, some researchers have successfully elaborated electrodes using such bio-carbons that lead to a good cycling performance[7–9]. Nevertheless, no further interpretation concerning the development of electrical conductivity during pyrolysis was given for biomass-derived carbons.

Among various lignocellulosic materials, microfibrillated cellulose (MFC) and lignosulfonate (LS) have caught special attention for the elaboration of carbon precursor composites[10,11]. MFC are released from cellulose fibers via mechanical treatments with potential chemical treatment[12]. Thanks to their microscopic dimensions, MFC form a network with strong strength[13]. LS is a water-soluble polymer composed of a large quantity of cross-linked aromatic cycles[14]. It is an industrial byproduct from the production of wood pulp using sulfite pulping. The composites elaborated from MFC/LS slurries are self-standing with MFC playing a role as mechanical reinforcement whereas LS ensures the carbon yield after pyrolysis[15,16]. However, in the frame of this work that is to use 3D printing as forming method, it was revealed in a previous work[15] that add of LS into MFC hydrogels lead to either a disruption of the hydrogels' stability after 3D printing due to lack of viscosity(with 10%-30% LS), or a loss of shape definition because of the long restauration time(with 50% LS). Since LS is an essential component to the composite due to its large contribution to the carbon yield[16] that is important to ensure the thermal stability and conductivity of as-elaborated bio-carbons, one solution to improving the hydrogels' printability while keeping using large

quantity of LS in the formulation is to add appropriate additives. In the aim of using bio-sourced materials in this work, cellulose powder (CP) was chosen.

This thesis not only characterized the carbons obtained from MFC/LS/CP precursor in terms of conductivity, microstructure, density as a function of pyrolysis temperature, but also correlated 3D printing to the composite formation from its hydrogel form. Filament-based 3D printing technic was used as the principal forming method for elaborating MFC/LS/CP carbon precursor, owing to the fact that all pristine materials are water-processable and could form appropriate hydrogel for printing. The interest of using 3D printing in this work mainly consists in its flexibility to produce samples in various forms and dimensions in order to meet different characterization purposes. For instance, as the simplest form, monolines were printed only for tensile tests. More excitingly, electrodes could be directly printed using a two-head printer with one head firstly printing a web-like structure then another filling the web holes with other types of hydrogel (probably electrochemistry-strengthen components). As a result, 3D printing not only amplifies the potential applications of MFC/LS/CP as a printable hydrogel but also proposes an unexplored way to elaborate electrodes of next generation.

The present work is divided in 4 experimental sections:

Section 1 studied the rheological properties of MFC/LS hydrogels and their relationship with the printability and stability after 3D printing. This study aims at optimizing the formulation of MFC/LS hydrogel in order to manufacture hydrogel samples that are morphologically stable after 3D printing. Besides, drying method (air drying or freeze drying) was also optimized according to the printing results of MFC/LS hydrogels of different concentrations.

Section 2 worked on the analysis of the thermal degradation of MFC/LS composites as well as their decomposition kinetics. Since pyrolysis is the critical process that transforms carbon precursors to real carbons, it is essential to investigate the reactions that occur in each component during such process.

Section 3 characterized the bio-carbons of MFC/LS as a function of heat treatment temperatures (HTT) since the latter plays a decisive role in carbons' physicochemical properties, including density, electrical conductivity, microstructure, *etc.*

Section 4 summarized the methods and conclusions of the 3 previous sections and examined the use of MFC/LS/CP as carbon precursors. CP was included in the hydrogel formulation in order to improve the printing results of MFC/LS that were summarized in section 1. The thermal characterization of MFC/LS/CP composite was repeated as was described in section 2. Moreover, biocarbons of MFC/LS/CP were characterized and compared to those of MFC/LS (section 3).

The 4 sections correspond to 4 published (or submitted) papers that are listed in Chapter 7.

This PhD thesis was carried out principally in Laboratory of Pulp and Paper Science and Graphic Arts (LGP2) in Grenoble, France. It is also in collaboration with SPIN (Center for Chemical Engineering) in Saint-Etienne, France. The experimental work done during this thesis is schematically illustrated in the figure below:

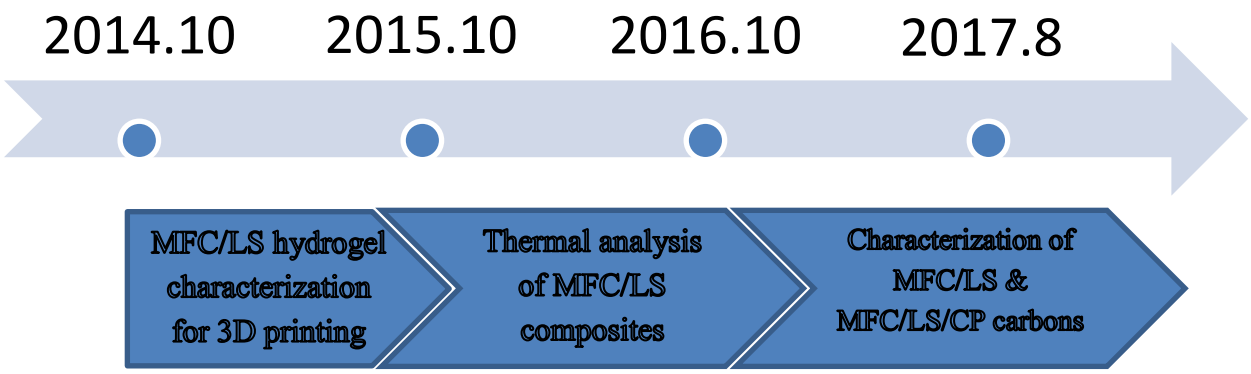

1. State of art

1 State of art

1.1 Conductive engineering carbon materials& composites: state of art

1.1.1 A general introduction to carbon materials

Carbon is one of the most abundant elements on earth and the utilization of carbon materials began at the prehistoric age when charcoal was first introduced. From literature, no clear definition of "carbon materials" is found. A generally accepted concept for "carbon materials" is that they refer to materials composed predominantly of carbon, irrespective of their structure. According to different criteria, carbon materials can be divided in different categories. In terms of atomic arrangement, carbons, like diamond, graphite and fullerenes, *etc.*, form an ordered (poly-) crystalline structure while others are more-or-less disordered or even amorphous, including engineering carbons and carbon films manufactured by PVD or CVD[2]. In terms of chronological development of carbon-based materials, there are classic carbons (period I), new carbons (period II) and nanocarbons (period III) (Fig 1.1.1). Since the first report of fullerenes in 1985, carbon-based nanomaterials[17], including carbon nanotubes (CNTs) and graphene, have been largely developed for the applications in catalyst supports, adsorbents and energy storage compounds owing to their excellent physical and electrochemical properties.

Period	Years	Carbon materials developed	Remarks
I	–1960	Artificial graphite blocks Activated carbons Carbon blacks Natural diamond	Mass production Sale in either tons or kilograms
II	1960 – 1985	Various carbon fibers Glass-like carbons Pyrolytic carbons High-density isotropic graphites Intercalation compounds Various composites (CFRP, CFRC, *etc.*) Synthetic diamond Diamond-like carbons	Introduction of various techniques for the production of carbon materials (*e.g.*, CVD, composite with other materials, *etc.*) Developments of new applications Sale mostly in grams
III	1985 –	Fullerenes Carbon nanotubes	Nano-sized Sale in milligrams

Fig 1.1.1 The chronology of the development of carbon materials (copyright of Michio et.al.[18])

The thermal expansity, electrical and mechanical properties as well as bulk density of different forms of carbon (except nanocarbons) vary in a rather wide range, as listed in Fig 1.1.2. It appears that graphite and its intercalation compounds have a comparable electrical conductivity to metals but much lighter weight, which explains their wide use as electrode materials. Some of pyrolytic carbons, such as PAN-based and pitch-based carbon fibers, compose of a quite porous structure, which may be a good candidate for solving the shape

stability and cycling performance problems for electrode host materials during charging/discharging. Moreover, materials made of synthetic carbon fibers and their composites have been currently employed in vehicles and bicycles for the sake of reducing total weight while remaining adequate stiffness, which accounts for the decrease of fuel consumption and manpower for driving them[19].

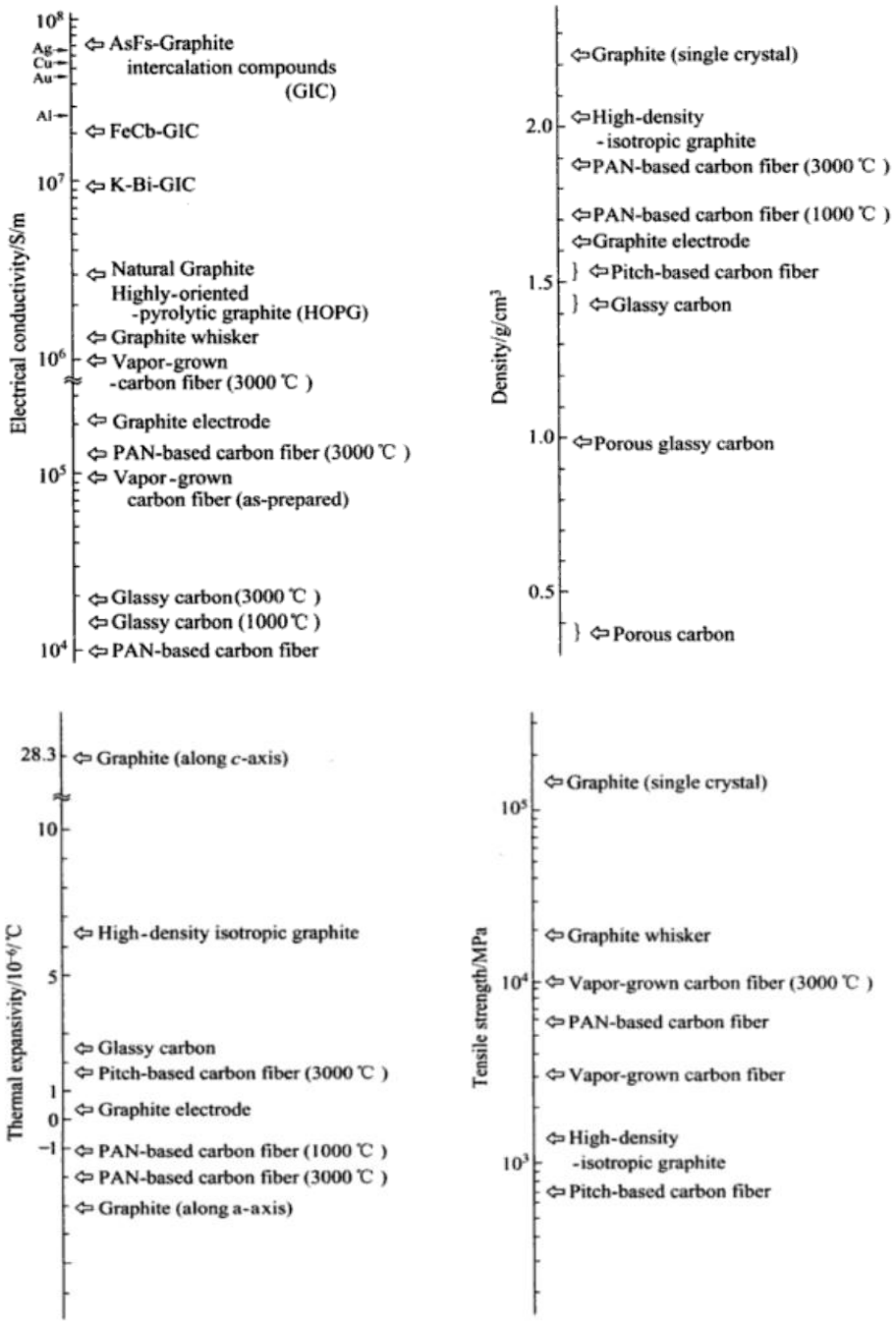

Fig 1.1.2 Properties of different forms of carbon (copyright of Michio et.al.[18])

1.1.2 Engineering carbon materials

The major topic in the present work is engineering carbons. Generally, they have more or less disordered graphitic or even amorphous microstructures. In spite of excellent physical,

chemical and structural characters that (poly-) crystalline carbons possess, engineering carbon materials are still the most commonly used in the industry and in everyday life owing to their easier manufacturing method, lower costs of raw materials and production process.

Most of engineering carbons are derived from organic precursors by heat treatment in inert atmosphere (called also carbonization process). The precursors for engineering carbons and the corresponding products are listed in Fig 1.1.3.

Primary precursor	*Secondary precursor*	*Example products*
Hydrocarbon gases		pyrocarbons, carbon blacks, vapour grown carbon fibres, matrix carbon[a]
Petroleum		delayed coke, calcined coke
	petroleum pitch	needle coke, carbon fibers, binder and matrix carbon[a]
	mesophase pitch	mesocarbon microbeads, carbon fibers
Coals		semi-coke, calcined coke
	coal chars	activated carbons
	coal tar pitch	premium cokes, carbon fibers, binder and matrix carbons[a]
	mesophase pitch	mesocarbon microbeads, carbon fibers
Polymers	polyacrylonitrile	PAN-based carbon fibers
	phenolic and furan resins	glassy carbons, binder and matrix carbons[a]
	polyimides	graphite films and monoliths
Biomass[b]		activated carbons

a. precursor for binder in polygranular carbons and graphites, precursor for matrix in carbon-carbon composites; b, especially wood and nutshells

Fig 1.1.3 A list of precursors for engineering carbon materials (copyright of Burchell et.al[2])

1.1.3 Engineering carbons from biomass

Among the above precursors, biomass, mainly wood components, has caught special attention these years for the synthesis of valuable carbon materials since it is an environmental friendly and renewable resource and is highly available in nature. Bio-sourced carbonaceous materials are mainly derived from three structural components of wood: cellulose, hemicellulose and lignin. The content of each component in wood cell walls depends on the wood sources and varies between 40%-45% for cellulose, 25%-35% for hemicellulose and 20%-30% for lignin[20]. Morphologically, wood cell wall is a complex laminate structure, which could be divided into three different zones: the middle lamella, the primary cell wall and the secondary cell wall (including s1, s2 and s3, as schematically illustrated in Fig 1.1.4). The secondary cell wall is a major consideration for biosynthesis since it contains the main quantity of cellulose and besides, lignin is nearly not detected in two other zones[21]. The three different layers in the secondary cell wall could be easily distinguished in an ultrastructural scale by the differences in the orientation of cellulose microfibrils. Irrespective of layers in the secondary cell wall zone, each wood component plays a crucial role to constructing the strength of cell wall: cellulose works as the framework substance; hemicellulose is the matrix material cross-linking cellulosic and non-cellulosic polymers; and lignin is the encrusting matter[22], as is described in both longitudinal and transversal senses in Fig 1.1.5.

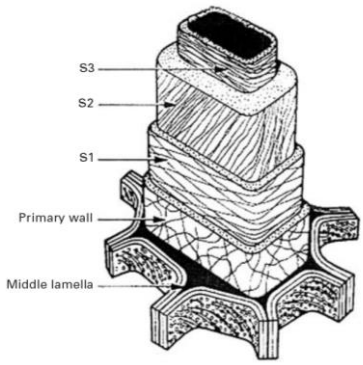

Fig 1.1.4 Illustration of cell wall structure of wood fibers (copyright Barnett *et al.*[23])

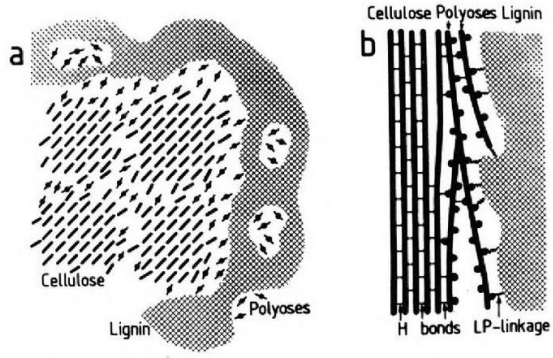

Fig 1.1.5 Schematic diagram for the ultrastructural arrangement of cellulose, hemicellulose (polyoses) and lignin in the wood cell wall: a) transversal section; b) longitudinal section (copyright of Higuchi et.al.[22])

Early in 1838, Anselme Payen declared the discovery of a "resistant fibrous solid" after a series of acids and ammonia treatments of plant tissues. Shortly after that, cellulose was used to name this plant constituent whose molecular formula was determined to be $C_6H_{10}O_5$.[24] As is demonstrated in Fig 1.1.6, from the right to the left, a cellulosic fiber (essentially a part of cell wall) is regarded as a bundle of microfibrillated cellulose (wrapped outside by HC and possibly lignin), each of which is also an alongside package of several elementary fibrils (or microfibrils)[22]. Along each microfibril, there is an alternation of crystalline regions and amorphous parts. The crystallinity of cellulose has been studied for years and is assigned to be cellulose chains assembling where a strong and complex network of hydrogen bonds acts as intra- and intermolecular connections[25,26]. Besides, a disordered part has been proved to co-exist and link with the ordered ones. Unlike crystalline regions, the nature and the mechanism of disordered parts of cellulose microfibrils have not been clearly suggested yet[27,28].

Fundamentally, cellulose is a glucan polymer consisting of linear chains of 1,4-β-bonded anhydro-D-glucose units, as it shows in Fig 1.1.6. Each unit is corkscrewed 180° with respect to its neighbors, and the repeated segment is frequently taken to be a dimer of glucose, known as cellobiose. Three hydroxyl groups are owned by one single glucose unite, ensuring its ability to form strong and multi-scale hydrogen bonds in microfibril structure. Furthermore,

the frequent existence of –OH groups imparts cellulose with other characteristic properties such as hydrophilicity, chirality, degradability and chemical variability. The number of glucose units in one cellulose molecular chain (called also polymerization degree, DP) varies depending on wood sources and the selection of sample locations. According to the measurements conducted by Goring et. al.[29] using light-scattering techniques, native cellulose has an average DP ranging from 9000 to 15000 and a DP of 10000 means a linear chain length of approximately 5 μm in wood. In terms of transversal dimensions, an elementary fibril of about 5 nm could contain approximately 40 cellulose chains[22] whereas the microfibrillated cellulose has diameters ranging from 20 to 50 nm[12].

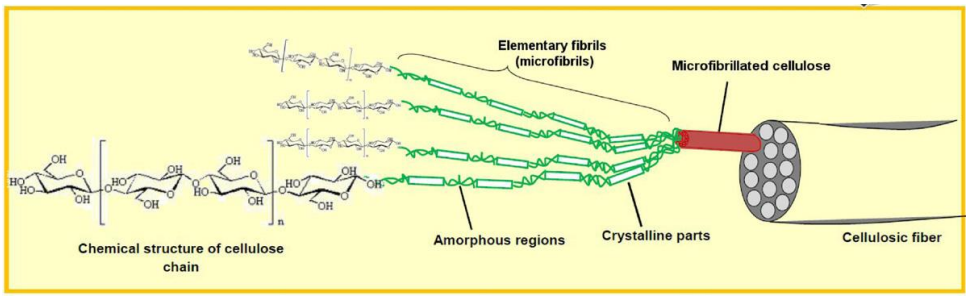

Fig 1.1.6 The hierarchy structure of cellulose(from the right to the left): from macroscopic cell wall fibers to microscopic chemical molecular formula (copyright Lavoine *et al.*[12])

Hemicelluloses are mixtures of polysaccharides[30] that occur in close association with cellulose and lignin in the secondary cell wall of wood fiber. They differ from cellulose by the composition of their sugar units, the length of chain and branching of the chain molecules[21]. The content of polysaccharides in hemicellulose differs from species to species but is structurally divided into four general types[31]: Xylans, Mannans, Xyloglucans and Mixed-linkage β-glucans, all of which occur in many structural variations differing in side chain types, localization and distribution of glycoside linkages in the main macromolecular chain. Generally, HC has a lower molecular weight than cellulose as well as a lower chemical and thermal stability, probably due to lack of crystallinity and lower polymerization degree[21]. HCs occur in nature having also 3 hydroxyl groups per chain unit, but unlike cellulose, they are soluble in alkali and easily hydrolyzed by acids.

Lignin is a phenolic substance consisting of an irregular array of variously bonded hydroxyl- and methoxyl-substituted phenylpropane units[30]. Henriksson *et al.* firstly proposed a general molecular formula of spruce lignin, presented in Fig 1.1.7. In contrast to cellulose which is a linear polymer, lignin has a complex and three-dimensional structure and is formed by polymerization of monolignols whose type depends on plant species. In coniferous wood, lignin is built up almost exclusively by coniferyl alcohol (G-units) with a minor presence of coumaryl alcohol (H-units), although the latter is a major constituent in compression wood lignin. In hard woods, both G-units and sinapyl alcohol (S-units) are used as building blocks whereas in monocotyledonous tissue, all these three alcohols are used as lignin precursors. Fig

1.1.8. presents the three major monolignols. In lignin network, they are mutually cross-linked by different ether and carbon-carbon bonds[20].

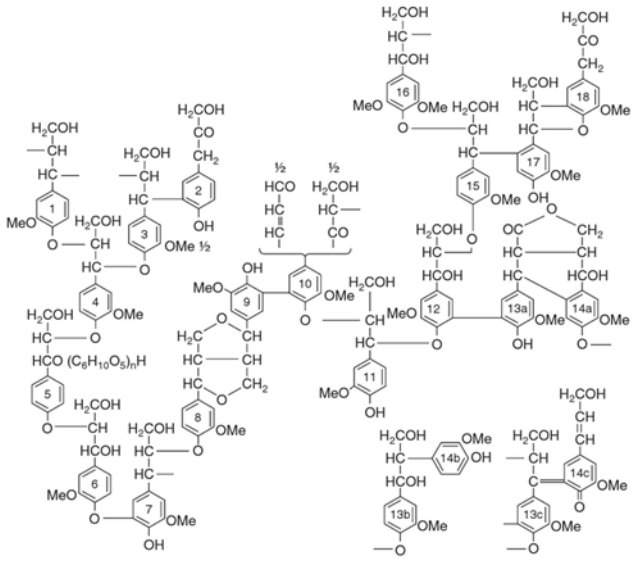

Fig 1.1.7 A general formula of spruce lignin, proposed by Henriksson *et al.*, shows the most important inter-unit linkages between the phenylpropane units. (copyright Belgacem and Gandini[32])

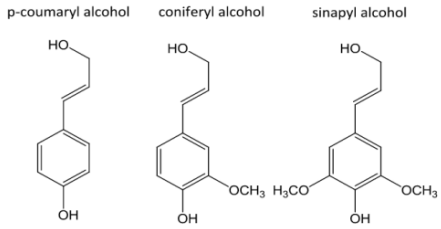

Fig 1.1.8 Schematic illustration of the three main precursors of lignin (copyright : thesis of Ida Norberg[20])

Lignin has been seen as a promising carbon fiber precursor recently owing to its high carbon content (over 60%, with respect to only 44% (theoretically) for cellulose precursor), aromatic macromolecule morphology in addition to its comparably high abundance in nature (second to cellulose). The production of carbon fibers from lignin has been reported in several works[33,34] including a complete process from raw materials' treatment to the final carbonization.

Several synthesis methods, such as pyrolytic carbonization, hydrothermal carbonization, high-voltage arc electricity, laser ablation, have been reported for preparing amorphous carbonaceous materials from the above biomass components with different shapes (single fiber or fibrous web), dimensions and applications[35]. Herein, pyrolysis (pyrolytic carbonization) is chosen as the main method for synthesizing bio-sourced carbon materials due to its relatively simple facilities and low-costs. At early stage of pyrolysis (200°C <T<600°C), cyclization and aromatization proceed in the organic precursor with the release of

various organic compounds like hydrocarbons, and inorganic matters such as CO, CO_2, H_2O, mainly because some of the C-C bonds are weaker than C-H bonds. Over 600°C, out-gassing is typically H_2 due to the polycondensation of aromatics. Up to 1500°C, the residues which have "suffered" from carbonization may be called carbonaceous solids though they might still contain hydrogen. Above 1500, graphitization begins so the residues contain more than 99% of C which are thus called carbon materials[6]. The occurrence of reactions, including cyclization, aromatization, polycondensation and carbonization, depends strongly on the organic precursors as well as heating conditions. Sometimes these processes overlap with each other throughout pyrolysis and therefore, the whole process from precursor to the final carbon residues is often simply called "the carbonization". A general schema of carbonization process is provided by Michio *et al.* (Fig 1.1.9).

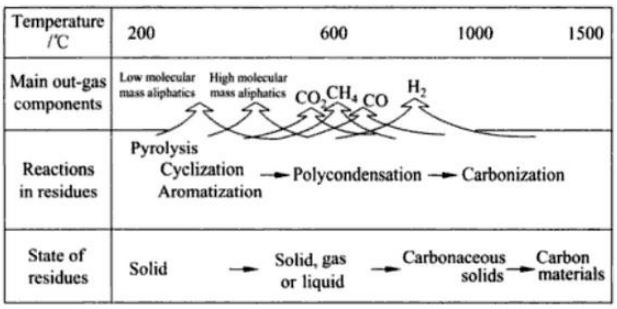

Fig 1.1.9 Schema of carbonization process (copyright Michio *et al.*[18])

1.1.4 Applications of engineering carbons in energy storage devices

With the increasing demand for portable electronic devices and electrical vehicles, rechargeable Lithium –ion batteries (LIBs) have received special attention nowadays among the electrical energy storage devices due to their relatively high capacity, fast charge-discharge rate and light weight[9,36] compared to conventional Ni-Cd batteries and Ni metal hybrid cells. A comparison of currently used electrical energy storage (EES) technologies is presented in terms of volumetric and gravimetric energy density[37] (Fig 1.1.10a)) as well as discharge time and power rating[38] (Fig 1.1.10b)).

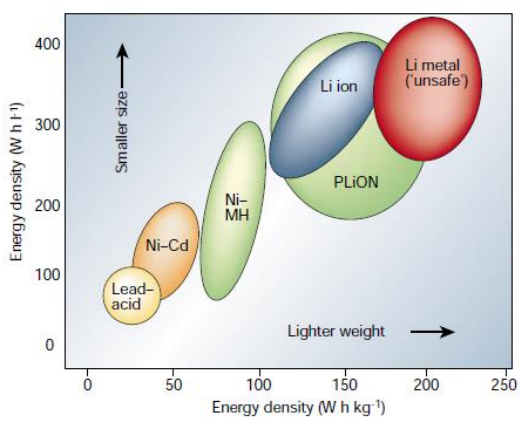

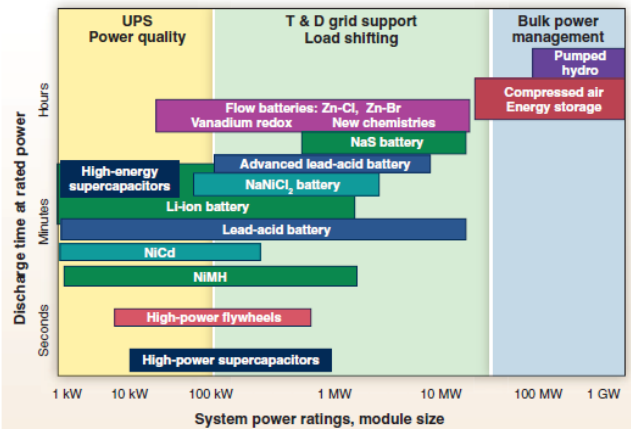

Fig 1.1.10 Comparison of EES technologies in terms of: a) volumetric and specific energy density; b) discharge time and power rating

Among the EES devices, batteries, especially secondary LIBs, are found to occupy the most application market and attract a large number of investments for fundamental and applied research. A battery consists of numerous cells which are connected with each other in series or in parallel in order to provide required capacity and voltage. Each cell is composed of one anode and one cathode usually immerged into a liquid electrolyte. Li-ion battery cells employ lithium intercalaction compounds as positive and negative electrodes materials in which the electrical energy conversion between charge and discharge is realized by means of electrochemical oxidation-reduction (redox) reaction. Commonly used materials for both electrodes and the electrolyte are concluded in Fig 1.1.11[39]. Carbon materials, whether graphitic or not, are currently used as anode active material owing to a better cycling performance and structural stability compared to Li metals or alloys. The materials for the positive electrode are typically metal oxides of Lithium with either a layered structure, like $LiCoO_2$ or a tunneled structure, such as $LiMn_2O_4$[40,41]. The active materials are coated onto a current collector, normally a metal foil, with a fluorinated polymer binder and an electronic conductivity enhancer, typically a high surface area carbon black, to form a "sandwich" structure. The electrolyte, which is liquid and made of Li salt dissolved into an organic solvent, ensures the transfer of Li ions between the anode and the cathode in the cell. The charge-discharge process during which the electrochemical reactions take place in both anode and cathode is well demonstrated in Fig 1.1.12. When on charge, an external electrochemical force is applied, which promote the decomposition (oxidation) of positive electrode material into Li ions and compensation electrons. The Li ions then de-intercalate from cathode and "travel" through Li salt electrolyte by ion exchange before intercalating into anode material. Meanwhile, the compensation electrons travel in the external circuit and are received by the anode to finish the reduction reaction. Fig 1.1.13 formularizes the reaction in each electrode as well as the overall process. The discharge reverses the reactions and the electrons pass through external circuit from anode to cathode to provide energy power for electronic devices.

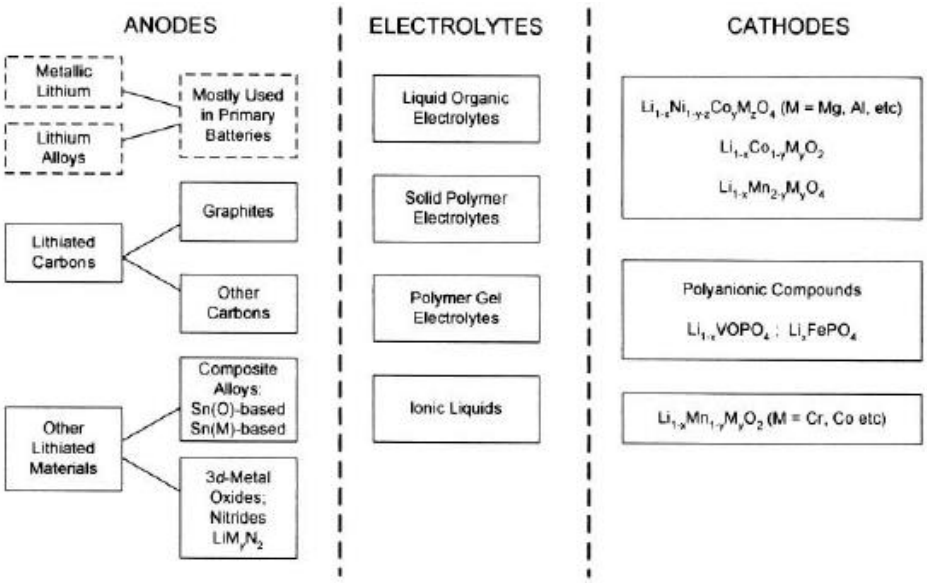

Fig 1.1.11 Choice of materials for anode, cathode and electrolyte of LIBs

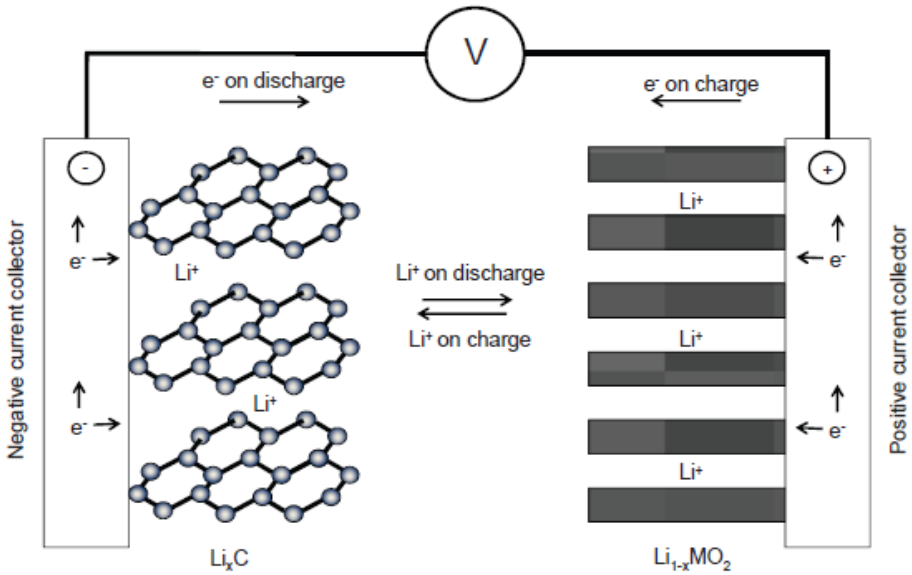

Fig 1.1.12 Charge-discharge process in a LIB cell

Positive electrode

$$LiMO_2 \underset{\text{discharge}}{\overset{\text{charge}}{\rightleftharpoons}} Li_{1-x}MO_2 + xLi^+ + xe^-$$

Negative electrode

$$C + xLi^+ + xe^- \underset{\text{discharge}}{\overset{\text{charge}}{\rightleftharpoons}} Li_xC$$

Overall cell

$$LiMO_2 + C \underset{\text{discharge}}{\overset{\text{charge}}{\rightleftharpoons}} Li_xC + Li_{1-x}MO_2$$

Fig 1.1.13 Reactions in both electrodes and the overall cell during charge-discharge

Based on the electrochemical reactions in a LIB cell, a promising electrode material should conform to several requirements: i) the ability to receive and de-intercalate a large amount of Li ions in a short time to ensure the capacity and energy density of the battery cell; ii) no obvious change of the electrode's volume or form during the intercalation and de-intercalation of Li ions, which promises its structural stability and safety; iii) the previous reaction of Li ions with the active material does not prohibit it from accepting latterly arrived Li ions, in order to ensure the cycling performance and a long service life. Furthermore, the increasing demand for energy consumption from the contemporary society accompanied nevertheless by limited CO_2 emission requires the development of renewable electrode materials to manufactory more efficient and more environmental-friendly LIBs. Moreover, it would be

better if the complicated "sandwich" structure of conventional electrodes (active material (AM)- binder- metallic current collector) could be reduced for the purpose of smaller and lighter LIBs but with the ensured conductivity and efficiency.

Among the negative electrode materials listed in Fig 1.1.11, carbonaceous materials are believed to be the most appropriate choice for several reasons. First of all, lithium insertion into carbon leads to binary phases LiC_x, which are close to equilibrium whereas its intercalation into metal oxides yields often ternary non-equilibrium state Li_xMO_n, which will then decompose to electrochemical inactive matters.[42] Secondly, although metallic Lithium and Li-alloys exhibit extremely high redox potential, their corrosion problems and dendrite formation with liquid electrolyte have become a major concern for the safety and cycle life of LIBs. However, carbonaceous materials overcome such problems since they are usually electrolyte-inert with a redox potential close to metallic Li. In addition, carbon materials, no matter graphitic or not, naturally have certain controlled porosity, depending on carbon sources and carbonization processes, which offers adequate room for the insertion de-intercalation of Li ions without huge volumetric change. Moreover, bio-sourced carbon materials have been studied for years, which could provide a possible solution for manufacturing renewable LIB electrodes.

The present thesis aims at adopting pyrolytic wood derivatives (*i.e.* derivatives of cellulose or lignin) as electrode host materials.

1.2 MFC and LS as bio-carbon precursors: extraction methods, rheological and mechanical properties

Within the purpose of producing porous and self-standing conductive bio-carbons, two mains constitutional materials are used in the course of the current thesis, both of which are wood derivatives: microfibrillated cellulose (MFC) and sodium lignosulfonate (NaLS). The reasons for them to be chosen are multiple. Firstly, as mother materials to MFC and NaLS, cellulose is the most abundant carbon source in nature and lignin ranks only second to it. Secondly, synthesis methods of carbon fibers from cellulose and lignin precursor are accessible in current literature. Furthermore, composites made of MFC and LS, regardless of forming methods, are self-standing and functional in which MFC fibers constitute a web-like reinforcement whereas NaLS serves as surrounding matrix and contributes mostly to the carbon yield after pyrolysis. In terms of forming process, both MFC and NaLS are water-processable, which makes it easier to produce MFC/LS composites by simply following a molding /shaping step (like casting, 3D printing, *etc.*) and the subsequent drying step (air drying, oven drying, or freeze drying). In the following paragraphs, not only the extraction protocols of MFC and NaLS will be introduced, but also their rheological properties in suspension state as well as the mechanical properties of dried MFC will be discussed.

1.2.1 MFC precursor

Currently, novel isolation methods make it possible to manufacture cellulosic material with one dimension in nanoscale, which are referred to generically as nanocellulose. Among nanocellulose, three principal categories are divided according to different extraction

processes and cellulose sources: microfibrillated cellulose (MFC), nanocrystalline cellulose (NCC) and bacterial nanocellulose (BNC). Their different morphologies are exhibited in TEM or SEM micrographs, as seen in Fig 1.2.1. Synonyms for each are also listed in Table 1.2.1 along with their typical sources, isolation methods as well as average dimensions. These nanocelluloses not only inherit important properties of cellulose, such as hydrophilicity, broad chemical-modification capacity but also possess new features as nanomaterials, like very large surface area and high inter-fibril contact.

MFC is manufactured through mechanical homogenization with or without previous chemical or enzymatic treatment. Such treatments aim at delaminating cellulose fibers and liberating microfibrils (see cellulose hierarchy diagram in Fig 1.1.6).The resulting MFC is composed alternatively of crystalline regions and amorphous ones with diameters comprising between 5 and 60 nm and lengths of several micrometres. After extraction, MFC exhibits gel-like morphology in water, called MFC hydrogel.

Distinguishable to MFC, NCC consists of rod-like cellulose crystals with widths and lengths of 5-70 nm and 100-250 nm, respectively. No amorphous regions are present in NCC since it is removed from cellulose source by acid hydrolysis, often followed by ultrasonic treatment. Owing to their crystalline structure and rod-like shape, NCC crystals present interesting optical and liquid-crystalline properties[43–45] and appear as very promising coating additives, food packaging and gas barriers. However, NCCs have limited flexibility compared to MFC due to lack of amorphous regions.

Bacterial nanocellulose is formed by aerobic bacteria via biosynthesis from low-molecular-weight carbon sources like D-glucose. These bacteria, such as acetic acid bacteria of Gluconacetobacter genus, are capable of excreting exopolysaccharide at the interface to air when they are cultivated in common aqueous nutrient media[46]. The resulting BNC hydrogel is composed of a network of nanofibers whose diameter ranges between 20 and 100nm, enclosing up to 99% of water. In contract to MFC and NCC that are isolated from cellulosic sources, BNC is formed directly as a nanopolymer which contains a stable network of pure cellulose free of lignin and hemicellulose content. The special features of BNC confer it a variety of applications in medical implants[47], textiles, cosmetics, *etc.*.

Table 1.2.1 Nanocellulose family (copyright Klemm *et al.*[48])

Type of nano-cellulose	Selected references and synonyms	Typical sources	Formation and average size
microfibrillated cellulose (MFC)	microfibrillated cellulose,[1] nanofibrils and microfibrils, nanofibrillated cellulose	wood, sugar beet, potato tuber, hemp, flax	delamination of wood pulp by mechanical pressure before and/or after chemical or enzymatic treatment diameter: 5–60 nm length: several micrometers
nanocrystalline cellulose (NCC)	cellulose nanocrystals, crystallites,[2] whiskers,[3] rodlike cellulose microcrystals[4]	wood, cotton, hemp, flax, wheat straw, mulberry bark, ramie, Avicel, tunicin, cellulose from algae and bacteria	acid hydrolysis of cellulose from many sources diameter: 5–70 nm length: 100–250 nm (from plant celluloses); 100 nm to several micrometers (from celluloses of tunicates, algae, bacteria)
bacterial nano-cellulose (BNC)	bacterial cellulose,[5] microbial cellulose,[6] biocellulose[7]	low-molecular-weight sugars and alcohols	bacterial synthesis diameter: 20–100 nm; different types of nanofiber networks

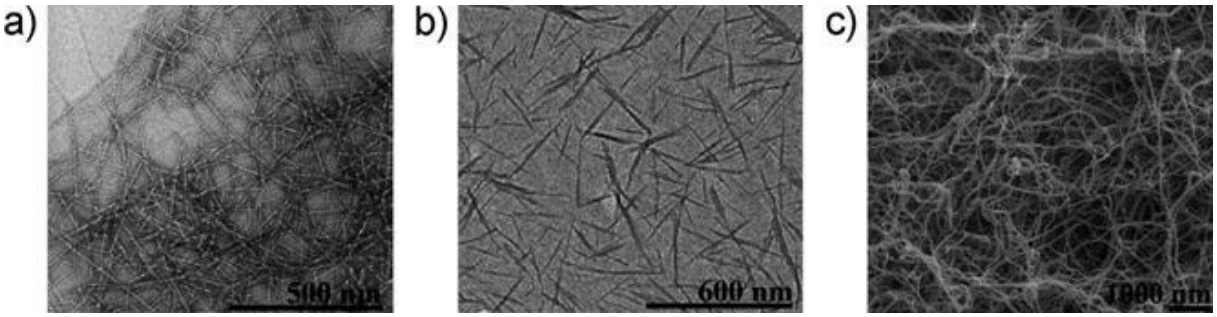

Fig 1.2.1 TEM micrographs of a) MFC[49] and b) NCC[50]; SEM micrograph of c) BNC[48]

In context of current thesis, MFC is chosen to be the main constitutional material to produce self-standing and flexible electrode. The reasons lie on its better flexibility, abundant wood sources and practical elaboration ways. In the following sections, manufacturing method and rheological properties of MFC hydrogel, together with mechanical properties of MFC films and composites, will be detailed.

1.2.1.1 MFC hydrogel elaboration

Microfibrillated cellulose is currently extracted from a number of different cellulose sources. Since wood is the most important industrial source of cellulosic fibers, it is thus the main raw material used to manufacture MFC. Compared to wood, non-wood sources, such as sugar beet pulp[39], wheat straw and soy hulls[51,52], are attracting increasing interest thanks to the their abundance in nature and the lower energy consumption during extraction processes. Cellulose microfibrils are easier to be separated from these sources since they are extracted from primary wall, in contrast to wood sources where cellulose fibers are presents in the secondary wall[12].

Irrespective of cellulosic sources, MFC production starts from a cellulosic pulp which is made from wood chips or other sources via a pulping process. As a chemical treatment, different types of pulps are made by adding different chemical products: kraft pulp is made by using a mixture of sodium hydroxide and sodium sulphide to dissolve non-cellulose ingredients like lignin and hemicellulose, in which almost pure cellulose fiber could be obtained; pulping with

salts of sulphurous acids leads to cellulose sulphite pulp which contains more by-products, like hemicellulose, in cellulose fibers.

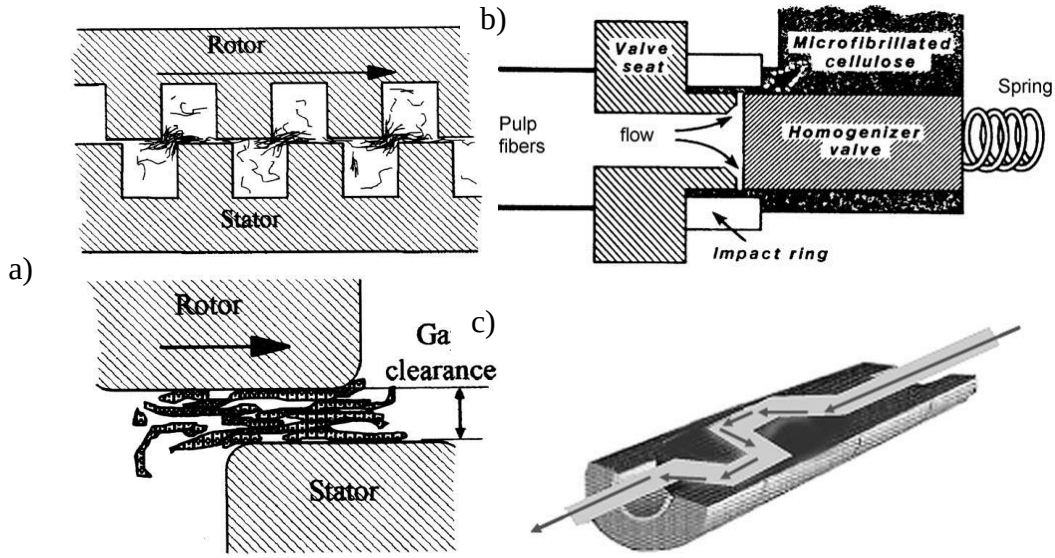

Fig 1.2.2 Mechanical treatments in: a) refiner[53]; b) high-pressure homogenizer[54]; c) high-pressure microfluidizer[12,48]

Mechanical treatments are essential to produce the gel-like MFC suspension from the original cellulose pulp. Conventional way of mechanical treatments consists of a refining process combined with homogenization[55]. The refining is accomplished in a disk refiner (Fig 1.2.2a)) where the diluted fiber suspensions is forced through a gap between the rotor and stator disks, which have surfaces fitted with bars and grooves, against which the fibers are subjected to repeated cyclic stresses[53]. In the following homogenization, previously refined cellulose fibers are pumped at high pressure and forced through a spring-loaded valve assembly (Fig 1.2.2b)). Since the valve opens and closes in rapid succession, the fibers are subjected to a huge pressure drop with high shearing and impact forces. The combination of forces promotes a high degree of delamination of cellulose fibers and leads to a release of microfibrillated cellulose. The refining process is carried out prior to homogenization due to the fact that refining could produce external fibrillation of fibers by gradually peeling off the external cell wall layers (P and S1 layers) and exposing the S2 layer, and also cause internal fibrillation that loosens the fiber wall, preparing the pulp fibers for subsequent homogenization treatment[56].

After the first homogenizer being applied by Turbak *et al.* in 1985, recent alternatives for mechanical treatments have been proposed: microfluidizer, grinder, cryocrusher, *etc.* Among them, microfluidizer has attracted increasing attention thanks to the more uniformly sized fibers that it could produce. In the microfluidizer, the cellulose pulp passes through thin z-shaped chambers (whose diameters ranges between 200 and 400 μm) under high pressure, *i.e.*, 2070 bar. The shear rate is thus quite huge (up to 10^7 s^{-1}), resulting in the formation of very thin cellulose nanofibrils.

Table 1.2.2 Comparison of energy consumption required in mechanical treatments under different pre-treatments

Pre-treatment	Pulp type	Energy required (kWh/t)
None	Kraft	12 000-70 000[57]
None	Sulphite	27 000[58]
Enzymatic	Sulphite	1500[58,59]
TEMPO	Kraft	1940[60]
Carboxymethylation	Kraft/sulphite	500[58,61]

Each of previously mentioned delamination technics requires huge energy consumption. For the purpose of producing gel-like MFC with adequate dimensions, 5-10 passes through the homogenizer are necessary. Eriksen *et al.*[57] determined that the electricity consumed by a homogenizer for fibrillation of kraft pulp reaches as high as 70000kWh/t. Sulfite pulps are easier to delaminate than kraft ones due to a high hemicellulose content and/or charge density which facilitates cellulose disintegration. Nevertheless, 27000kWh of energy is still required for the manufactory of one ton of MFC suspension with a high hemicellulose content[58]. The development of disintegration methods that are less energy-consumption becomes an important topic in MFC production. The combinations of some pre-treatments and the mechanical treatment have thus been suggested. Pre-treatments of cellulose fibers, including enzymatic hydrolysis, TEMPO-mediated oxidation and carboxymethylation, help reducing energy consumption in the following mechanical treatments on two major mechanisms: i) by increasing fibers swelling in water and ii) by chemical modification on fibers' surface. Enzymatic pre-treatment with *i.e.* endoglucanse improves the swelling of fibers and makes them less stiff and cohesive, thus decreasing the energy needed for disintegration[62]. TEMPO-mediated oxidation pre-treatment selectively converts the C6 primary hydroxylate groups of cellulose to carbonxylate groups via the C6 aldehyde groups. As a result, nanofibrils within the fibers separate from each other due to the repulsive forces among the ionized carboxylates, which overwhelm the hydrogen bonds holding them together[63]. As another chemical pre-treatment, carboxymethylation increases the anionic charges in the formation of carboxyl groups on the surface of MFC. When the charge density of pulp fibers rises, charge repulsion leads to a drastic decrease in fiber-fiber friction and therefore less susceptibility to flocculation as well as a decrease in clogging tendency[64]. Cellulose fibers are hence easier to delaminate. The above-mentioned pre-treatment methods are compared in Table 1.2.2 in terms of energy consumption reduction.

1.2.1.2 Rheological properties of MFC hydrogel

MFC forms gels at low concentration in water. Photographs of MFC water dispersions produced using two different pre-treatments were provided by Lavoine *et al.*[12], as seen in Fig 1.2.3. A large number of rheological studies have been conducted during the last decades on MFC suspensions that were extracted from different sources via different disintegration methods. The studies mostly focus on the determination of the viscosities (or shear stresses)

as a function of shear rate in the flow mode and the viscoelastic responses (the storage G' and loss moduli G") in the oscillation mode.

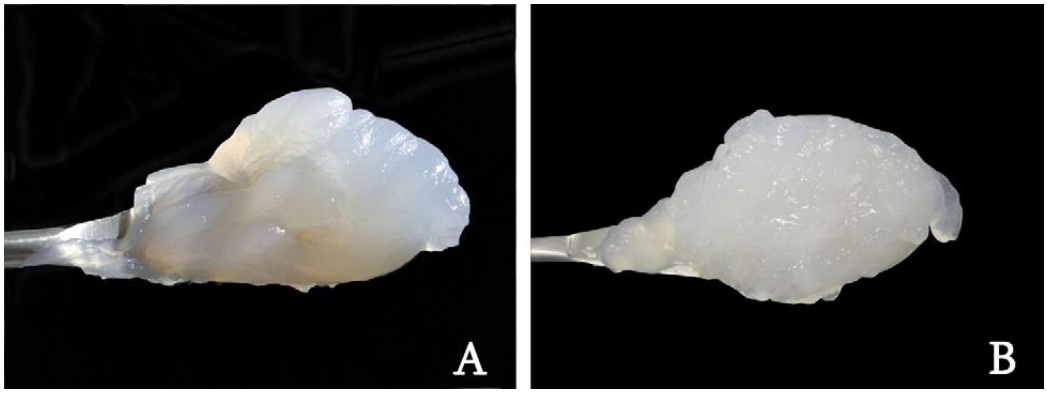

Fig 1.2.3 Pictures of two different MFC suspensions furnished by FCBA, France: A) 2% (w/w) MFC from eucalyptus, enzymatically pre-treated; B) 3% (w/w) MFC TEMPO-oxidated from dömsjo.

It was largely reported that MFC suspensions had shear-thinning and thixotropic behaviours during flow shear measurements[65–67], as symbolically shown in Fig 1.2.4. As it was much observed, the viscosity of a 2% MFC hydrogel decreases as the shear rate increases in low shear rate region (10^{-3} ~10 s^{-1}) as well as in high shear rate one (100~10^{3} s^{-1}). These two inclined lines are connected by a Newtonian plateau at intermediate shear rates between 10 and 100s^{-1}. The shear thinning behaviour in the first region is concluded by several authors[66,68] to be the breakage of the entangled 3D network of MFC (that is flocculated in water) when shearing is applied. Then the Newtonian plateau at intermediate shear rates seems to be confusing whereas Karppien *et al.*[69,70] tried to explain it by studying the floc size distribution. They suggested that in the plateau region, the floc size increases rapidly with a broadened size distribution, causing the collision between fibers more frequent within fiber-rich areas, which compensates the viscosity loss driven by the applied shearing. Nevertheless, after the plateau, floc size decreases despite an increase in shear rate, leading to the second region of shear thinning. Furthermore, still in Fig 1.2.4, a weak thixotropic tendency of MFC could be noticed due to the presence of a hysteresis loop during back and forth of shearing at intermediate shear rates. Such a hysteresis loop is created since the microstructure of flocs has been destroyed by the imposed shearing and there is not enough time for it to recover when the shear force comes back, resulting a different in viscosity at the same level of shear rate. Usually the loop has a small area, signifying that a short time is sufficient for rebuilding the flocculation[71]. Worth to noticing that there is a strong influence of concentration as well as pH on MFC rheology[66,69].

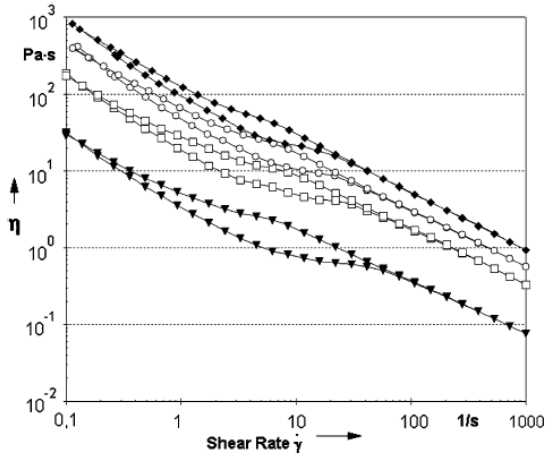

Fig 1.2.4 Schema presenting the flow properties of a bleached sulphate MFC of different concentrations: (1%) filled triangle; (2%) open square; (3%) open cycle; (4%) filled diamond.

The rheological studies are essential for MFC to be used as bio-ink in further 3D printing with or without other additives. Its shear-thinning behavior together with a short relaxation time confer it a good printability through an extrusion-type printer for the purpose of manufacturing self-standing MFC objects in three dimensions[15]. Rees *et al.*[72] piloted the 3D printing of MFC with two selected types of MFC and successfully obtained a printed objet with clear grid-pattern after freeze-drying (in order to preserve the exact morphology of the printed objet). Since then, the utilization of single or mixed MFC hydrogel as bio-ink has attracted increasing interest.

1.2.1.3 Mechanical properties of MFC films and composites

MFC hydrogel forms films after air drying or oven drying. Many methods could convert MFC gels into films: casting, vacuum filtration, dynamic jet, *etc.* Since they are analogous to papermaking process, MFC films are also called MFC nanopapers. As water is gradually removed from the wet web, cellulose microfibrils are getting closer and closer to each other until that hydrogen bonds are formed within inter-fibril contact areas. A multi-layer and porous network of MFC is established.

Compared to conventional paper, high specific tensile strength and elastic modulus have been characterized in MFC nanopaper, according to many reports[73–76]. Since mechanical characterization depends intimately on measuring conditions as well as MFC nanopapers' quality, such as fiber orientation, fiber sources, fiber dimensions and preparing methods, the mechanical strengths provided by different authors are quite varied. Sehaqui *et al.*[76] compared NFC and traditional wood fibers in terms of mechanical strength and reported a drastic improvement in elastic modulus by 66% as well as in tensile strength by 142%.

Some studies[73,75,77] focus on the influence of wood sources and delamination process on mechanical properties of MFC nanopaper. As it was revealed, a higher degree of pre-treatment and mechanical treatment clearly results an improvement of tensile strength. It is

rather reasonable since highly refined fibers could achieve much more contact among each other for hydrogen bonding.

In addition, many researches aim at correlating film-making methods and the final nanopapers' quality. Sehaqui et al[74,76] investigated the mechanical behaviors of MFC nanopapers made by varied forming process and a filtration/compressed drying combined method, called Rapide-Köthen, was recommended due to the best mechanical strength that it could provide for films made in such a way. Since the mechanical strength is quite sensible to the fiber orientation distribution, such a constrained method inhibits in maximum the out-plan oriented fibers, leading to a great in-plan mechanical strength. The importance of fibril orientation was also verified in the work of Baez *et al.*[78]. Furthermore, since drying is the most relevant process to the development of mechanical strength of paper due to the fact that hydrogen bonds are formed during this period as water is evaporating, better paper quality can be achieved by choosing appropriate drying conditions. Restrained drying induces drying stress in the paper web where shrinkage is not allowed, resulting to higher Yong's modulus, higher tensile strength (by up to 40%[79]) and better dimensional stability of the sheet than those dried freely.

Owing to its high-strength and elastic network together with the low density, MFC have been used as reinforced agent in some composites or as coating materials[80]. Virtanen *et al.*[81] investigated MFC/alginate composites whose mechanical properties were significantly improved with the increasing amount of MFC in them. Applications for such composites are multiple : bio-degradable packaging[81], medical devices[82], electrode material[83,84], *etc.*.

1.2.2 NaLS precursor

Lignosulfonates (LS) are formed during the sulfite pulping process by the cleavages of the α-O-4 linkages of the randomly cross-linked network of lignin (see Fig 1.1.7), and a sulphonation of the α-and/or γ-position of the side chains of C_9 units[14]. The fragments are quite water-soluble owing to the introduction of sulphonic acid groups. The resulting lignosulfonates are wildly used as dispersing agents, binders[85] and complexing agents. LS was chosen as another important ingredient in the context of the current thesis for multi reasons. As a derivative of wood lignin, LS contains equally high carbon content (≈60%) but excellent water-processable capacity despite its comparatively low-cost for manufactory. Composites made from MFC/LS slurry are self-standing after drying and could achieve considerable conductivity after high temperature pyrolysis thanks to the high carbon content of LS. In the following sections, the manufacturing methods, the property in water and the rheological properties of LS will be detailed.

1.2.2.1 Production and main properties of NaLS

Production of lignosulfonates starts from the spent sulphite liquors (SSL). The latter are produced as a waste product from the production of cellulose pulp via a sulfite process. The dissolved solids in SSL consist largely of lignosulfonates and the remainder of sugars and acidic degradation products of cellulose and lignin. Various method have been used to

separate LS from the other constituents, including precipitation[86], dialysis[87] and chromatography[88].

The resulting lignosulfonate macromolecule forms a randomly branched polyelectrolyte (Fig 1.2.5a)). Commercial lignosulfonates normally have broad molecular weight distributions (M_w=5000-60000 g/mol, M_w/M_n=3-12), and the degree of sulfonation (DS) varies from 0.4 to 0.7 sulfonate groups per phenylpropane unit[89,90]. Moreover, since sulfonic acids are strong acid, LS are therefore negatively charged with charge density varied depending on PH value. A fragmented molecular structure of LS is demonstrated in Fig 1.2.5b). In the literature, the relative content of phenylpropanoid monomers, linkage types and sulfonate groups is known whereas their relative location and the detailed branching pattern as well as the position of charged groups are not well known[89]. Dissolved in water, LS molecules coil to form a compact and spherical structure where the hydrophilic sulfonic acid groups are positioned at the surface of a hydrophobic hydrocarbon core[89,90].

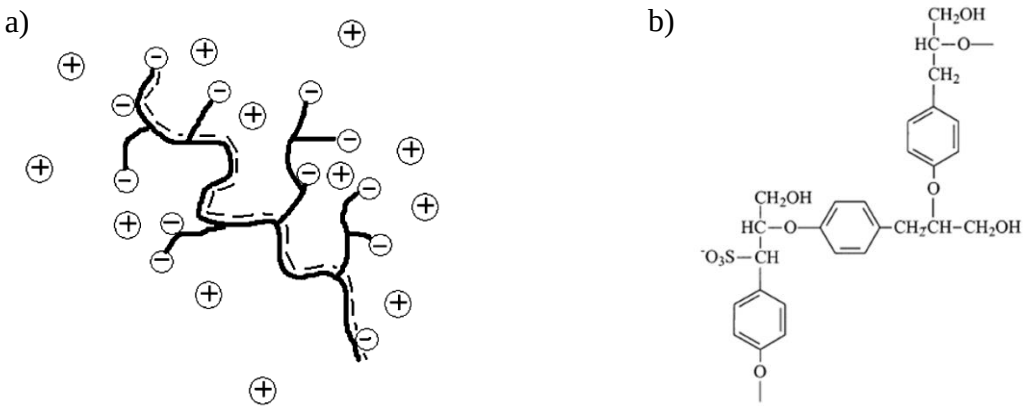

Fig 1.2.5 a) A schematic view of NaLS macromolecule[14] (cycles indicate the charge groups: negative for sulfonic acid groups which are attached to the molecular chain; positive for sodium ions); b) Chemical formula of a fragment of LS molecular (copyright Fredheim *et al.*[89])

Lignosulfonates have been applied for multiple industrial uses since they were commercially available in the early 1930s, thanks to their polyelectrolyte nature. The most common application is to work as dispersing agents to deflocculate or to stabilize the colloidal suspensions. As a polyelectrolyte, LS adsorbs at the solid–liquid interface and infer a repulsive force, thus reducing or eliminating the adhesion between particles in close proximity[91]. Furthermore, it is used as soil conditioner[92] since it is capable of adsorbing on the surface of soil, converting the unstructured soil into a macrostructural one. The hydro-physical properties of soil are thus regulated with an improvement of fertility regeneration and controlled soil erosion. LS has a cross-linked macromolecular structure, as a result, it was reported that an improvement of plastic properties of soy protein could be observed when 30% to 40% of LS was added[93].

1.2.2.2 Rheological properties of NaLS solutions

Although NaLS is frequently incorporated into polymers in a slurry state to form the composites for multifunction, its rheological behaviours under steady shear flow have seldom been investigated. To our best knowledge, only Vainio *et al.*[94] reported the Newtonian plateau of viscosity for each LS solution with concentrations ranging from 10% to 50% (Fig 1.2.6a)). The Newtonian behaviour of LS in solutions seems to confirm its "compact spherical morphology", as mentioned in the previous section.

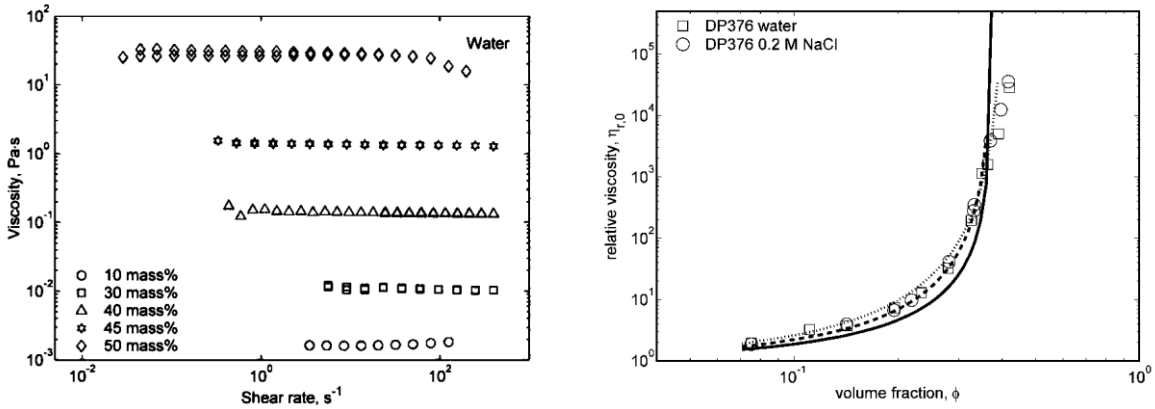

Fig 1.2.6 a) Viscosity evolution of LS solutions as a function of shear rate; b) relative viscosity as a function of volume fraction of LS solutions

It could be seen from Fig 1.2.6a) that the viscosity magnitude increases drastically with the increase concentration by over 10^4. Such a rise of viscosity is reasonable since in higher concentrations, LS "spheres" get closer to each other and the mutual friction is much more important, leading to a higher shear stress necessary as shear is applied. In order to better understand the relationship between the viscosity of LS solutions and the volume occupation by LS in water (defined as volume fraction Φ, which could be transformed from normally used mass concentration c via Eq 1.2.1), the Krieger-Dougherty (K-D) equation was applied, Eq 1.2.2, which is a phenomenological model for concentrated suspension[95].

Eq 1.2.1 $$\phi = \frac{1}{1+\rho_{LS}/\rho_{eau}*(1-c)/c}$$

Eq 1.2.2 $$\eta_r = (1-\phi/\phi_m)^{-[\eta]\phi_m}$$

Where ρ_{LS}=1.4 g/cm^3 (according to Marcus[96]), η_r is the relative viscosity of each suspension that is determined from its viscosity plateau in Fig 1.2.6a). Φ_m and $[\eta]$ are respectively the maximum volume fraction and the intrinsic viscosity of LS, whose values need to be determined by Curve Fitting.

Open squares in Fig 1.2.6b), that are derived directly from the rheological experimental results, illustrate that a viscosity divergence at volume fraction around 0.4. Curve fitting (dotted line) using K-D equation leads to a good reproduction of experimental data and provides the value of Φ_m and $[\eta]$ at 0.37±0.01 and 6.8±0.3, respectively. Generally, the maximum volume fraction for hard spheres is approximately at 0.63[97], and Φ_m increases with

polydispersity[98]. Thereby, Vainio *et al.* proposed a monodispersed non-spherical morphology for LS particles dissolved in solution due to the rather low Φ_m that they obtained.

1.3 Pyrolysis of MFC/LS system and its kinetic modelling

1.3.1 A short review of experimental thermoanalytical methods

The needs to control the carbon production during thermal decomposition of MFC/LS system as well as to achieve a stable and homogeneous conductive network require a better understanding of pyrolysis kinetics of the included biomass components. Experimental thermal analysis technologies provide efficient data for pyrolysis kinetic analysis and furthermore, for the construction of kinetic models. Such data could be obtained by monitoring a property of the sample against the evolution of temperature or time, in a specific atmosphere. The properties which interest thermal analyzers are listed in Table 1.3.1, along with the corresponding measuring techniques. In the early years, thermal analysis were conducted by isothermal methods, which means properties of samples were recorded by repeating the experiments under isothermal conditions at different temperatures. Nowadays, isothermal methods have generally been replaced by dynamic ones because of the narrow temperature range that they could exploit despite the needed toilsome work, as well as the unavoidable existence of the non-isothermal stage during the initial heating ramp. The non-isothermal analysis technologies use modern thermobalances that allow samples to undergo a programmed continuous temperature rise, which ensures no temperature regions are omitted. However, the convenient dynamic methods still have shortcomings, such as the disparities of values of kinetics parameters obtained from repeated experiments under same conditions and the increased sensibility to experimental noise. For the purpose of overcoming these defaults, low sample weight (<30mg) and low heating rate (<10K/min) are recommended in order to eliminate the heat and mass transfer limitations. Moreover, the accuracy of non-isothermal methods could be improved by collecting data from experiments performed at various heating rates, which is generally adopted by researchers in recent kinetic studies.[99–101]

Table 1.3.1 A list of thermoanalytical technologies (copyright White *et. al.*[102])

Property	Technique	Parameter measured	Abbreviation
Mass	Thermogravimetric analysis	Sample mass	TGA
	Derivative thermogravimetry	First derivative of mass	DTG
Temperature	Differential thermal analysis	Temperature difference between sample and inert reference material	DTA
	Derivative differential thermal analysis	First derivative of DTA curve	
Heat	Differential scanning calorimetry	Heat supplied to sample or reference	DSC
Pressure	Thermomanometry	Pressure	
Dimensions	Thermodilatometry	Coefficient of linear or volumetric expansion	
Mechanical properties	Thermomechanical analysis		TMA
Electrical properties	Thermoelectrical analysis	Electrical resistance	TEA
Magnetic properties	Thermomagnetic analysis		
Acoustic properties	Thermoacoustic analysis	Acoustic waves	TAA
Optical properties	Thermoptical analysis		TOA

Among the thermoanalytical technologies, thermogravimetric analysis is the most commonly used since it records the mass decrease of solid phase due to the devolatilization during the thermal decomposition at the imposed heating rate within the certain temperature range. Its first-order derivative curve, -dm/dt, known as differential thermogravimetry (DTG), is somehow more interesting for being able to provide the reaction rate evolution.

Thermoanalytical methods provide an excellent data base for the latter kinetic modelling. However, it cannot tell neither the exact reactions taking place during thermal decomposition, nor the numerous volatiles that are produced throughout the pyrolysis process, and overall, the pyrolysis mechanism. Therefore, other analytical methods (optical, X-ray, *etc.*) should be employed to provide further information concerning the chemical or structural modifications in samples. In the present work, mass spectrometry (MS) technology is coupled with TGA for the purpose that the former could characterize the produced volatile molecules by means of ionization followed by the detection of these ions. The information provided by MS could, to some extent, help determine the volatile gazes which rise from the pyrolysis of the sample, and thus is dispensable for a better understanding of the pseudo-components in the kinetic model.

1.3.2 Pyrolysis kinetics

1.3.2.1 Biomass pyrolysis kinetic modelling

Kinetic modelling of biomass is mainly based on its DTA data. For a better understanding of conversion process, the term "conversion degree" is established, as is defined in Eq 1.3.1. α is a function of the initial mass (m_0), the current mass (m) and the final mass (m_f) of samples, all of which could be read from TGA data. The raison for applying α for kinetic modelling, instead of mass loss (m/m_0), consists mainly in that the definition of conversion α excludes the part of non-reactants (ash content+ the char) during pyrolysis, by a subtraction term (m_0-m_f) in the denominator in Eq 1.3.1. Moreover, the T-depended evolution of α begins at 0 and ends at 1, with the former standing for the eve of reactions and the latter representing the final state of reactants where they accomplish the devolatilization. Thus, α signifies more intuitively the whole conversion routine, compared to mass loss evolution. The first-order derivative of α, dα/dt, is called the conversion rate.

Biomass undergoes a set of quite complex reactions throughout pyrolytic decomposition. Therefore, a hypothesis arises that pyrolysis of biomass could be considered as the sum of several independent parallel reactions. Each reaction takes place owing to the decomposition of a specific component of the biomass sample, called pseudo-component, since its real chemical nature usually remains unknown. Based on such a parallel schema, the conversion or conversion rate function of biomass is the superposition of that of each pseudo-component multiplied by its mass fraction (μ_i), as is expressed by Eq 1.3.2 and Eq 1.3.3.

Eq 1.3.1 $$\alpha \equiv \frac{m_0 - m}{m_0 - m_f}$$

Eq 1.3.2 $$\alpha = \sum_{i=1}^{N} \mu_i \alpha_i$$

Eq 1.3.3 $$\frac{d\alpha}{dt} = \sum_{i=1}^{N} \mu_i \frac{d\alpha_i}{dt}$$

Under isothermal conditions or even dynamic ones but without heat or mass transfer limitations, the conversion rate of each pseudo-component can be influenced by two terms (Eq 1.3.4).

The first one (Eq 1.3.5), known as rate constant, presents an Arrhenius dependence on temperature, in which A_i, in s^{-1}, is the pre-exponential factor or the frequency factor and E_i, in KJ/mol, is the activation energy of the corresponding reaction. For homogeneous gaseous systems, the Arrhenius expression is proved appropriate for kinetic analysis since their energy distribution function could be represented by Maxwell-Boltzmann equation which is the starting point of Arrhenius equation. Therefore, the physical significance of Arrhenius parameters can be interpreted by molecular collision theory[102]. The activation energy E is regarded as an energy barrier that must be overcome so that molecules can get enough close to react and form products. The frequency factor, A, provides a measure of the frequency of occurrence of the reaction[103]. Thus, the rate constant, k(t), being the product of A and the exponential term including E, yields the frequency of successful collisions[104]. However, pyrolysis of solid state materials, like biomass, is considered to be a heterogeneous chemical reaction. There has been some criticism for the use of Arrhenius equation in solids kinetics in a physical point of view and among them, Garn[105] emphasized that this equation could only be applicable to homogeneous reactions. In spite of that, Arrhenius-like expression has been successfully used for biomass kinetics modelling[99,101,106–108] and it has allowed for descriptions of temperature dependence of many thermally activated solid state processes such as nucleation and nuclei growth[109] or diffusion[110] since for these cases, the system must overcome a potential energy barrier and the energy distribution along the relevant coordinate is governed by Boltzmann statics. Besides, Galwey *et. al.*[103] confirms the capacity of Arrhenius equation for being applied to solid state kinetics by proving that the energy distribution functions for both electronic and phonon energy of heterogeneous solid samples exhibit approximately the same form as that in Maxwell-Boltzmann distribution.

The second term in the left of Eq 1.3.4 is a conversion function that represents the selected reaction model. Table 1.3.2 lists the most common reaction models from literature. Among them, first order reaction model (Eq 1.3.6) is widely adopted for biomass kinetics modeling owing to its adequate adaptation to dynamic thermoexperimental results, which accounts for being applied in the present work.

Eq 1.3.4 $$\frac{d\alpha_i}{dt} = k(T)f(\alpha)$$

Eq 1.3.5 $$k(T) = A_i \exp(-\frac{E_i}{RT(t)})$$

Eq 1.3.6 $$f(\alpha) = (1 - \alpha_i\ )^{n_i}$$

Table 1.3.2 Expressions for the most commonly used reaction mechanisms in solid kinetics (copyright White et. al.[102])

Reaction model	$f(\alpha) = (1/k)(d\alpha/dt)$
Reaction order	
Zero order	$(1-\alpha)^n$
First order	$(1-\alpha)^n$
nth order	$(1-\alpha)^n$
Nucleation	
Power law	$n(\alpha)^{(1-1/n)}$; $n = 2/3, 1, 2, 3, 4$
Exponential law	$\ln\alpha$
Avrami–Erofeev (AE)	$n(1-\alpha)[-\ln(1-\alpha)]^{(1-1/n)}$; $n = 1, 2, 3, 4$
Prout–Tompkins (PT)	$\alpha(1-\alpha)$
Diffusional	
1-D	$1/2\alpha$
2-D	$[-\ln(1-\alpha)]^{-1}$
3-D (Jander)	$3/2(1-\alpha)^{2/3}[1-(1-\alpha)^{1/3}]^{-1}$
3-D (Ginstling–Brounshtein)	$3/2[(1-\alpha)^{-1/3}-1]^{-1}$
Contracting geometry	
Contracting area	$(1-\alpha)^{(1-1/n)}$; $n = 2$
Contracting volume	$(1-\alpha)^{(1-1/n)}$; $n = 3$

In this way, a set of differential equations could be produced, with each of them takes form of Eq 1.3.4 to represent a single conversion process from the parallel schema. In order to obtain a numerical solution for α_i from each differential equation, two requirements must be met: firstly, the kinetic triplet, A_i, E_i and f(α), should be given as known constants or at least, their initial values as well as ranges of values should be defined if it is programmed in an optimization function for purpose to provide best kinetic parameters with which the conversion model best fits the experimental one; secondly, a powerful mathematic calculation tool, such as Matlab, is demanded in order to provide suitable solutions with sufficient precision for thousands of data points. More concretely, the best fitting of the constructing model to the experimental curve, according to least squares principal, could be achieved with reasonable initial values and value ranges of kinetic triplets and by mathematical calculation of the differential equation set. At the same time, the optimal kinetic parameters would be given.

1.3.2.2 Model-free isoconversional method for the estimation of kinetic parameters

Although model-based kinetic method has won a special popularity for being used to evaluate solid state kinetics, especially for those under non-isothermal thermoanalysis conditions, the kinetic parameters, supplied by studies (conducted under similar heating conditions) of biomass having similar components, are sometimes inconsistent. This is mainly due to an inappropriate choice of model function f(α). Since Arrhenius parameters are highly correlated with the reaction model, they can be forcibly adjusted to accommodate any selected one from Table 1.3.2 and thus result a suitable fitting to the experimental curve. For example, early explorations[111–113] for describing the single-step thermal decomposition of $ZnCO_3$ led to a divergence that Hüttig *et al.* applied a power law model with n=2/3 to derive a smaller E (38.4 kcal/mol) as compared to the result found by Bruzs that contains an activation energy value at 95 kcal/mol based on a first-order reaction model. Such a "kinetic compensation effect"[114] evokes significant confusions for researchers when choosing a pertinent reaction model and because of it, the model-independent isoconversional method attracts a lot of attention since its empirical formula was first proposed by Kujirali *et al.*[115].

The model-free approach allows predicting Arrhenius parameters without previous assumption of reaction mechanism. It is based on isoconversional hypothesis, that is, the reaction rate at a given extent of conversion depends only on temperature. As mentioned before, the first empirical isoconversional equation was proposed by Kujirali *et al.* to evaluate the temperature dependence of materials decomposed under isothermal conditions. Laterly, in non-isothermal kinetics, both differential and integral isoconversional methods have been developed since the 1960s. Constant heating rates β_j are used for most of non-isothermal experiments, as expressed in Eq 1.3.7 (in which the subscript j represents the ordinal number of the experiment realized at the heating rate β_j).

Eq 1.3.7 $$\beta_j = \frac{dT}{dt}$$

Friedman suggested a differential isoconversional method (Eq 1.3.8) by combining the heating rate β_j with Eq 1.3.4 in a logarithmic form, in which k(T) is replaced by Eq 1.3.5. At a specific extent of conversion α, the plot of $\ln[\beta_j \frac{d\alpha}{dt}]$ versus $1/T_j$ yields a series of parallel straight lines, corresponding to different heating rates, whose slope is E/R.

Eq 1.3.8 $$\ln\left[\beta_j \left(\frac{d\alpha}{dT}\right)_{\alpha,j}\right] = \ln[Af(\alpha)] - E/RT_{\alpha,j}$$

Whereas for integral isoconversional methods, as the word "integral" indicates, they make integration of both sides of an equation that is directly transformed from Eq 1.3.4 (with k(T) being replaced by Eq 1.3.5 and according to Eq 1.3.7, $dt = \frac{dT}{\beta_j}$):

Eq 1.3.9 $$g(\alpha) = \int_0^{\alpha} \frac{d\alpha}{f(\alpha)} = \frac{A}{\beta_j}\int_0^{T_\alpha} \exp(-\frac{E}{RT})\, dT$$

where T_α is the temperature at conversion α. The integral part of the rightmost side in Eq 1.3.9 is called the temperature integral. It does not have an exact analytical solution in closed form but can be approximated by using different empirical formulas, which accounts for the variety of integral methods. In order to simplify Eq 1.3.9 for the approximation, the term x=E/RT is defined, so that Eq 1.3.9 is transformed as follows:

Eq 1.3.10 $$g(\alpha) = \frac{AE}{R\beta_j}\int_x^{\infty} \frac{\exp(-x)}{x^2}\, dx = \frac{AE}{R\beta_j} p(x)$$

One commonly used integral isoconversional approach, the Ozawa-Flynn-Wall (OFW) method[116–118], applies an approximation formula suggested by Doyle[119], seen as the Eq 1.3.11. The final equation yields Eq 1.3.12 where g(α) is a constant at each extent of conversion. This equation is valid for 20<x<60. According to it, at a specific conversion degree, the dependence of $\ln \beta_j$ on $1/T_j$ for each heating rate should be linear with the slope for such a straight line $\ln \beta_j$ vs. $1/T_j$ should be equal to -1.0516E/R.

Eq 1.3.11 $$p(x) \cong -0.0048e^{-1.0516x},\ \ for\ 20 \leq x \leq 60$$

Eq 1.3.12 $$\ln \beta_j = \ln \frac{AE}{Rg(\alpha)} - 5.33 - 1.0516x = constant - 1.0516 \frac{E}{RT_{\alpha,j}}$$

Another widely cited integral approach is called Kissinger-Akahira-Sunose (KAS) method. It employs a generalized empirical approximation formula (simplified as shown in Eq 1.3.13) that yields an appropriate approximation especially for smaller E/RT[111,120,121]. Substitution of Eq 1.3.13 into Eq 1.3.10 and taking ln of both sides result the final equation of KAS method, Eq 1.3.14. Similarly, $\ln(\frac{\beta_j}{T_j^2})$ has a linear relationship with $1/T_j$ for the heating rate β_j so that the activation energy could be read from the slope of the line $\ln(\frac{\beta_j}{T_j^2})$ vs. $1/T_j$.

Eq 1.3.13 $$p(x) = x^{-2}e^{-x} \quad for\ 20 \leq x \leq 50$$

Eq 1.3.14 $$\ln(\frac{\beta_j}{T_{\alpha,j}^2}) = \ln(\frac{AR}{Eg(\alpha)}) - \frac{E}{RT_{\alpha,j}}$$

1.3.3 Pyrolysis of three main components of biomass

As explained in chapter 1.3.2.1, kinetics of biomass could be considered as a linear superposition of each reactant's single reaction along with its percentage occupation. Thus, the study of the complicated pyrolysis process of biomass could be simplified to that of each participating constituent. In spite of the variety of biomass species, there are only three fundamental components: cellulose, hemicellulose and lignin, whose mass fractions might be changing within them among different biomass types. Hence, knowledge of the kinetics of these three components is not only necessary but dispensable for constructing any biomass system's kinetics.

1.3.3.1 A review of thermal decomposition of cellulose, hemicellulose and lignin

Abundant resources[122–125] have proved that thermal stability of cellulose (C), hemicellulose (HC) and lignin (L) are quite different. Under inert atmosphere and low heating rates (<10°C/min), HC decomposes earliest within a temperature range of 250-310°C whereas its maximum reaction rate present at around 295°C. Then cellulose decomposes between 300 and 380°C, whose DTG peak appears at 345°C. Lignin is the most thermal- stable wood constituent that decomposes much more slowly in a rather wide temperature range and only exhibits a slight "peak" at around 375 °C (Fig 1.3.1). Herein, it is worth noticing that the mass loss below 200 °C for all biomass constituents is attributed to the evaporation of moisture content in the samples. In terms of carbonaceous residue at 800°C, lignin yields nearly 44% of its initial mass, which is almost 2 times higher than that of cellulose (18%) and of HC (22%).

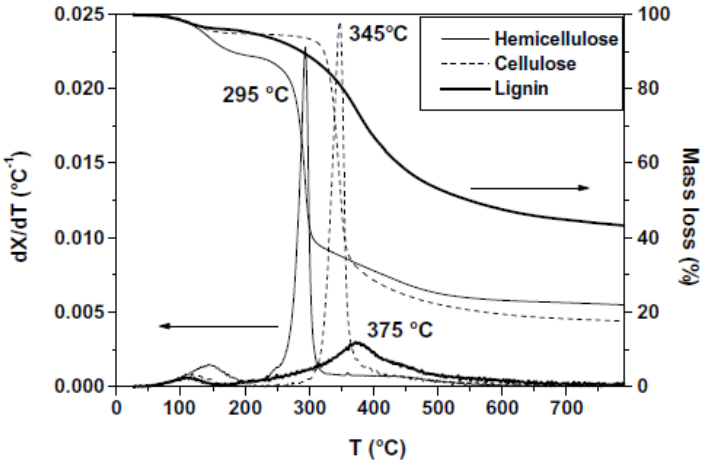

Fig 1.3.1 Comparison of thermal decomposition of C, HC and L under nitrogen (copyright: Cagnon *et al.*[122])

The above divergences of thermal behavior between cellulose, hemicellulose and lignin are strongly related to their different chemical constitutions and structures. With references to molecular structure descriptions of each of the three from chapter 1.1.3 as well as their element compositions listed below (Table 1.3.3), it is reasonable that lignin has the highest carbon yield together with the best thermal stability since it consists of highest carbon content in addition to a complex network of cross-linked aromatic molecules that are difficult to decompose during heat treatment[126]. Cellulose decomposes at a well-defined intermediate temperature range, mainly due to its homogeneous unbranched crystalline structure of linked D-glucose units. On the other hand, Xylan (a type of HC), being also a polysaccharide, is less thermally stable, which is attributed to its amorphous structure with many branched units that has a low activation energy[123].

Table 1.3.3 Elementary composition of cellulose, xylan (representing hemicellulose) and kraft lignin (copyright: Stefanidis *et al.*)

Sample	C (wt.%)	H (wt.%)	O (wt.%)[a]	Ash (wt.%)
Cellulose	42.27	6.40	51.33	0.00
Xylan	42.07	5.82	45.75	6.36
Lignin	63.41	5.89	28.42	2.28

A large amount of studies have been conducted for kinetic modelling of the three biomass main constituents[99,100,106,127,128]. However, the kinetic triplets provided by different authors for the same material are not always consistent, depending on experimental conditions, plant species, the choice of method (model fitting or isoconversional) and if model fitting method was selected, which model function is used.

Anca-couce *et al.*[107] estimated kinetic triplets of cellulose, hemicellulose and lignin by using model fitting method throughout two wood types (Table 1.3.4). With the choice of nth order reaction mechanism, they successfully simulated experimental behaviors of all the three wood components during pyrolysis in inert atmosphere (Fig 1.3.2).

Table 1.3.4 The kinetic triplets of cellulose, hemicellulose and lignin estimated by model fitting using nth order reaction on two wood species (copyright: Anca-Couce *et al.*)

Sample and model	Component	E (kJ/mol)	log$A$ (logs^{-1})	n (–)	c (–)	Fit (%)
Beech-A	HC	150.8 ± 3.6	11.74 ± 0.35	2.55 ± 0.25	0.41 ± 0.02	1.9
nth order	C	177.4 ± 1.3	12.49 ± 0.12	0.70 ± 0.02	0.49 ± 0.02	
	L	203.0 ± 30.9	14.29 ± 2.62	3.46 ± 0.65	0.10 ± 0.02	
Beech-A	HC	122.5 ± 2.6	8.96 ± 0.25	1	0.30 ± 0.01	3.5
$n = 1$	C	178.6 ± 1.8	12.67 ± 0.15	1	0.64 ± 0.01	
	L	134.9 ± 26.5	7.54 ± 2.09	1	0.06 ± 0.01	
Beech-V	HC	179.3 ± 6.5	14.36 ± 0.63	3.70 ± 0.36	0.45 ± 0.02	3.7
nth order	C	190.2 ± 0.3	13.39 ± 0.00	0.71 ± 0.05	0.40 ± 0.07	
	L	211.4 ± 14.3	15.09 ± 1.14	1.27 ± 0.31	0.15 ± 0.07	
Beech-V	HC	153.4 ± 4.1	11.82 ± 0.39	1	0.26 ± 0.01	5.1
$n = 1$	C	190.2 ± 2.0	13.45 ± 0.17	1	0.66 ± 0.01	
	L	70.8 ± 40.3	1.74 ± 3.22	1	0.08 ± 0.01	
Pine-A	HC	116	8.07	1	0.25	3.2
nth order[a]	C	146	9.71	0.59	0.58	
	L	167	11.3	2.78	0.17	
Pine-A	HC	149.8 ± 0.1	11.21 ± 0.03	1	0.18 ± 0.01	4.6
$n = 1$ (a)	C	174.9 ± 4.6	12.26 ± 0.39	1	0.64 ± 0.02	
	L	34.3 ± 7.8	−0.026 ± 0.74	1	0.18 ± 0.02	
Pine-A	HC	124.1 ± 6.1	8.88 ± 0.58	1	0.24 ± 0.01	4.7
$n = 1$ (b)	C	166.4 ± 3.6	11.53 ± 0.30	1	0.71 ± 0.02	
	L	186.6 ± 59.3	11.51 ± 4.57	1	0.05 ± 0.02	

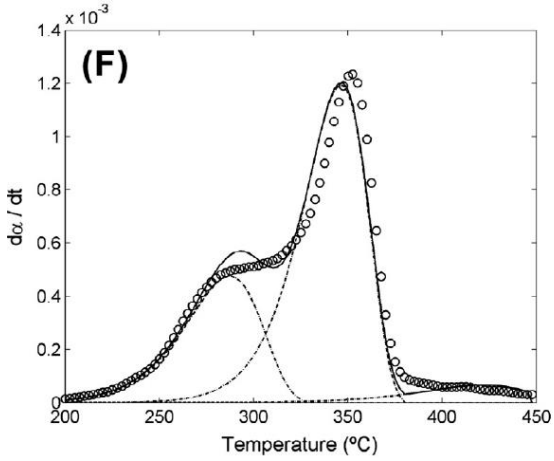

Fig 1.3.2 Fitting results when use first order reaction and kinetic data for beech-A from Pyrolysis of NaLS

The thermal comportment of lignosulfonates has seldom been reported with respect to that of lignin, mainly due to its poor application in biofuel domain together with the complex reactions that they undergo during pyrolysis. One of the minority, Jakab et al[129,130]. investigated various lignosulfonates (including CaLS and NaLS) with comparison to different lignin products by coupling TG and MS techniques. Their results reveal a total different decomposition pathway of lignosulfonates, especially for NaLS, who presents various reaction peaks in its DTG curve, in contrast to that of lignin whose maximum reaction rate peak is only one (as shown in Fig 1.3.1). Furthermore, NaLS was also compared to lignosulfonate acid (LS) and ammonium lignosulfonate (NH_4LS) in terms of thermal behaviors, showing some analogies along with differences (Fig 1.3.3). Below 600°C, all three LSs exhibit two major mass loss peaks with the distance between them varies among NaLS, LS and NH_4LS. As ionic compounds, cation type appears to have strong effect on the thermal stability of these lignosulfonates. The mass spectra of SO_2 provides an extra evidence for proving that the first reaction peak for all three lignosulfonates is largely reasonable to be considered as decomposition of sulfonate group owing to similar form and consistent

temperature range for corresponding peaks. The second peak is difficult to be identified since it is probably a mixture of dehydration and decarburization reactions. It is worth noticing that dehydration reaction happens throughout the whole pyrolysis of lignosulfonates and water remains the most important volatile product since its profiles follow roughly the feature of DTG curves. The DTG maximum of NaLS appearing at 740°C is attributed to carbonate decomposition.

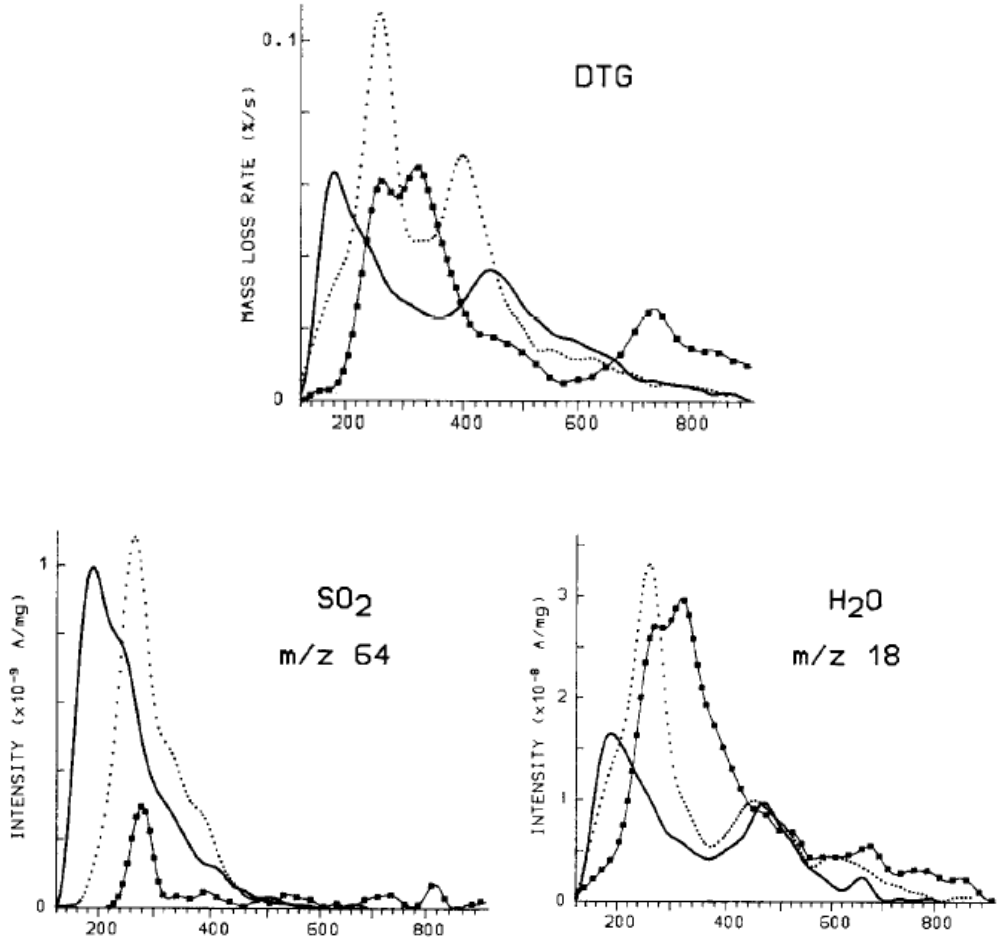

Fig 1.3.3 Comparison of thermal behavior of NaLS −▪−▪−, NH_4LS ◦◦◦ and LS ——: a) DTG curves; b) MS profiles for SO_2; c) MS profiles for H_2O (copyright Jakab *et al.*1993)

Kinetic analysis of NaLS is even more rarely conducted than its thermogravimetric studies. Till now, only Li *et al.*[131] have been found to report a complete kinetic research using model-free Kissinger approach. In his work, the activation energy of each reactant is previously determined by Arrhenius plots. The most interesting is that the asymmetry of each reaction peak is taken into consideration and characterized by a shape index s that is directly associated with reaction order n. Also, the frequency factor A can be calculated for $n \neq 1$ according to an equation derived from Eq 1.3.4 (see Li *et al.* for more details). The Arrhenius parameters for NaLS that they provided are listed in Table 1.3.5. Indeed, their method and results has useful reference values for further kinetic researches of NaLS whereas the NaLS that they used for dynamic TG experiments and the later kinetic modeling is lack of

universality, so that their DTG curves for modeling are much simpler than those of normal industrial ones (NaLS used in the work of Jakab et al as well as those used in present thesis). Consequently, there is an impending need for studying NaLS kinetics.

Table 1.3.5 Kinetic parameters of NaLS (copyright Li et al 2014)

Sample	Reaction steps	β (°C min^{-1})	S	T_p (°C)	n	Kinetic parameters	
						E_a (kJ mol^{-1})	A (min^{-1})
SL	1st	10	0.448	154.1	0.843	104.28	1.70×10^6
		20	0.728	158.8	1.075		
		30	0.860	159.8	1.168		
		40	0.779	166.6	1.112		
	Average		0.704	159.8	1.050		
	2nd	10	1.160	248.9	1.357	128.51	2.77×10^6
		20	1.396	258.8	1.489		
		30	1.192	265.8	1.376		
		40	1.371	274.2	1.475		
	Average		1.280	261.9	1.424		
	3rd	10	0.500	421.3	0.891	168.98	7.00×10^6
		20	0.508	433.1	0.898		
		30	0.574	434.7	0.955		
		40	0.428	439.1	0.825		
	Average		0.503	432.1	0.892		

1.3.3.2 Impacting factors for biomass kinetics: environmental components and ash content

In a majority of biomass systems, there are usually mixtures of the three main constituents of biomass, with the proportion of each probably varying between 0 to 100%. Although it is assumed to have no interaction between every duplet among cellulose, hemicellulose and lignin during pyrolysis of blends, whether it is always true remains controversial since largely different conclusions have been given from literature. Luo *et al.*[132,133] and some other researchers[125,134] believe the existence of significant interactions between C, HC and L during pyrolysis with investigations in terms of gas and tar production, char –formation and product composition by using TG-FTIR, TG-MS techniques together with chemical elementary analysis. However, if only taking their thermogravimetric or DTG results into consideration, on which the kinetic theory was basically founded, there is no surprising disparity between the experimental curves and the calculated ones with the latter obtained under assumption of linear superposition of the three biomass components. Indeed, influences might exist with the addition of other wood component(s) into the original single one during pyrolysis, in a way of promoting or inhibiting the production of some gases or chars, but if equilibrium is achieved between promoted and inhibited reactions, the total reaction rate of the blends could remain equal to the sum of each, same tendency as is suggested by their own results. Furthermore, instead of concluding the existence of interactions between wood components, Yang *et al.*[124] attribute such a slight shift of reaction rate peak towards higher temperature in C/HC/L blends to the mass and heat transfer limitations that are caused by the addition of other wood component(s) with different particle size(s) and chemical nature. Therefore, in a point of view of kinetic studies, it is reasonable to suppose that no interaction between cellulose, hemicellulose and lignin occurs throughout pyrolysis, which is consistent with mainstream researches in the domain of biomass kinetics[135–137].

Another discussable factor that could modify kinetic triplets of biomass is the ash content. Different extraction methods are used to produce industrial “pure” wood components and

supplementary acid or alkali treatments are applied to enable raw materials to meet strict dimensional and structural requirements for scientific research purpose. Consequently, the raw materials used for pyrolysis possess more or less inorganic mineral content, called also ash content. As indicated in Table 1.3.3, industry-available cellulose, hemicellulose and lignin have tiny amount of ash whereas commercial NaLS, on the other hand, contains a quite high mineral percentage (as high as around 20%). Generally speaking, the main elemental constituents of biomass minerals are Si, Ca, K, Na and Mg with smaller amounts of S, P, Fe, Mn and Al, all of which occur as oxides, silicates, carbonates, sulfates, chlorides and phosphates in ash content[138]. Both Müller-Hagedorn *et al.*[128] and Nassar[139] found that alkaline salts in biomass, whether added or innate, act to lower the apparent activation energy of thermal reactions and promote the formation of char. Furthermore, Varhegyi *et al.*[140] compared treated sugarcane bagasse samples with diluted inorganic salt solutions (such as MgCl2, NaCl, FeSO4, and ZnCl2) and non-treated ones in terms of thermal comportment and gas/char production by MS, revealing that the increasing char production in treated samples (except for the case of MgCl2 in which no difference was identified between treated and non-treated samples) could be attributed to an alteration of reaction pathways by theses salts. The MS intensities of all treated samples were lower than those of untreated ones, suggesting the presence of inorganic additives suppresses the secondary cracking of high molecular weight primary products. In addition to catalytic effects imposed by cation contents in ash, anions were also observed to influence the pyrolysis temperature with an impacting order: bicarbonates<sulfates<chlorides[128].

1.3.3.3 Improvement of conductive carbon production during pyrolysis

The application of carbonaceous biomass into electro-chemical devices requires them to have good electrical conductivity in addition to appropriate mechanical strength. In order to guarantee both properties, the pyrolytic process that biomass undergo should be well controlled with the purpose of promoting the dehydration reaction and char formation whereas inhibiting carbonaceous volatiles production. Numerous solutions have been suggested to efficiently improve the quality of carbonized biomass, which could be divided into several aspects: i) high pyrolysis temperature; ii) controlled heating rate; iii) pre-treatment of sample with various impregnating agents.

Perepelkin[6] suggested a relationship between heat treatment temperatures (HTT) and electrical resistivity of different biomass precursors (Fig 1.3.4). In his chart, it is clearly illustrated that, regardless of wood precursors, an increase of HTT declines observably sample's resistivity, indicating a rise of electrical conductivity in the other hand. Pyrolysis up to 750°C allow to convert all types of biomass into conducting agents, which is also in agreement with the fact that the higher heat treatment temperature is, the purer carbon material is obtained.

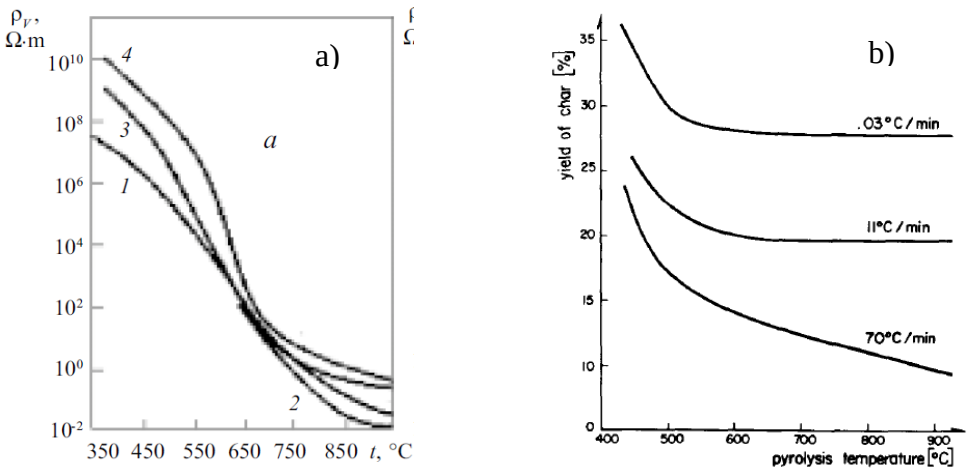

Fig 1.3.4 a) Significance of temperature on final electrical resistivity of carbon biomass: 1) and 2) hemicellulose precursor; 3)charcoal; 4)lignin carbon (copyright Perepelkin 2002); b) influence of heating rate on char yield during cellulose pyrolysis (copyright: Brunner *et al.*, 1980)

Brunner *et al.*[141] investigated in detail the importance of heating rate on char yield and char properties in cellulose pyrolysis. As it is illustrated in Fig 1.3.4b), a change of heating rate from 70 to 0.03 °C/min results a considerable increase in char yield from 11% to 28% at the end of pyrolysis at 900°C. This is due to a prolongation of dehydration reaction at low temperature (<240°C), which leads also to thermally more stable char with a low oxygen content. With examination of char properties, it is concluded that low heating rates help likewise to yield highly porous but dense chars.

Pre-treatment of biomass with additives increase its reaction rate during pyrolysis. Hence, additives play a dispensable role in biomass pyrolysis by means of enhancing reaction kinetics by cracking higher molecular weight compounds into lighter hydrocarbon products[142]. A great number of additives of various types have been suggested to improve the quality of biomass char according to different mechanisms. Flame retardants have been widely used since they could facility and stabilize the pyrolysis process of biomass[143]. Gao *et al.*[144] investigated several of them, including guanidine dihydrogen phosphate (GDP) and diguanidine hydrogen phosphate (DHP), achieving a rise of 33% on carbon yield. Zeng *et al.*[145] tried several phosphate and ammonium salts, proving the usefulness of di-ammonium phosphate (DAP) on improvement of carbon yield along with a high specific area. Besides, Lysenko et al[146] demonstrated that water-soluble organosilicon, whether alone or mixed with other ammonium additives, helped increasing carbon yield to an important extent and improving simultaneously mechanical resistivity of carbon fibers. Moreover, impregnation of biomass samples in a diluted sulfuric acid solution[147] before heating treatment or conducting the pyrolysis process of biomass in HCl atmosphere[148] helps increase the carbon yield to 38% together with a considerably restrained shrinkage observed in cellulose fibers under SEM. It is due to the fact that strong acids work as dehydration agents which keep “absorbing” H_2O molecules throughout heating. Other examples of additives are alkaline-sodium compounds,

such as NaOH, Na_2CO_3 and Na_2SiO_3, which decrease gaseous products like CH_4 and CO_2 and favor H_2 formation mostly[149]. A lot of more additives could be found in literature and the selection of pyrolysis catalysts should also consider the resulted impurity that they bring into the final carbons.

1.4 Microstructural and electrical conductivity evolution of biomass during pyrolysis

Biochars which are derived from lignocellulosic materials via a pyrolysis process have been used as environmentally-friendly carbon materials in a wide range of applications, including soil improvement[3], pollutant removal[4], greenhouse gas emission reduction[5], *etc.*, owing to their highly porous structure and the resulting high surface area[3,4]. Despite the fact that biomass has been considered as non-graphitizing carbon precursor, Perepelkin[6] summarized an electrical resistivity decrease of nearly 12 orders of magnitude for biomass precursor heat treated at 350°C and 950°C, leading to a potential use of biochars as "active" electrode materials in energy storage devices. Although outstanding cycling performances have been achieved on such biomass-derived electrodes[7–9], little interpretation has been made for the electrical conductivity development of biomass during pyrolysis.

During pyrolysis, carbon precursors suffer from molecular decomposition and condensation to form carbonaceous chars with a carbon content up to *ca.* 80%[150] (800°C). As intrinsic property, the electrical resistivity of a carbon material, with the latter seen as a packed bed of carbon particles, should account for both factors: the intra-particle resistance and the inter-particle (contact) resistance[1,151]. Both factors are strongly temperature-depended[152,153] and could thus be characterized by the microstructural evolution and the percolation model as a function of heat treatment temperature (HTT).

McDonald-Wharry *et al.*[150] summarized previous descriptions of the microstructure of non-graphitizing carbons by establishing a model called "distorted graphene triad" (Fig 1.4.1). According to it, non-graphitizing carbons are composed of 3 distinguish microstructures (Fig 1.4.2): i) regular graphite-like domains formed by average 3 graphene layers; ii) distorted graphite regions (mainly due to the existence of oxygen functional groups) which forms curved cross linking between regular graphite domains; iii) micropores with a diameter similar to the length of regular domains. Pré et *al.*[154,155] studied the nanostructure in activated carbons and carbide-derived carbons (CDCs) using high resolution transmission electron microscopy (HRTEM) which provides information about the shape, size and orientation of the defective graphene sheets.

Rhim *et al.*[10] studied the electrical property development throughout the pyrolysis of microcrystalline cellulose (MCC) and suggested that the increasing HTT leads to the continuous growth of conductive carbon clusters (regular and distorted graphite regions as mentioned above) and upon a percolation threshold at HTT between 600 and 610°C with a conductive phase volume fraction of 0.39, conductive phrases begin to make contact so that

the DC conductivity becomes detectable in MCC chars. Kercher *et al.*[156] deduced similar conclusions by studying the fiberboard carbonization in terms of electrical property.

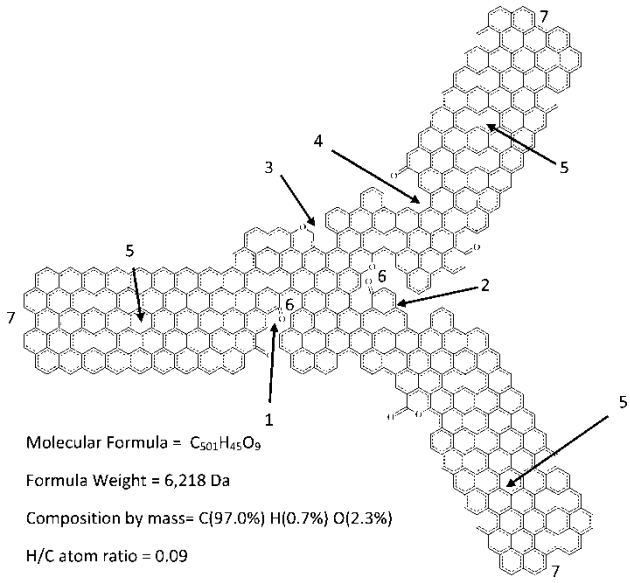

Fig 1.4.1 The structure of a "distorted graphene triad" (copyright McDonald-Wharry *et al.*[150]). Interpretation of features: (1) persistent oxygen functional groups becoming trapped by aromatic growth, (2) deep fjord regions within the graphene-like structure, (3) sites for aromatic condensation (fjord closure) by elimination of H_2 or two radicals, (4) formation of conjugated cross-links that extend the π system across the structure, (5) domains of regular graphene structure that have an approximate diameter of 1−2 nm, (6) carbonyl groups under steric strain that could induce/fix curvature and non-planarity, and (7) bays and/or K regions, which are more reactive, that could be favored sites for epitaxial growth to extend graphene-like domains or form additional cross-linking.

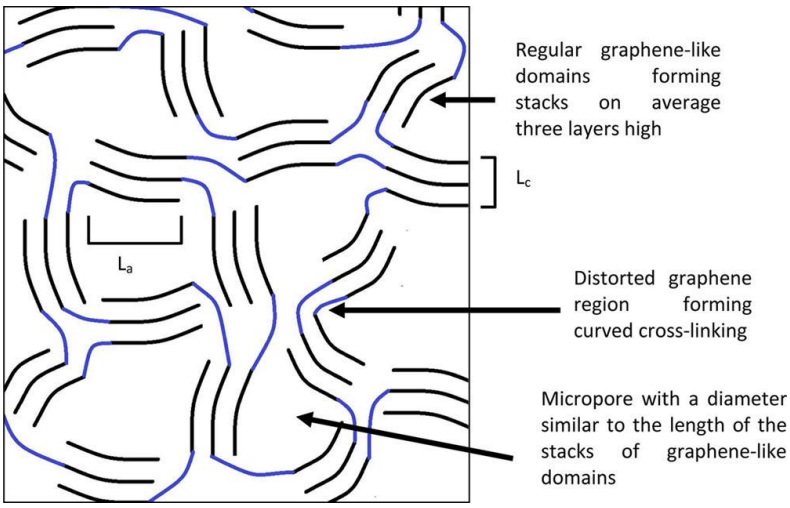

Fig 1.4.2 Illustration for the stacking of "distorted graphene triad" (copyright McDonald-Wharry *et al.*[150])

Among various lignocellulosic materials, microfibrillated cellulose (MFC) and lignosulfonate (LS) have caught special attention for the elaboration of carbon precursor composites[10,11]. The composites elaborated from MFC/LS slurries are self-standing with MFC playing a role as

mechanical reinforcement whereas LS ensures the carbon yield after pyrolysis[15,157]. In addition to the thermal stability[158], MFC/LS derived carbons could acquire adequate porosity[159] and potential electrical property with regard to their comparatively low density[160], as most of biochars do, make them a promising materials for electrodes in energy storage devices[1].

Since HTT is the predominant factor for the determination of chars' chemical and physical properties, the characterization of chars derived from MFC/LS precursor in terms of morphology, electricity measurements, density and microstructure evolution needs to be performed as a function of HTT, which, to the best of authors' knowledge, has not been investigated.

2. Materials and methods

2 Materials and methods

2.1 Materials:

MFC, in the form of a 2% (w/w) hydrogel, was provided by FCBA (Saint Martin d'Hères, France). It was produced from bleached hardwood (birch) kraft pulp via a mechano-enzymatic protocol along with subsequent homogenization at high pressure.

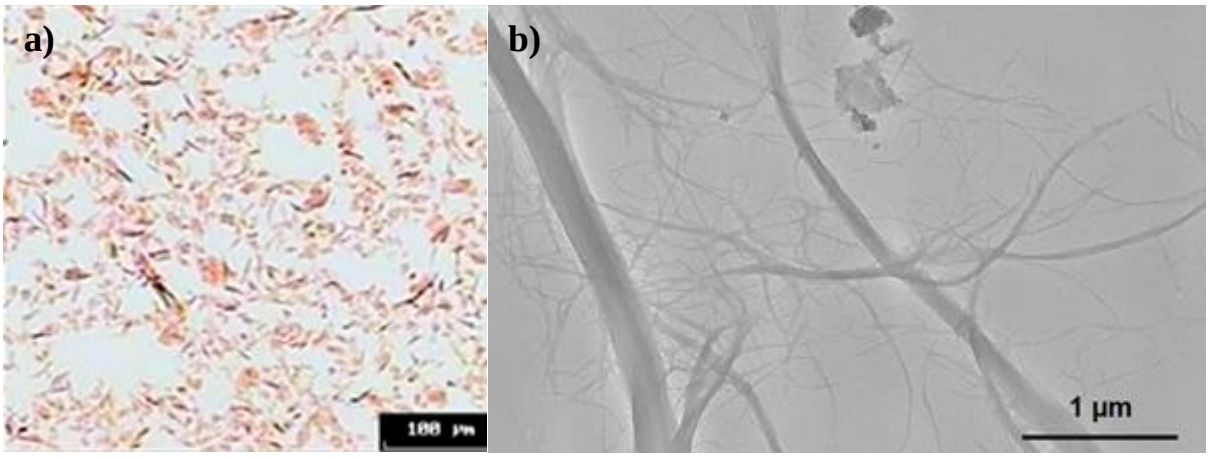

Fig 2.1.1 Morphology of the used MFC under a) optical microscopy and b) scanning electron microscopy

Sodium lignosulfonate (NaLS) was purchased from Carl Roth GmbH + Co. KG (France).It is in the form of a brown powder with sodium content reaching 9%. More detailed elemental analysis of NaLS is shown in Appendix A.

High purity cellulose powder (CP) from cotton was purchased from Sigma-Aldrich (France) with an average particle size of 50 µm.

2.2 Solution preparation

Single or mixed MFC and LS solutions of various concentrations were elaborated as follow:

Single LS solutions were prepared by simply dissolving LS of different quantities into deionized water. The following concentrations (w/w of water) were made: 20%, 30%, 40%, 50%, 52.5% and 55%, corresponding to volume fractions ranging from 0.15 to 0.47.

MFC hydrogels (0.5%, 1%, 11.4%, w/w of water) were prepared either by dilution of the pristine 2% with deionized water (for 0.5% and 1% ones) or by centrifugation (for 11.4% ones).

MFC/LS mixed slurries were elaborated by adding different quantities of LS into the corresponding MFC hydrogel. Three series of mixed slurries were prepared: i) 0.5% MFC series which contain 0.5% of MFC and 20%-50% of LS; ii) 1% MFC series with 1% of MFC and 20%-50% of LS; iii) 2% MFC series with 2% of MFC and 20%-50% of LS.

MFC (dry matter), LS powder and cellulose powder were 1: 49: 14 mixed for 3D printing purpose.

2.3 Rheological tests

Rheological tests were conducted in two modes: simple shear mode for viscosity measurements and thixotropic mode for thixotropic tests. Regardless of modes, all rheological measurements were performed by using a rotational physical MCR 301 rheometer (Anton Paar) in a plate-cone configuration. A cone with 50 mm diameter and 1° angle was used and the gap was set to 1 mm. A transparent cover was used to prevent water evaporation during measurements. Temperature of the plate was maintained at 23 °C.

Viscosity measurements were carried out for all suspensions by repeating several cycles with shear rate ranging between 10^{-3} and 10^{3} s^{-1} with about 10 min relaxing time between each cycle. Four measuring points were set for decay with 10 s between each measuring point.

Thixotropic measurements were carried out just for slurries with 2% MFC. The shear rate was maintained at 1000 s^{-1} for 20 s before a sudden drop to $0.1s^{-1}$, as was schematically described in Fig 2.3.1. Samples' viscosity and stress responses were recorded as a function of time. In order to get rid of inertial instabilities, data were recorded every 1 s after the step-down variation.

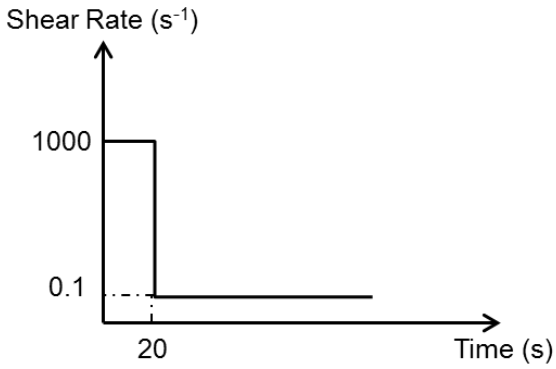

Fig 2.3.1 Descriptive scheme for thixotropic measurements

2.4 Forming methods of MFC/LS and MFC/LS/CP carbon precursors

2.4.1 Casting followed by air drying

It consists the simplest way to elaborate MFC/LS composites. Mixed slurries were poured in Teflon molds and a stainless ruler was used to spread out the slurry within the mold as well as to eliminate the extra slurry in order to smooth its surface. After drying in ambient conditions, film-like composites were obtained (Fig 2.4.1).

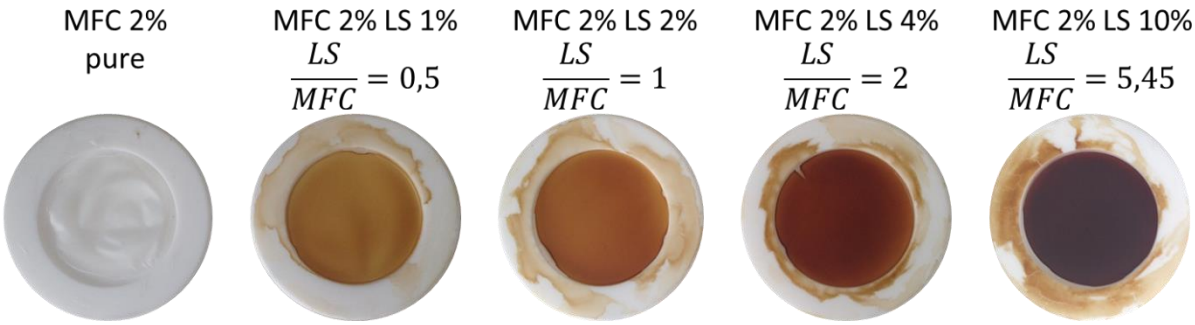

Fig 2.4.1 An example of film-making by casting

2.4.2 3D printing followed by air drying or freeze drying

A commercial 3D printer (Model 3, Seraph Robotics) was used to test the processability of 2% MFC suspensions with LS content ranging between 0 and 50%. Two series of square cuboids (LxWxH: 2x2x1 cm) were printed using a 0.96 mm syringe needle and a printing speed of 35 mm s^{-1} (corresponding to a shear rate in the needle tip of ca. 300 s^{-1}). The first series was dried at room temperature, whereas the second series, after 2h relaxation at room temperature, was slowly frozen in a refrigerator (-12°C). Frozen samples were then freeze dried in a freeze-dryer (Martin Christ Gefrierstrocknungsanlagen GmbH).

MFC/LS/CP mixtures were printed using a 3D printer (Leapfrog, Creatr HS model). The triple slurry was stored in a syringe with the plunger being pushed under a steady pressure (about 1bar) from a vacuum pump. The extruded slurry then passed through a rotating screw before being printed via a 0.5 mm needle (Fig 2.4.2a)). The printing speed, the width of filament as well as the layer height were set to be 550mm/min, 0.6mm and 0.33mm, respectively, in order to obtain a good morphological definition. Samples printed in various forms and patterns were then air-dried at ambient temperature.

Single lines of MFC/LS/CP mixture were printed using a 1mm needle (Fig 2.4.2b)) only for bending test purpose. They were then air-dried in ambient temperature.

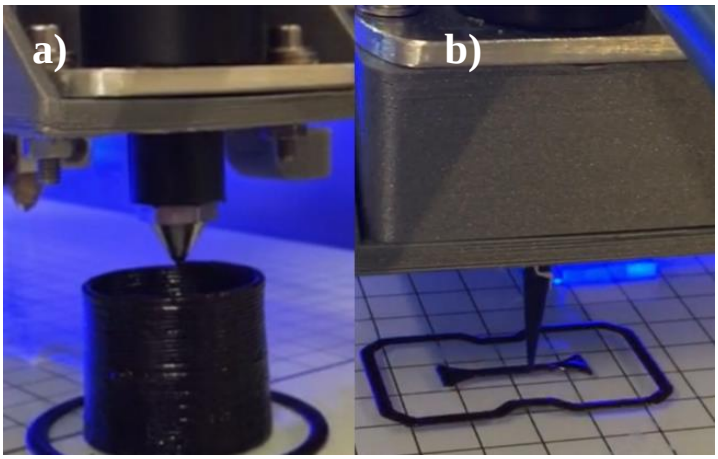

Fig 2.4.2 3D printer (Leapfrog) with an extruder of a) 1mm and b) 0.5mm diameter

2.5 Pyrolysis and its thermal characterization

2.5.1 Pyrolysis

Pyrolysis of dried composites was conducted in a tubular oven (Carbolite®, type 3216) under nitrogen flux (Fig 2.5.1). The heating schedule was listed in Table 2.5.1, with reference to Kercher at *al.*[156].

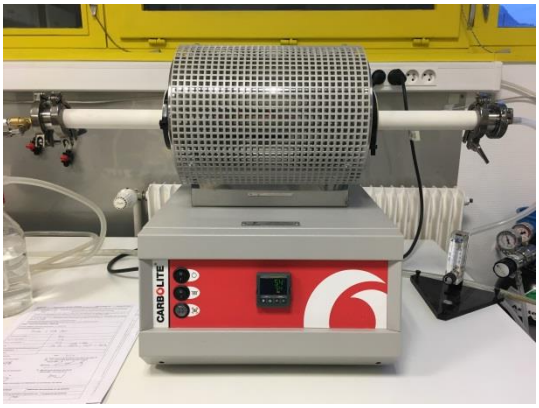

Fig 2.5.1 The used tubular oven

Table 2.5.1 Heat treatment program

T range (°C)	Heating rate (°C/min)	Dwell time at final temperature (min)
Ambient T~150	0.5	60
150~400	0.2	-
400~600	0.5	-
600~target T (600~1000)	1	10

2.5.2 Thermal characterization by TG/MS

Thermogravimetric experiments are performed in a SETARAM TG92 thermobalance under helium atmosphere. A mass spectrometer (OmniStar, PFEIFFER) is coupled to the TG analyzer through a transfer line heated at 180°C. Paper-formed samples are previously cut into tiny fragments and the mass of each sample is controlled to be less than 12 mg in order to avoid mass and heat transfer limitations during pyrolysis. TG data are recorded for all samples in a temperature range from 150°C to 800°C at heating rate of 5°C/min. Extra runs at heating rates of 2.5, 10 and 15°C/min were performed only on pure MFC and NaLS samples for the isoconversional kinetic analysis. Ionized gas molecules of m/z ratios between 1 and 200 are scanned by the MS. However, only important molecules were selected for the interpretation. The recorded intensities are normalized to those of helium and to the initial sample mass. Each TG-MS experiment is duplicated in order to ensure the reproducibility of the results.

2.5.3 Kinetic analysis

Model-based approach: the conversion degree of a matter is defined in Eq 2.5.1 as a function of the initial mass (m_0), the final mass (m_f) and the current mass (m), derived from the TG data of the sample. The total conversion (or conversion rate) of biomass is the sum of

those of its pseudo-components multiplied by their proportions (Eq 2.5.2) with N representing the number of identified pseudo-components. As shown in Eq 2.5.3, the conversion rate for each pseudo-component, $d\alpha_i/dt$, depends on: i) the kinetic constant $k(T)$ in which A_i, E_i and R are the pre-exponential factor, the activation energy and the gas constant (Eq 2.5.4), respectively; ii) the reaction model $f(\alpha)$ for which the first order reaction model is chosen as shown in Eq 2.5.5, with n_i=1 (i=1~N). Conversion rate equations for all pseudo-components, which are first order differential equations, are numerically solved using the ode23s Matlab ODE solver. Arrhenius parameters, A_i and E_i, as well as the proportions of the different pseudo-components μ_i, are determined by least square minimization of the objective function defined in Eq 2.5.6, with L being the number of experimental points. The relative deviation expressed in Eq 2.5.7 is considered to assess the quality of the fit.

Eq 2.5.1 $$\alpha = (m_0 - m)/(m_0 - m_f)$$

Eq 2.5.2 a) &b) $$\alpha = \sum_{i=1}^{N} \mu_i \alpha_i \quad , \quad d\alpha/dt = \sum_{i=1}^{N} \mu_i * (d\alpha_i/dt)$$

Eq 2.5.3 $$d\alpha_i/dt = k(T) f(\alpha_i)$$

Eq 2.5.4 $$k(T) = A_i \exp(-E_i/RT(t))$$

Eq 2.5.5 $$f(\alpha_i) = (1 - \alpha_i)^{n_i}$$

Eq 2.5.6 $$OF = \sqrt{\sum_{l=1}^{L} (\alpha^{model} - \alpha^{exp})^2}$$

Eq 2.5.7 $$Relative\ deviation = 100 \left| m_{exp} - m_{model} \right| / m_{exp}$$

Isoconversional approach: constant heating rates β_j are expressed in Eq 2.5.8 (in which the subscript j represents the ordinal number of the experiment realized at heating rate β_j). Isoconversional method makes integration of both sides of an equation that is directly transformed from Eq 2.5.3 (with $k(T)$ being replaced by Eq 2.5.4 and according to Eq 2.5.8, $dt=dT/\beta_j$) where T_α is the temperature at the conversion level α. The integral part of the rightmost side in Eq 2.5.9 is the so-called "temperature integral". Kissinger-Akahira-Sunose (KAS) method employs a generalized empirical approximation formula for the temperature integral[111,120,121] with the final equation expressed in Eq 2.5.10.

Eq 2.5.8 $$\beta_j = dT/dt$$

Eq 2.5.9 $$g(\alpha) = \int_0^{\alpha} d\alpha/f(\alpha) = A/\beta_j \int_0^{T_\alpha} \exp(-E/RT)\, dT$$

Eq 2.5.10 $$\ln(\beta_j/T_{\alpha,j}^2) = \ln(AR/Eg(\alpha)) - E/RT_{\alpha,j}$$

Where $T_{\alpha,j}$ represents the temperature corresponding to the degree of conversion α for a given sample pyrolyzed at a specific heating rate 'j'. The plot of $ln(\beta_j/T_{\alpha,j}^2)$ versus $1/T_j$ for each conversion level α yields a straight line with the slope and the interception with vertical axis corresponding respectively to $(-E/R)$ and $ln(AR/Eg(\alpha))$. The kinetic parameters (activation energy E and the pre-exponential factor A) could be deduced directly from the Arrhenius plots.

2.6 Characterization of carbonaceous chars

2.6.1 Microscopies

Morphological characterization was performed on samples, in both surface and sections, using a scanning electron microscope (FEI-Quanta 2000, ESEM^{TM}).

2.6.2 Fourier transform infrared spectroscopy

Chemical structure characterization is conducted with a Perkin Elmer FT-IR spectrometer (Perkin Elmer, USA). Each sample was grounded and then mixed with KBr powder (IR spectrometer grade) with a ratio of 1:125 in order to make testing pellets. The spectra were recorded in the wave number range of 4000 to 600 cm^{-1} with a resolution of 2 or 4 cm^{-1} and an accumulation of 32 scans per analysis. Absorption spectra were obtained and corrected with the environmental spectrum.

2.6.3 X-ray tomography

X-ray tomography (Nanotom 180, Phoenix X-Ray) was used to observe the internal structure of printed composites before and after pyrolysis. Images of every transversal section along the length of samples were recorded in order to restore the 3D structure of samples.

2.6.4 Electrical conductivity measurement

Electrical conductivity of carbonized samples was measured either by a two point ohmmeter (Fluke) or by the four-point probes system (Standa 019759), depending on the shape of samples.

Thin samples (thickness <1mm) were measured using a four-point probe system (Standa 019759) by following ASTM C611-98 (2005) and ASTM F84-98. The measuring current was generated by an impendence analyzer (Jandel, model RM3). The thicknesses of a sample were measured by a micro-comparator within the zone where the conductivity was measured in order to calculate the average thickness. The correction factor used to compensate the finite dimensions of each sample was from the work of Smits *et al.*[161]. 5 samples were measured per HTT (heat treatment temperature).

Thick objects were measured by an ohmmeter along the z axis after deposition of zinc electrodes with a diameter of *ca.*7 mm on its surfaces. The electric conductivity was then calculated with the Ohm law using the sample average thickness, the apparent contact area of the zinc electrodes and the cross sectional area of the whole square face in order to get an estimation of maximum and minimum conductivity values.

2.6.5 Density measurements

Skeletal density (true density) was measured using a gas displacement pycnometry system (AccuPyc 1330, Micromeritics, USA). Helium was used as displacement gas thanks to its extreme inertness (avoid being adsorbed) and the small molecule size (about 0.2 nm)[162], thus it can penetrate even the tiny pores in the sample.

2.6.6 Raman spectrometry

Raman spectra of carbonized chars were recorded using a Renishaw in-via Raman micro-spectrometer. A 100mW, 785nm laser was passed through a 1% transmission filter before projecting a measurement spot on samples with a diameter of approximately 1.5 µm. A 50x objective was used and frequencies between 800 and 2000 cm^{-1} were scanned in a synchroscan mode for each spectrum. 10 spectra were collected for each char sample representing 10 different measured positions.

The average of 10 spectra was calculated to represent the Raman pattern of one sample. The spectrum of each sample was then smoothed and normalized to its own G-band position (around 1600cm^{-1}). As presented in Fig 2.6.1, 5 Gaussian peaks (at around 1200, 1330, 1500, 1585, 1750 cm^{-1}, respectively) were assigned based on data from previously published articles[163–168] by considering the shape of the spectra and for the sake of highlighting the characteristic bands.

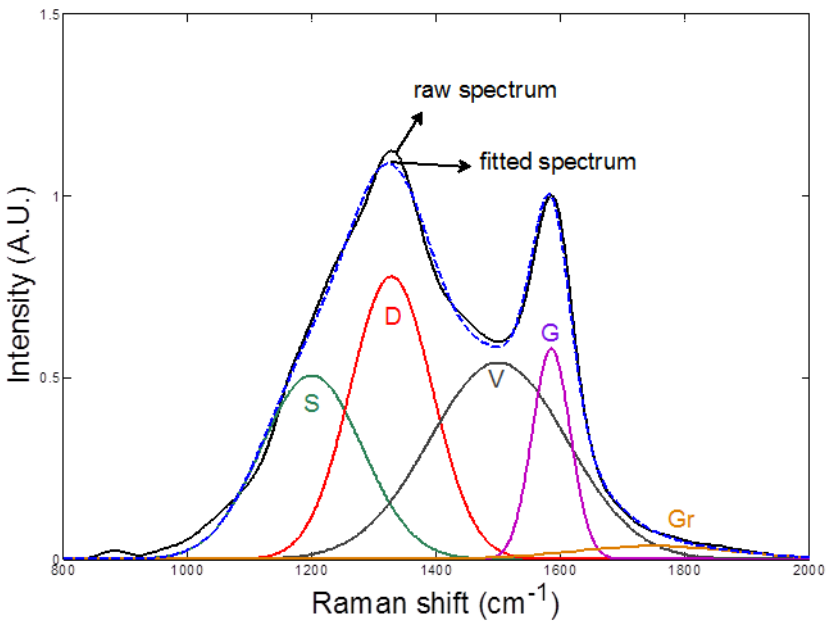

Fig 2.6.1 Raman band assignment used in this work

2.6.7 X-ray diffraction

X-ray diffraction (XRD) was used for phase and crystal structure identification. Each char, in the form of plate thin film, was placed on the sample holder and levelled to obtain total and uniform X-ray exposure. The samples were analyzed using an X-ray diffractometer (X'pert Pro MPD, PANalytical) at room temperature (RT) with a monochromatic CuKα radiation source (λ = 0.154 nm) in the step-scan mode with a 2θ angle ranging from 5° to 70° with a step of 0.067° and scanning time of 6.0 min.

Diffractograms of all samples were smoothed, normalized to 2θ=70° and linear-subtracted as described in the work[156]. Average crystallite size, along c- and a- axis was determined using Scherrer equation[156,169,170] Eq 2.6.1 &Eq 2.6.2:

Eq 2.6.1 $$L_c = 0.89\lambda/B_c cos\theta_c$$

Eq 2.6.2 $$L_a = 1.84\lambda/B_a cos\theta_a$$

Where L_c, and L_a are the stacking height and the lateral size of the crystallite, respectively; λ is the wavelength of the used X-ray; B_c and B_a are respectively the full width half maximum (FWHM) of the (002) and (100) peaks from the diffractogram of each sample, whereas θ_c and θ_a are the corresponding scattering angles.

The interlayer spacing d_{002} was determined using Bragg's law: Eq 2.6.3

Eq 2.6.3 $$d_{002} = \lambda/2sin\theta_{002}$$

The number of crystallite layers per stack (N) was therefore calculated as: Eq 2.6.4

Eq 2.6.4 $$N = L_c/d_{002} + 1$$

2.6.8 Mechanical characterization

A dynamic mechanical analyzer DMA (TA RSA3) equipped with a three-point bending fixture (Lxlxh:10x12.5x19 mm) was used for mechanical characterization of MFC/LS/CP carbon precursor and the resulting carbons. The tested samples were 3D printed mono-lines that were (or not) subsequently carbonized to HTT from 400 to 1200°C. The standard of ISO 178 was followed except for the special dimensions of the samples. The cross section of each samples is approximately an ellipse. As a result, the corresponding section modulus was used to calculate the flexural stress and strain as well as elastic modulus. In order to estimate the uncertainty caused by dimension measurement and inhomogeneity, 6 different positions were measured in width and thickness by a Vernier caliper. The crosshead speed was set to 0.001 mm/s in order to obtain enough data before rupture. 3 samples per HTT were tested.

3. Results and discussion

3 Experimental results

3.1 Use of MFC/LS blends as carbon precursors: impact of hydrogel rheology on 3D printing

3.1.1 Introduction

The first study conducted during this thesis focused on the rheological characterization of MFC/LS hydrogels of different concentrations. A successful use of 3D printing for manufacturing the carbon precursors requires a deep investigation of the used "ink". For such purpose, LS and MFC suspensions were examined in separate and mixed form. Both flow mode and thixotropic mode were applied in order to test the usability of MFC/LS hydrogels in different printing conditions. The relationship between the rheological behavior of MFC/LS hydrogels and the 3D printing were concluded and evidenced by the photographs of the printed objects. Drying conditions and some basic physical properties of the printed-carbonized objects were also given with comparison to those from literature.

3.1.2 Pure LS/water solutions of different concentrations

Fig 3.1.1 shows that, regardless of concentrations, LS solutions displayed a Newtonian behavior with a progressive viscosity increase from 0.003 to 100 Pa·s when LS concentration rose from 20 to 55%. The rheological behavior of LS solutions was therefore described by plotting relative viscosity as a function of the volume fraction of dissolved LS (inset in Fig 3.1.1). Below a volume fraction of *ca.* 0.35, relative viscosities slightly increased with concentration, whereas, above that value an abrupt increase was observed and for LS volume fractions higher than 0.47 it was no longer possible to measure viscosity.

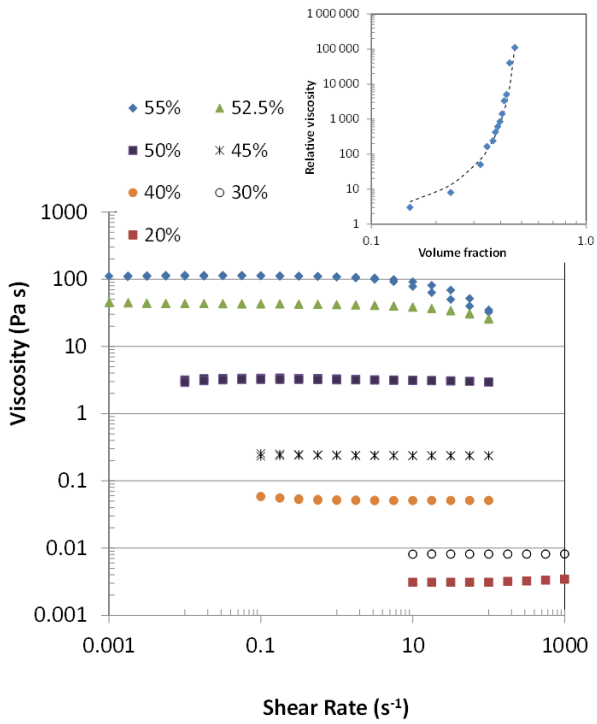

Fig 3.1.1 Rheological behaviours of LS solutions of different concentrations. The inset represents the relationship between relative viscosities and volume fractions. Full points and the dashed line represent experimental data and the fitting curve, respectively.

The Krieger-Dougherty equation(Eq 3.1.1)[94,95] was used to fit experimental data and to correlate the relative viscosity of the polymer solution (η_r) to its volume dissolved fraction (ϕ):

Eq 3.1.1 $$\eta_r = \left(1 - \frac{\phi}{\phi_m}\right)^{-[\eta]\phi_m}$$

where ϕ_m and $[\eta]$ are the maximum packing fraction (which corresponds to the critical phase volume at which the fluid's viscosity tends to infinity) and the intrinsic viscosity of LS, respectively.

Values obtained for ϕ_m and $[\eta]$, *i.e.* 0.49 and 8.14, were in line with those obtained by Vainio *et al.*[94] for similar systems, thus indicating that intermolecular interactions above a volume fraction of 0.49 lead to a fluid to solid transition and LS solutions are no longer processable by extrusion. In order to limit the viscosity of MFC/LS suspensions the maximum LS volume fraction used in this study was 0.42, corresponding to a LS mass fraction of 50% and a solution viscosity of 3.3 Pa·s.

3.1.3 Pure MFC hydrogels of different concentrations

Fig 3.1.2 shows that MFC hydrogels displayed a typical shear thinning behaviour[65,66], which is associated to the progressive destruction of the MFC network upon shearing and was modelled using the Herschel-Bulkley equations:

Eq 3.1.2 $$\sigma = \sigma_y + K\dot{\gamma}^n + \eta_s\dot{\gamma}$$

Eq 3.1.3 $$\eta = \frac{\sigma_y}{\dot{\gamma}} + nK\dot{\gamma}^{n-1} + \eta_s$$

where σ is the shear stress, σ_y the yield stress, $\dot{\gamma}$ the applied shear rate, η_s the viscosity of the Newtonian suspending medium (*i.e.* water or LS solutions), η the suspension viscosity, K the concentration factor and n the flow index which represents the fluid flow behavior (*i.e.* $n = 1$ Newtonian, $n > 1$ shear-thickening, $n < 1$ shear-thinning).

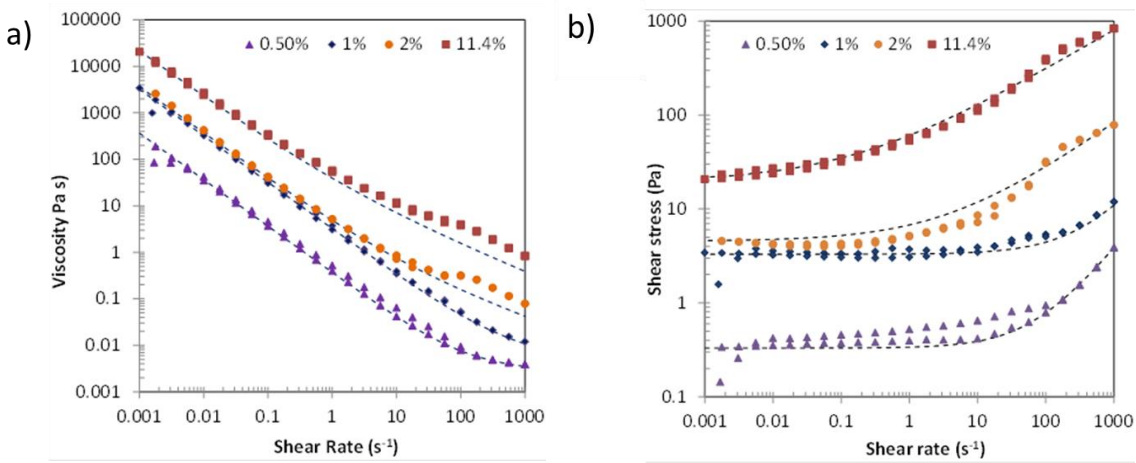

Fig 3.1.2 Viscosity (a) and shear stress (b) responses of MFC suspensions at 4 different concentrations in a shear flow. Dashed lines represent experimental data fitting with Eq 3.1.2 and Eq 3.1.3.

A rise in MFC concentration led to a general increase of the shear stress and viscosity, which was mainly due to the progressive formation of dense nanofiber networks opposing a growing resistance to shear[67]. The plot of the yield stress and the flow index values obtained from Eq 3.1.2 as functions of MFC concentrations (Fig 3.1.3), shows that the dilution to 0.5% of the pristine 2% MFC suspension led to the hydrogel disruption and a shift from shear thinning towards Newtonian behaviour (*i.e.* the yield stress dropped from 4 to 0.3 Pa, and flow index increased from 0.5 to 0.85).

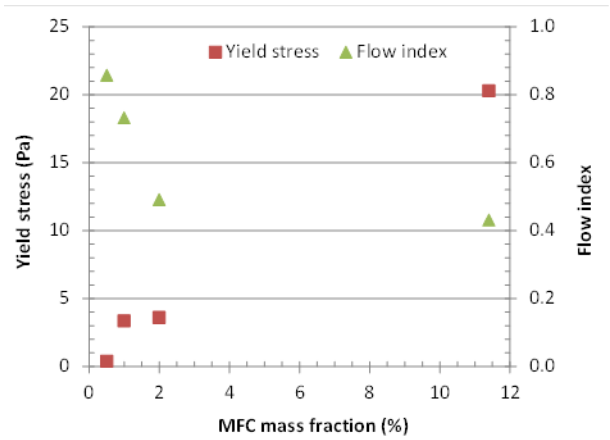

Fig 3.1.3 Yield stress and flow index of MFC suspensions obtained from experimental data fitting with Eq 3.1.2

Despite a high viscosity at low shear rate, the pronounced shear thinning and high yield stress of 2 and 11.4% MFC suspensions led to hydrogel fluidization in the printing needle (for a shear rate of *ca.* 300 s^{-1}, 2% and 11.4% hydrogels dropped to *ca.* 0.1 and 2 Pa·s, respectively).

As highlighted in previous works[171], 3D objects can be easily printed. Whereas, 0.5% MFC suspensions behaved as low viscosity Newtonian fluids and spread over the printing substrate.

3.1.4 MFC/LS slurries of different concentrations

Flow curves for mixed MFC/LS suspensions show that, at 2% MFC (Fig 3.1.4a)), the increase of the LS concentration results in a general shift of the flow curve towards higher viscosity. This is in line with the viscosity increase in the suspending medium.

Whereas, at 1 and 0.5% MFC (Fig 3.1.4b) &c)), LS addition induced a drop in viscosity at shear rates below ca. 100 and 10 s^{-1}, respectively. Above those shear rate values, the viscosities of MFC/LS systems were higher than those of pure MFC gels indicating that at low shear rates the viscosity of MFC/LS mixtures is dictated by the disruption of weak MFC networks. At high shear rates, the rheology is dominated by the viscosity of the suspending medium. Regardless of MFC concentrations, in the presence of 50% LS, the viscosity of MFC/LS systems was higher than that of the pristine MFC hydrogel and at high shear converged to η_s.

The plots of the yield stress values obtained from fits of Eq 3.1.2 to the experimental data (Fig 3.1.5) show that at concentrations below 30%, LS induced a drop in the MFC gel strength. Indeed, a drop in yield stress was clearly detected with 1 and 0.5% MFC. At a MFC concentration of 2%, only a slight decrease was observed.

As highlighted for diluted MFC/soluble polysaccharides mixtures[172], the sharp decrease in the yield stress at extremely low LS concentration (*i.e.*, 0.5% LS) is associated with the adsorption of LS on the fiber surface; the adsorbed LS, acting as lubricant, decreases the friction among nanofibers and the stress necessary to break the entangled nanofiber network. Increasing the LS concentration from 0.5% to 30% poorly affected the yield stress, thus indicating that over this LS concentration range the LS no longer affects the interfiber friction. Therefore, we can go on the assumption that between 0.5% and 30% LS, the fiber surface is saturated by adsorbed LS molecules and their effect on interfiber lubrication attains a steady state. Moreover, dissolved LS molecules have limited or no effect on fiber interactions. The minor effect of LS on the yield stress at an MFC concentration of 2% is ascribed to the formation of dense networks of entangled fibers, where interfiber friction is supposed to make a minor contribution to the yield stress compared with the mechanical fiber bending and deformation necessary to break the MFC network.

Above a LS concentration of ca. 30-40%, corresponding to an abrupt increase in the viscosity of the LS solution (Fig 3.1.1), the yield stress increased for all tested MFC concentrations attaining values close to that of pristine MFC hydrogels.

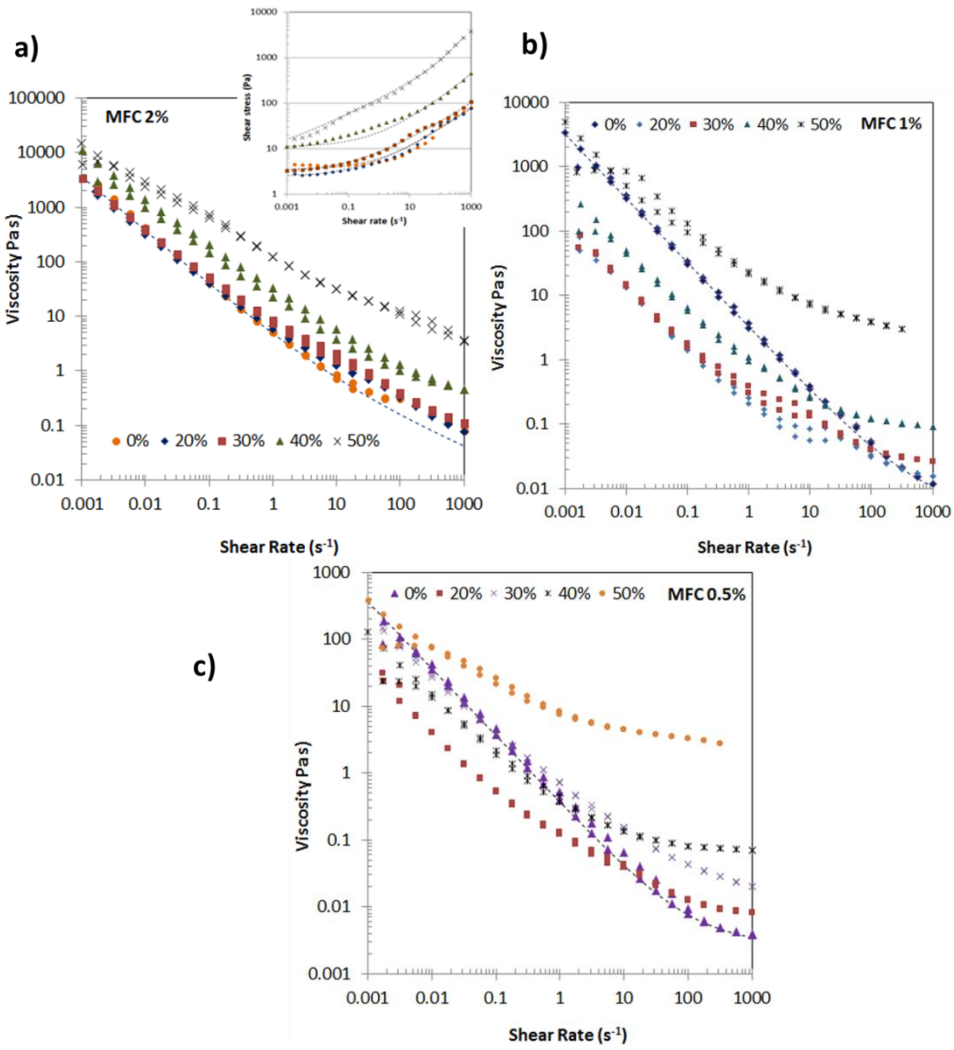

Fig 3.1.4 Plots of viscosity vs shear stress for MFC/LS systems: (a) 2% MFC series (the inset shows shear stress vs shear rate data); (b) 1% MFC series; (c) 0.5% MFC series. Dashed lines represent fits of Eq 3.1.2 and Eq 3.1.3 to the experimental data.

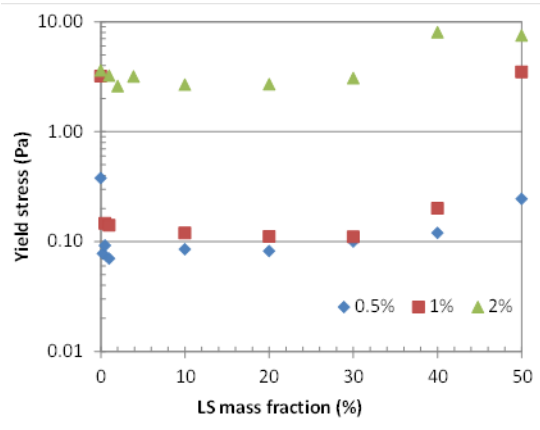

Fig 3.1.5 Influence of the MFC mass fraction (colored symbols) and the LS mass fraction on the yield stress. The yield stress values were obtained from fits of Eq 3.1.2 to the experimental data.

At high LS concentration, interfiber lubrication by LS plays a secondary role and the strength of the MFC network is supposed to be mainly affected by the high viscosity of the suspending medium, which, by decreasing fiber mobility, increased the stress necessary to break the MFC network (*i.e.* the yield stress).

Overall, at concentrations below 30% the viscosity of LS solutions is below 10 Pa·s, and LS lubricates nanofiber contact nodes and favors their relative motion and network disruption when shear is applied. At higher concentration, the high viscosity of LS solutions ($\eta > 70$ Pa·s) screens the lubricating action by inducing a drop in fiber mobility thus restoring the resistance of the network to shear.

3.1.5 Thixotropy of mixed slurries

Under oscillatory deformation, MFC suspensions are characterized by viscoelastic response with high storage modulus and low phase shift[172,173]. This quasi-elastic behavior indicates that structural changes in the MFC network (*i.e.*, breakdown and rebuild) induced by variations in the shear rate occur with no or short time delay. Nevertheless, Sorvari *et al.*[172] showed that carboxymethylcellulose (at a concentration of 0.11%) increased the viscosity of the suspending solution up to ~80 Pa·s and the viscous behavior of the MFC hydrogel, corresponding to an increase in the time delay for structure change in the MFC network.

In order to investigate the role of LS in affecting the MFC network rebuild kinetics, MFC/LS suspensions were subjected to a step-down shear variation simulating the shear conditions applied during the suspension extrusion through the 3D printer needle. Network rebuild after shearing was described using a first-order kinetic model to describe the response of the MFC/ LS suspension[71]:

Eq 3.1.4
$$\sigma(t) = \sigma_0 + (\sigma_\infty - \sigma_0)\left(1 - e^{-\frac{t}{\tau}}\right) + \eta_s\dot{\gamma}$$

where σ_0 is the shear stress immediately after the step-down variation in the shear rate, σ_∞ is the shear stress after an infinite time, τ is the time constant, and η_s is the viscosity of the Newtonian surrounding medium (*i.e.*, the bare LS solution). Fig 3.1.6 shows that in MFC/LS systems with LS concentrations below 30%, the shear stress exhibited a quick monotonic decrease, reflecting the viscoelastic response of the MFC network to the sudden shear variation[174]. The time constant obtained from fits of Eq 3.1.4 to the data progressively increased from 4 to 7 s as the LS concentration increased from 0% to 30%, thus indicating that LS slowed the response of the MFC network.

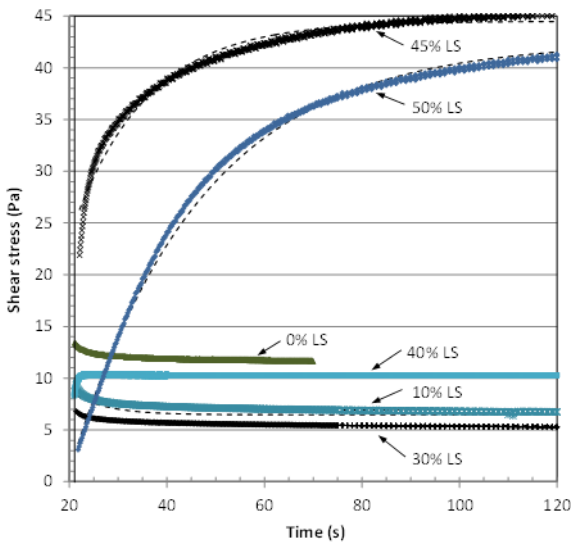

Fig 3.1.6 Shear stress responses to the step-down experiments for the 2% MFC series. The shear rate dropped from 1000 to 0.1 s−1. Dashed lines represent fits of Eq 3.1.4 to the data.

The shear stress drop and subsequent increase until stabilization observed at an LS concentration of 40% revealed a transition from viscoelastic behavior to inelastic thixotropic behavior. As a result of the increased viscosity of the LS solution, rebuilding of the MFC network was delayed and, as observed for papermaking fibers[175], occurred progressively after the step-down shear variation. Increases in the LS concentration up to 45% and 50% further emphasized the thixotropic response, with increases in the time constant from 0.7 s at 40% LS to 14 and 27 s at 45% and 50% LS, respectively.

3.1.6 Relationship between the rheology and hydrogel printing

As illustrated in Fig 3.1.7, square cuboids with good spatial definition (*i.e.*, sharp edges and no spreading of the cuboid base on the substrate) were printed using the bare (2%) MFC hydrogel. Additions of LS led to a progressive degradation of cuboid shape:

i. With up to 30% LS, the cuboid base was subjected to ever-increasing spreading, and the height of the printed object decreased from about 9 to 2 mm as the LS concentration was increased from 0 to 30%. According to the experimental data shown in Fig 3.1.6, this behavior was associated with a decrease in the viscosity (from 130 to 60 Pa·s) at low shear rates.
ii. With 40% LS, the MFC/LS suspension completely spread over the printing substrate, and the thickness of the final liquid film was below 1 mm. This trend was ascribed to the transition from viscoelastic to inelastic thixotropic behavior. Indeed, after shearing in the extruder needle and destruction of the MFC network, the flock rebuild kinetics was too slow and the fluid viscosity too low to stop the MFC/LS suspension from spreading over the printing substrate.
iii. With 50% LS, square cuboids were easily printed without major deformations. However, their edges displayed rounded profiles, indicating that the flow of the MFC/LS suspension did not stop immediately after extrusion. This behavior was

associated with the high viscosity of the suspending medium (η = 3.3 Pa·s), which, despite the pronounced thixotropic behavior and long MFC network rebuild time (τ = 27 s), slowed the spreading and provided sufficient time for network rebuild and object geometry "freezing" before major deformations were induced.

As highlighted in Fig 3.1.7, only the samples with LS concentrations of 0−10% and 50% held the pristine geometry after printing. However, with 0−10% LS, freeze-drying was necessary to hold the original shape since air drying induced extensive shrinkage. With 50% LS, air drying led to a limited deformation of the square faces and 40% shrinkage along the vertical axis, which for the purpose of this study was considered acceptable.

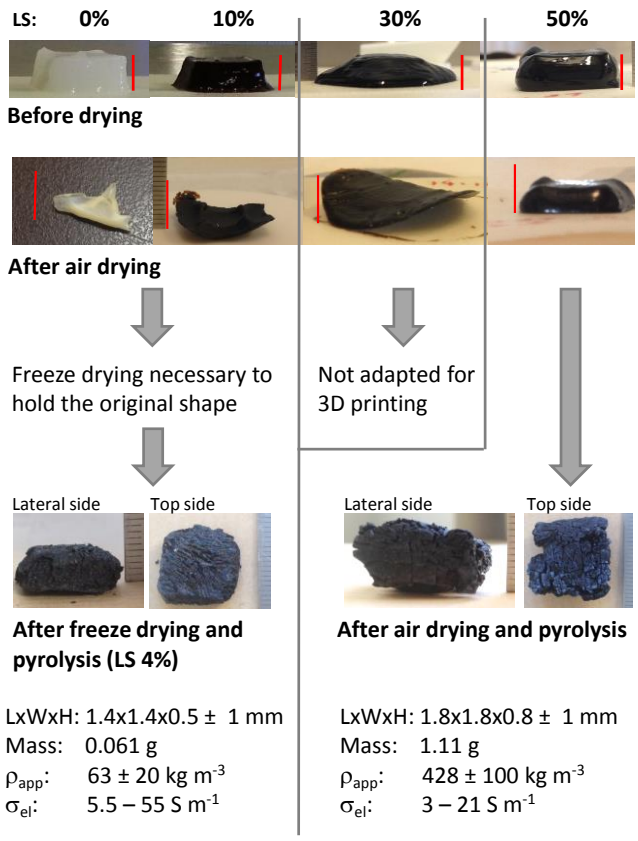

Fig 3.1.7 Shape and main characteristics of 3D printed cuboids before and after drying and carbonization. The red line represents a length of 10 mm.

3.1.7 Characterization of printed aerogels before and after pyrolysis

X-ray tomography of the cuboid sections (Fig 3.1.8) showed that before and after carbonization, the freeze-dried sample containing 4% LS (corresponding to a dry sample composition of 33.3% MFC and 66.7% LS) displayed a lamellar structure associated with solute accumulation at the boundaries between ice crystals, which acted as template[176,177]. According to the slow convective freezing used in this study, Fig 3.1.8 shows fine and continuous lamellar structures originating from the cuboid surface, converging to the cuboid core, and forming a continuous network. After carbonization, this particular structure led to the formation of an extremely light carbon cuboid with an apparent density of ca. 63 kg m^{-3} and an electronic conductivity of *ca.* 5.5−55 S m^{-1}.

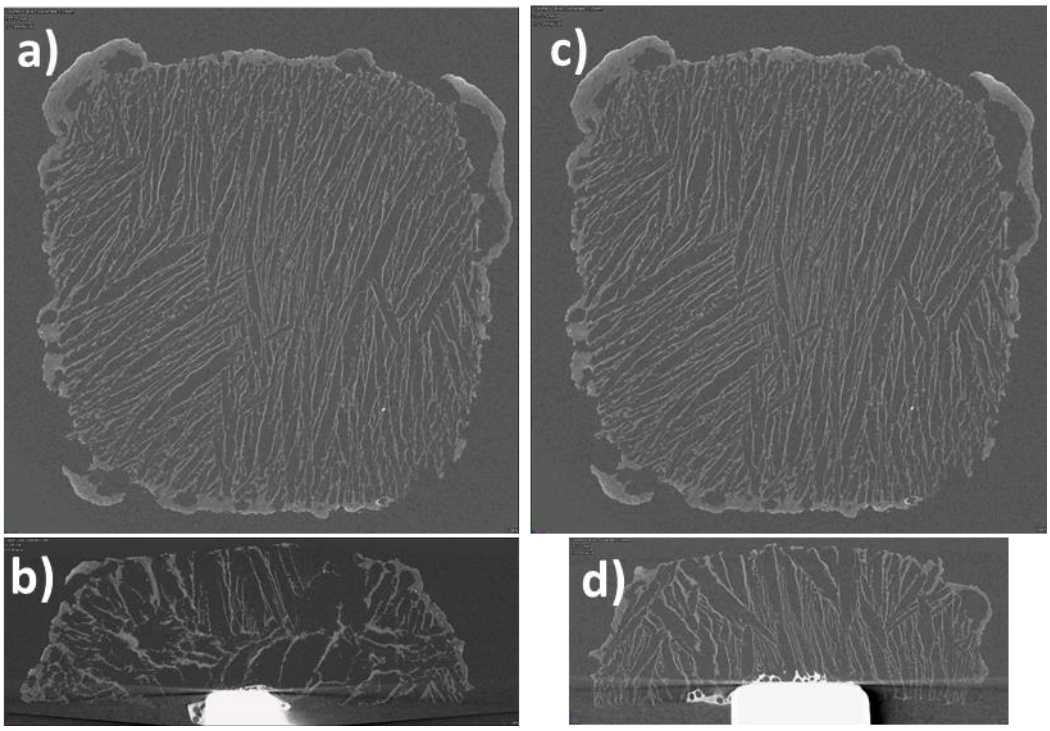

Fig 3.1.8 X-ray tomography sections of freeze-dried cuboids from 2% MFC/4% LS suspension (*i.e.*, 33.3% MFC and 66.7% LS in the dry sample): a) and b) before pyrolysis; c) and d) after pyrolysis

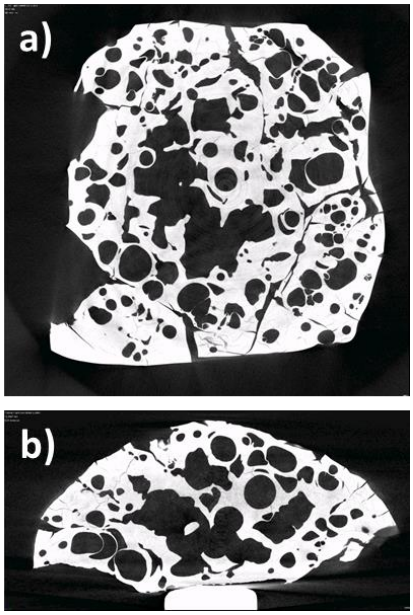

Fig 3.1.9 X-ray tomography sections of air dried cuboids from the 2% MFC/50% LS suspension (*i.e.*, 3.8% MFC and 96.2% LS in the dry sample).

For the sample containing 50% LS, the lamellar structure was absent after freeze-drying, and the solid phase displayed the presence of fine cracks, presumably due to the formation of small ice crystals. As highlighted for inorganic hydroxyapatite particles[177], this morphology change was interpreted as indicating that LS was not repelled from the ice front during crystal growth.

The air-dried sample with 50% LS (corresponding to a dry sample composition of 3.8% MFC and 96.2% LS) had high internal porosity with macropores and large cracks (Fig 3.1.9). This irregular structure was associated with the presence of large amounts of residual water in the sample before carbonization. Indeed, as determined by direct weighing, the water content decreased from 64% to 38% and 30% (w/w) after drying in air and at 110 °C, respectively. Despite the high density of the continuous phase (highlighted by the pronounced contrast in the X-ray tomography images) and the high apparent density of the carbonized cuboid (*i.e.*, 428 kg m^{-3}), the electronic conductivity along the Z axis was lower than that of the freeze-dried sample, (*i.e.*, 3−21 S m^{-1}). This difference is associated with discontinuities in the conductive path generated by macropores and cracks. This work shows that microfibrillated cellulose/lignosulfonate hydrogels appear to be promising bio-sourced precursors for the manufacture of carbon objects with simple geometries by 3D printing and carbonization. Even if several aspects concerning the control of object shaping by 3D printing and its geometric stability during drying/carbonization remain to be explored, carbon cuboids obtained by freeze-drying from a dry precursor made of 33% MFC and 67% LS displayed interesting properties (*i.e.*, low density, geometric stability, and homogeneous structure). Moreover, compared with carbon materials obtained from other wood-derived precursors (see Table 3.1.1), they display extremely low density and good electric conductivity, making them promising materials for the manufacture of 3D-structured porous electrodes for energy storage devices.

Table 3.1.1 Comparison of electrical conductivity of wood-derived carbon materials.

Reference work	Conductivity (S m-1)	Density (kg m-3)	Physical form	Precursor
This work	5.5-55	63 ± 20	3D printed cuboid	MFC/Lignosulfonate blend
Teng *et al.*[178]	2.3-3	nd	Fibre, 639-816 nm diameter	Kraft Lignin/MW Carbon Nanotube blend
Snowdon *et al.*[179]	0.9	nd	Powder compressed at 1.12 MPa	Hydrolysis Lignin
Deraman *et al.*[180]	243-500	1000	Bulky pellet	Lignin/precarbonized carbon
Rhim *et al.*[10]	10000	2000	Bulky pellet	Microcrystalline cellulose
*Lu *et al.*[181]*	90-2000	65-600	Monolithic aerogel	Polycondensed resorcinol-formaldehyde gel
*Sanchez-Gonzalez *et al.*[182]*	44-215	250-700	Compressed carbon black	Carbon black

*Carbon from sources other than wood given for comparison

3.1.8 Conclusions

MFC/LS systems displayed a complex rheological behavior that was affected by the LS concentration. At low concentrations (*i.e.*, below 30%), LS acted as a lubricant, favoring shear-induced disruption of the MFC network and inducing a progressive decrease in both the yield stress and viscosity. The print quality of the cuboids underwent progressive degradation

due to spreading of the MFC/LS over the printing surface, and 10% was the maximum LS concentration that could be used to print cuboids.

At intermediate LS concentrations (ca. 40%), the MFC/LS suspensions shifted from viscoelastic to inelastic thixotropic fluids with complete degradation of the print quality, *i.e.*, the MFS/LS suspension completely spread over the printing substrate. At high LS concentrations, the print quality the cuboids was restored since despite the pronounced thixotropic behavior, the high viscosity of the suspending medium slowed the fluid spreading during printing, thus providing sufficient time to rebuild a continuous MFC network and "freeze" the cuboid geometry.

Freeze-drying and carbonization of cuboids printed using MFC/LS suspensions with a maximum LS concentration of 10% yielded carbon cuboids with minimal shape variations that displayed an ice-templated continuous lamellar structure, extremely low apparent density (ρ_{app} = 63 ± 20 kg m^{-3}), and high electrical conductivity (σ = 5.5−55 S m^{-1}). Because of the high dry material content, cuboids printed with 50% LS suspensions underwent acceptable shrinkage upon air drying and carbonization. Nevertheless, despite interesting conducting properties, large defects (*i.e.*, macropores and crackles) generated during drying led to a heterogeneous and brittle object.

Overall, this study demonstrates that MFC/LS hydrogels have the potential to be used as biosourced precursors for the manufacture of 3D-printed carbon objects, but work remains to be done to demonstrate the level of control that would be necessary for a manufacturing environment.

3.2 Use of MFC/LS blends as carbon precursors: pyrolytic process characterization and kinetics study

3.2.1 Introduction

At the end of the chapter 3.1, conductive and self-standing objects were successfully elaborated using 3D printing and the subsequent pyrolysis. Since pyrolysis is the fundamental process that transforms carbon precursors into engineering carbons and plays a significant role in determining carbons' properties (morphology, electrical conductivity, *etc.*), a further study of the thermal degradation of MFC/LS composites and their kinetics is quite necessary. This second part of chapter 3 presents the thermal characterization of MFC/LS blends using TGA/MS. The kinetic analysis was conducted using both model-free and mode-based methods. Arrhenius parameters were given for MFC and LS separately as well as in composites.

3.2.2 Morphological and structural characterization

MFC and NaLS alone, together with one of their composite are observed under SEM, as shown in Fig 3.2.1. MFC nano-paper, made by water evaporation from the original 2% aerogel, is in the form of a thin film in macroscale, whereas in microscale, it consists of a stack of micro-layers in the thickness direction (Fig 3.2.1b))[183]. Each micro-layer is formed by cellulose microfibrils entangling with each other and exhibits a web-like structure[184,185], as observed in Fig 3.2.1a). Dimensions of single microfibril of cellulose are beyond the maximal resolution of the SEM to be distinguished. Dissimilarly, industrial NaLS is in powder-form and SEM image shows that these powders are essentially spherical but hollow (indicated by arrows in Fig 3.2.1c) with diameters ranging between 20 and 135 μm[90]. Composite of NaLS and MFC (66% and 33%, respectively) is examined on fraction surface and as shown in Fig 3.2.1d). A sheet-like structure of MFC can be observed as in pure MFC film, whereas NaLS, blended previously with MFC in suspension state, acts like "glue" which surrounds MFC sheets spatially and sticks them together in transversal direction to form a compact stack after water evaporation.

Fig 3.2.2a) illustrates chemical structures patterns of single MFC, NaLS along with their composites using FTIR. Characteristic bonds of MFC and NaLS are identified directly in Fig 3.2.2b), with good similarity to those reported in the literature[186–188]. MFC/NaLS blends do not present other chemical bonds than those inherited from single MFC and NaLS. Besides, the specific bands related to each constituent are more or less pronounced depending on the fraction of MFC and LS in the composite.

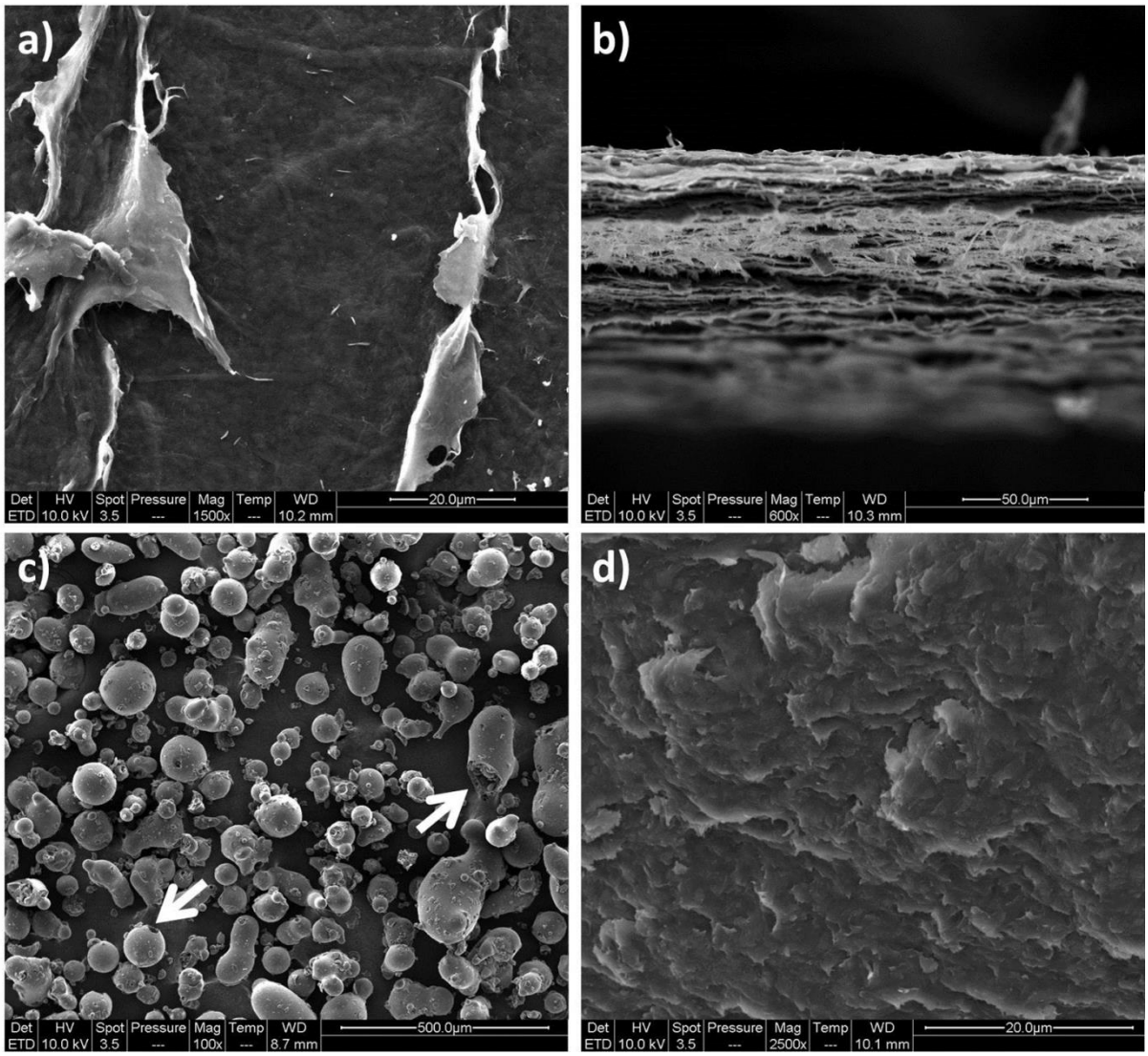

Fig 3.2.1 SEM micrographs of: (a) MFC film surface; (b) MFC film in transversal sense: (c) NaLS powder (arrows indicate the hollow nature of NaLS); (d) NaLS/MFC composite (66%/33%) in fraction surface

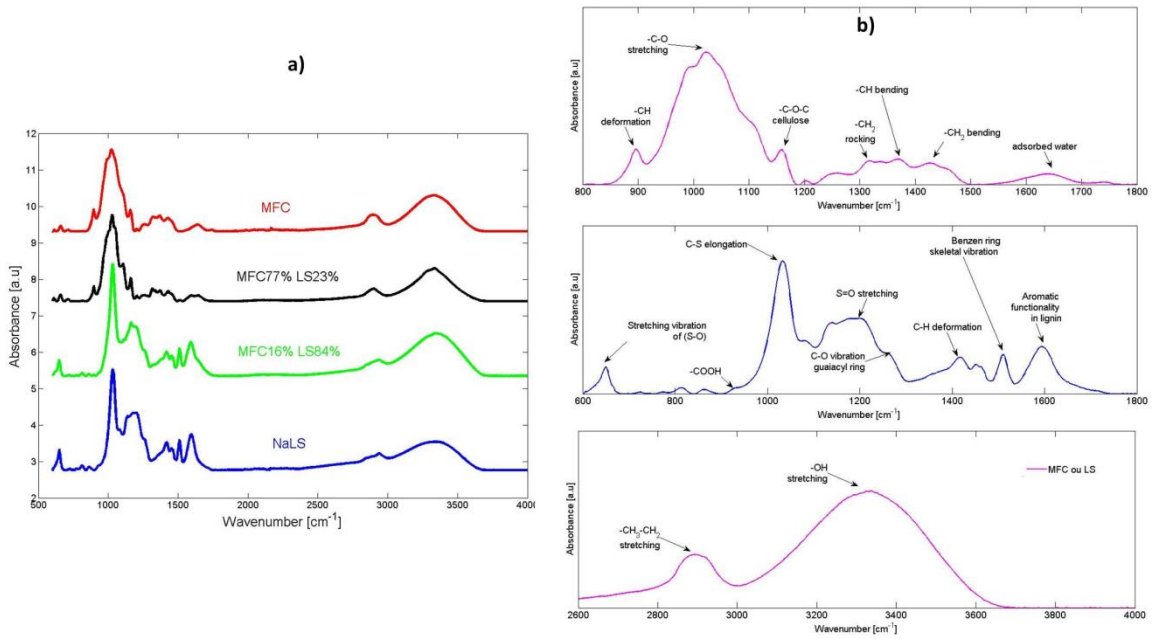

Fig 3.2.2 FTIR spectra of MFC/NaLS composites of various ratios: (a) global comparison; (b) characterization of chemical bonds in MFC and NaLS as a function of wavenumber

3.2.3 Thermal characterization

Thermal degradation patterns of MFC and NaLS as well as their different composites are presented in Fig 3.2.3. One can see on this figure that the thermal degradation characteristics of MFC and NaLS are quite different. Unsurprisingly, MFC presents a very similar thermal decomposition pattern to that of cellulose as reported in the literature[122–125] since they both have the same chemical structure owing to their common cellulose nature. Pure cellulose decomposes mainly from 250°C to 400°C and exhibits a sharp reaction peak at around 334°C. In the end of pyrolysis, the carbonaceous char is formed and weights slightly more than 20% of the initial mass of the sample. Compared to MFC, DTG curve of NaLS is more complicated and is composed of two successive reaction peaks (at 239°C and 291°C) and four visible shoulders (at around 200, 330, 410 and 665°C, respectively), not far from previous reports concerning LS degradation[129,131,189]. NaLS thermal degradation starts around 150°C. Its thermal degradation process takes place in a large temperature range up to 800°C. Nevertheless, NaLS degrades more mildly than MFC and thus results higher char yield at around 47%[90].

Composites of MFC and NaLS seem to combine the thermal behavior of both pristine materials. They appear also to exhibit more similar thermal degradation patterns to the predominant constituent in them. For instance, compared to pure MFC, adding 23% of NaLS into MFC makes such a composite to degrade more prematurely with a shift of maximum reaction rate towards lower temperatures by 26°C whereas the morphology of its DTG curve still recalls the characters of cellulose decomposition. Likewise, when the content of NaLS in the composite becomes predominant, which is the case for the composite of 16% MFC and 84% NaLS, it follows roughly the degradation pathway of single NaLS. The comparatively huge

peak at around 250°C that this composite shows is most probably the superposition of one reaction peak of NaLS originally at 239°C, and the characteristic peak of MFC decomposition initially at 334°C in pure MFC pyrolysis. This peak shifts towards lower temperature regions with increasing NaLS content in the composite. Char mass increases with increasing NaLS content in the composites, except for the composite with 84% NaLS. The latter gives a char yield slightly higher than in pure NaLS.

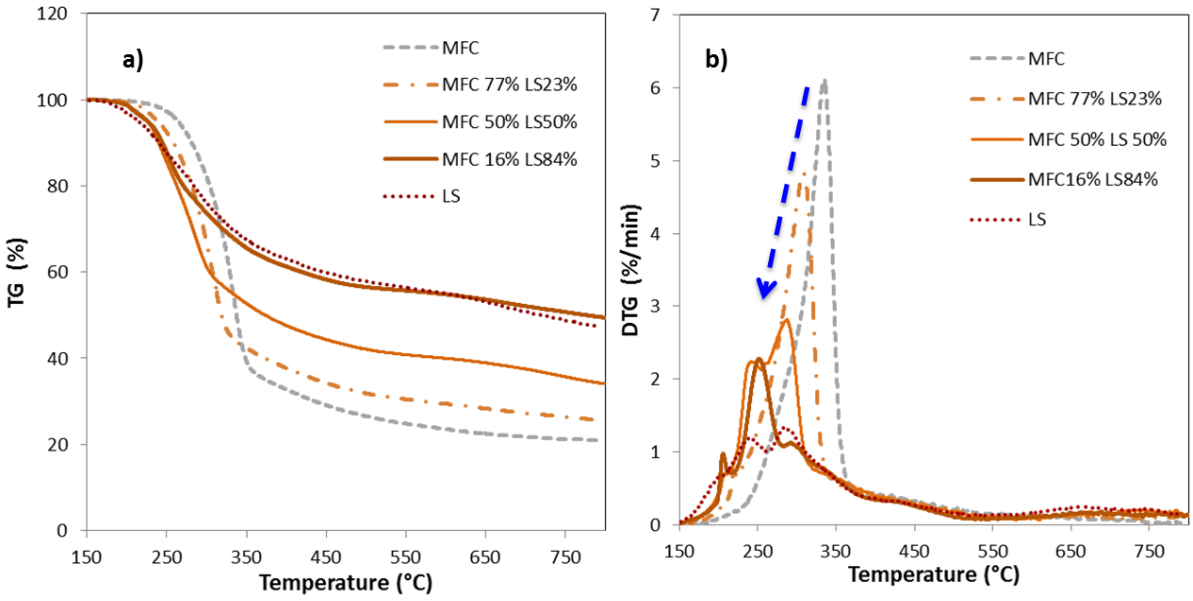

Fig 3.2.3 (a) TG and (b) DTG curves of MFC, NaLS (shorted to LS) and their composites (the arrow indicates the shift of characteristic peak of cellulose)

3.2.4 Catalytic effect of sodium

For composites where the MFC content is predominant (MFC: 77%, 67% and 50%), the shift of characteristic peak for cellulose decomposition, that is indicated in Fig 3.2.3b) by an arrow, is thought to be due to the catalytic effect of sodium ions that NaLS brings in[129,189]. Although NaLS degrades earlier and slower than MFC, there are no reasons - except interactions between NaLS and MFC- to shift the degradation peaks at low temperatures. In the absence of interactions, the composites should degrade following a TG/DTG curve which would correspond to the linear combination of that of the pure MFC and NaLS. The theoretically predicted TG/DTG curves are calculated according to Eq 3.2.1 or Eq 3.2.2 based on the experimental TG/DTG data of MFC and LS obtained separately. As shown in Fig 3.2.4 a) and b), obvious differences between the "theoretical" curves and the experimental ones are obtained for both MFC-predominant composites. When the NaLS content rises from 23% to 50%, the sodium content in the composite increases from 2% to 4.5%, making cellulose in these composites to decompose earlier and earlier due to an increasing catalytic effect. The peak temperatures shift to 308°C, 296°C, and 283°C, respectively for composites with 77%, 67% and 50% of MFC, in comparison with the peak temperature observed at 334°C for pure MFC. The discrepancies between the theoretical additive curves and the experimental ones are more pronounced with increasing sodium content. Reasonable explanation should still behind the catalytic effect of Na that makes cellulose characteristic peak to get closer to that

of NaLS. Therefore, because of the "superposition effect", the characteristic region of NaLS is reinforced and appears more obviously in DTG curves of composites.

The temperature shift ΔT_p (representing the difference between the observed peak temperature in the composite and that observed in pure MFC) is plotted as a function of the Na content in the composite as shown in Fig 3.2.5a). One can observe a clear linear dependence between these two variables, which strongly suggests that the presence of Na is the main reason for the peak shift in the DTG curves.

Furthermore, we investigated the effect of NaCl impregnation on MFC on its thermal behavior. The results are plotted in Fig 3.2.5b) and suggest that sodium ions, introduced otherwise into MFC, are indeed capable of decreasing MFC reaction rate as well as shifting the degradation peak to lower temperature regions. However, compared to MFC/NaLS blends, the different mobility of Na^+ together with the presence of chloride ions in MFC/NaCl mixture catalyze MFC pyrolysis in a slightly different way by yielding a smaller ΔT_p despite the higher Na content.

Eq 3.2.1 $$TG(T)_{Theoretical\ additivity} = \%MFC \times TG(T)_{MFC} + \%LS \times TG(T)_{LS}$$

Eq 3.2.2 $$DTG(T)_{Theoretical\ additivity} = \%MFC \times DTG(T)_{MFC} + \%LS \times DTG(T)_{LS}$$

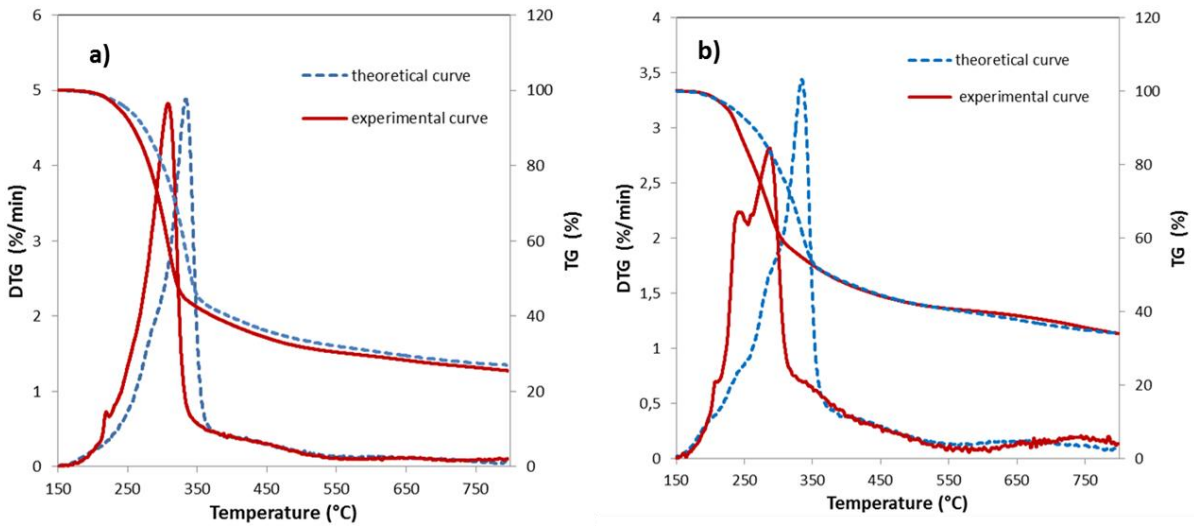

Fig 3.2.4 Comparison of theoretical and experimental TG/DTG curves for two MFC-predominant composites: (a) MFC77% LS23%; (b) MFC50% LS50%

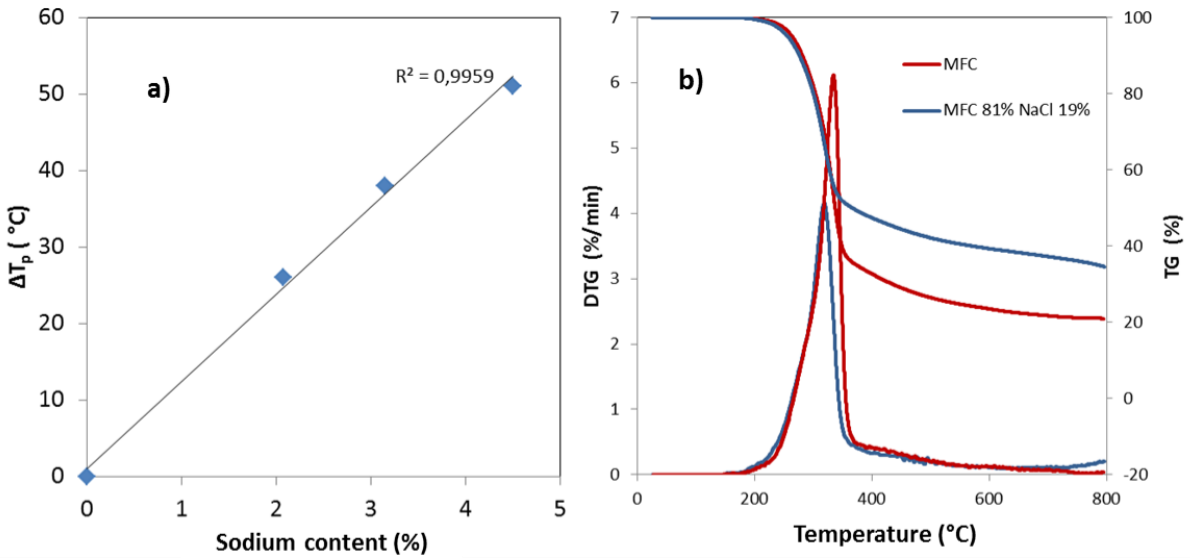

Fig 3.2.5 a) Influence of sodium content on the observed ΔTp in the MFC/NaLS blends; b) Evidencing the catalytic effect of Na by the TG analysis of MFC/NaCl blend

In the study of Wang *et al.*[190], it was observed that not only NaCl, but also other sodium compounds, such as Na_2CO_3, NaOH and Na_2SiO_3, could make wood decomposition to take place under lower temperatures. Sodium ion can penetrate into the biomass textures and break the intermolecular hydrogen bridges under swelling or heating[190,191]. As a result, devolatilization occurs earlier.

3.2.5 Pyrolysis gas analysis by mass spectrometry (MS)

Fig 3.2.6 illustrates the intensity evolution of the major pyrolysis products throughout the high temperature pyrolysis of the different MFC/LS composites. The TG/MS experiments were performed without a calibration of the mass spectrometer. The intensities obtained for the selected molecules were blank corrected considering the signals obtained for pure Helium gas, and normalized to the initial sample mass. The results presented in Fig 3.2.6 can only be compared qualitatively[192]. The intensity evolution of H_2O molecule roughly follows the features of the DTG curve regardless of the sample , which is in agreement with the fact that water is the most important volatile product[131,189]. It is believed that the cracking of alphatic hydroxyl groups (-OH band at 3350cm^{-1} in Fig 3.2.2b) for both MFC and LS) in the lateral chains generates water[131]. Another strongly emitted gaz is carbon dioxide. According to MS plot of CO_2, the decarboxylation reaction is apparently composed of two stages: the first one begins quite early around 150°C and lasts continuously till 500°C; the second stage takes place between 500 and 700°C and is particularly remarkable for pure NaLS sample. The complicated evolution of CO_2 emission should be attributed to the various functional groups existing in MFC and NaLS, including carboxyl, carboxylate, ester, carbonate groups among others. The specially strengthened decarboxylation in NaLS at around 640°C is possible to be a result of the decomposition of Na_2CO_3, an intermediate matter produced during pyrolysis[129]. Distinguished from CO_2, CO is released quite late in the temperature range of 650 to 750°C for NaLS, in contrast with MFC, for which the CO intensity reached its maximum at around

325°C. Surprisingly, composites (LS23% and LS84%) do not present an obvious emission maximum at around 700°C as LS does, which seems that MFC inhibits the CO production during their high-temperature devolatilization stage. Moreover, a large amount of alkyls and aromatic alkenes with various molecular masses are released during intermediate temperature range. The most important product, methane (*m/z*=15), whose emission evolution gives a clue concerning the demethylation of biomass that consists of two successive reaction peaks at approximately 300 and 500°C regardless of the sample. Decomposition of sulfonates, where the latter are represented by S-O band (650 cm^{-1}), C-S band (1028 cm^{-1}) and S=O band (1200cm^{-1}) in FTIR results in Fig 3.2.2b), is examined according to H_2S and SO_2 emissions[193,194]. SO_2 is strongly released at early stage from 200 to 350°C in NaLS, signifying that the sulfonic acid group is rather thermally instable. It is interesting to observe that although H_2S is not largely present during pure NaLS pyrolysis, whereas it is strongly released in the composite MFC16%/LS84%. It is reasonable to assume that MFC could strengthen the H_2S production from NaLS but the true mechanism has to be further investigated.

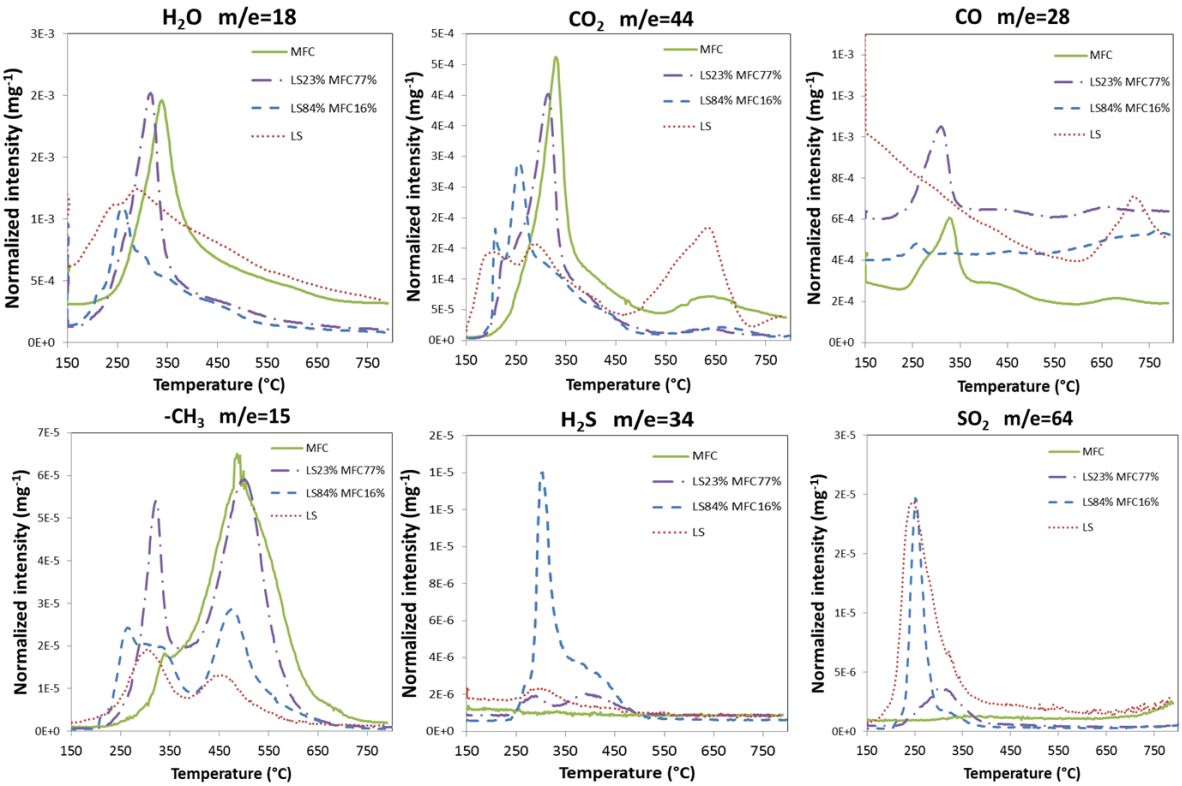

Fig 3.2.6 MS plots of major pyrolysis gases during the TG experiments of the different MFC/LS composites

3.2.6 Kinetic analysis

3.2.6.1 Estimation of activation energies by KAS isoconversional method

KAS isoconversional method is employed to estimate the activation energies at the different conversion level (0.1-0.9) during the pyrolysis of MFC and NaLS up to temperature of 500°C. Arrhenius plots for both materials based on four heating rates are presented in Fig 3.2.7.

Highly linear relationship between $\ln(\beta_j/T_{\alpha,j}^2)$ versus $1/T_j$ confirms the hypothesis that activation energy should be constant at fixed conversion regardless of heating rates. Activation energies for each conversion level are resumed in table.1.

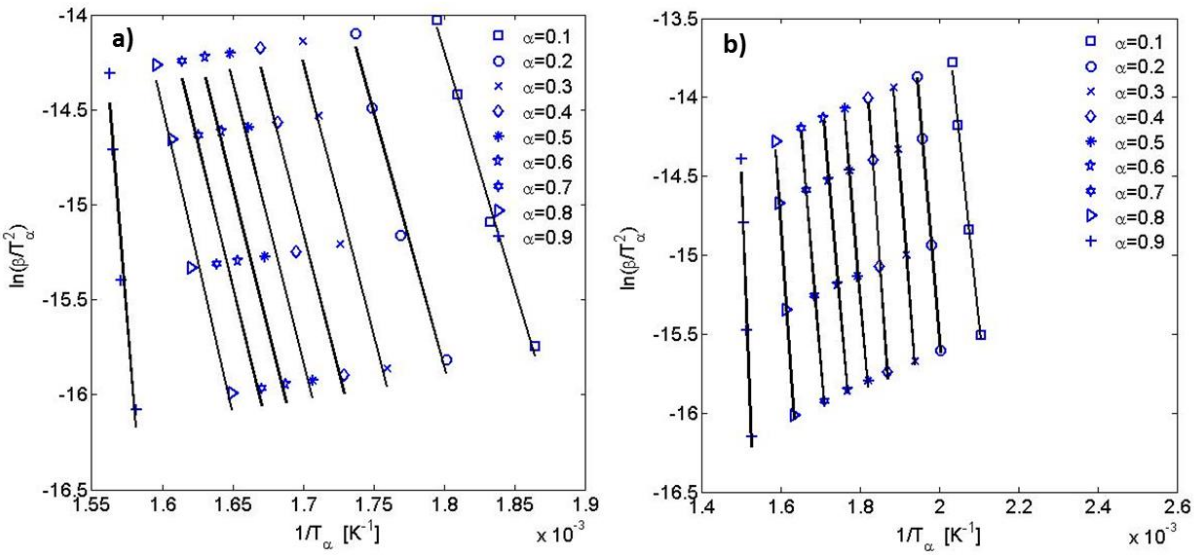

Fig 3.2.7 Arrhenius plot for (a) MFC and (b) LS at conversion levels from 0.1 to 0.9

Table 3.2.1 Activation energies provided by KAS method

α	MFC		NaLS	
	E_a (kJ/mol)	R^2	E_a (kJ/mol)	R^2
0.1	206.62	0.994	197.49	0.996
0.2	223.37	0.984	243.77	1.000
0.3	237.9	0.962	264.82	0.999
0.4	240.45	0.952	299.26	0.994
0.5	244.86	0.947	246.57	0.996
0.6	248.02	0.945	235.91	1.000
0.7	253.69	0.957	246.8	0.999
0.8	268.77	0.969	307.07	0.996
0.9	763.78	0.959	542.19	0.984

It can be seen from Table 3.2.1 Activation energies provided by KAS method that *E* varies at different conversion levels for both MFC and NaLS. At most of conversion levels, MFC has an activation energy that varies between 206 and 270 KJ/mol and rises with increasing conversion content. *E* of NaLS increases sharply at first (from 197 to 300 KJ/mol, when α rises from 0.1 to 0.4), and then followed by a slight decrease back to 246 KJ/mol for α from 0.5 to 0.7. *E* values for MFC thermal degradation are quite comparable with those provided in the literature and will be detailed in the following section. However, to the authors' best knowledge, no kinetic data for NaLS thermal degradation are published. For both MFC and

NaLS, an abnormal divergence of E could be observed at α>0.8, which demands further investigation.

3.2.6.2 Kinetic triplets provided by model-fitting method

The number of pseudo-components required for modeling was rather difficult to fix *a priori*. Especially for the LS sample, which exhibited a quite complicated DTG curve pattern, indicating the occurrence of several reactions taking place in different temperature ranges. The choice was made leaning on the DTG curve shape (peaks, shoulders) as well as on the MS spectra. According to conversion features of MFC and NaLS, they are deconvoluted into 4 and 6 pseudo-components, respectively.

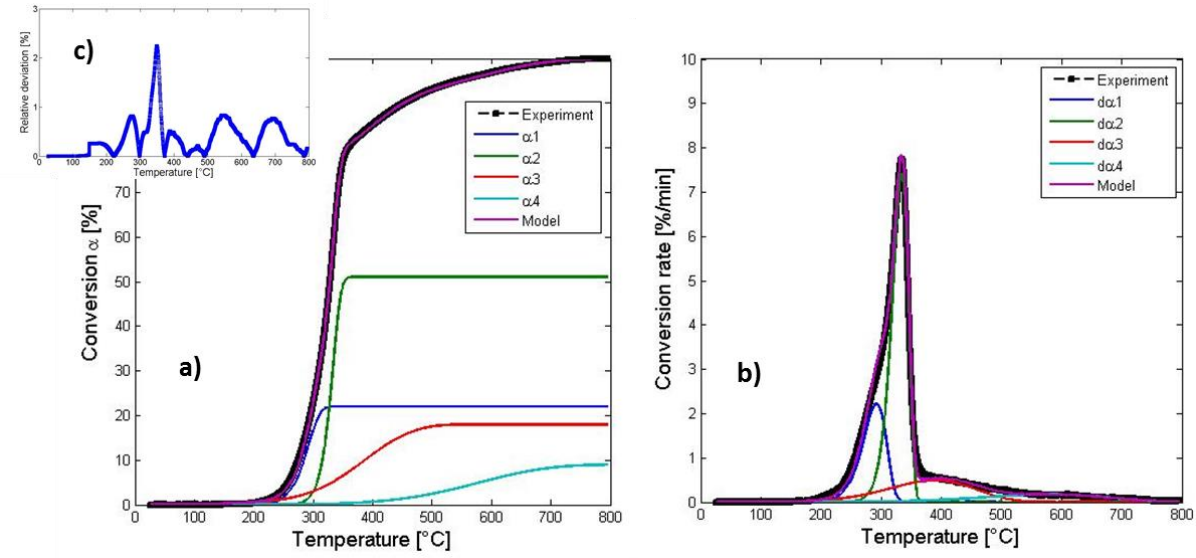

Fig 3.2.8 Kinetic modelling of MFC: (a) TG modelling; (b) DTG modelling; (c) relative deviation

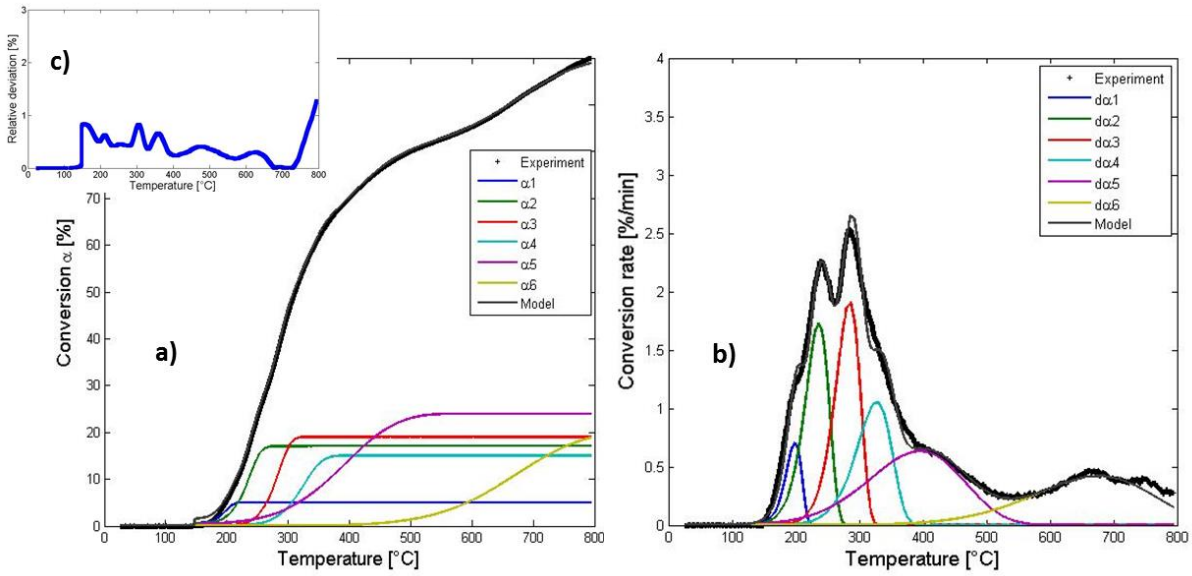

Fig 3.2.9 Kinetic modelling of NaLS: (a) TG modelling; (b) DTG modelling; (c) relative deviation

The confrontation between the experimental data and the models are shown in Fig 3.2.8 and Fig 3.2.9 respectively for MFC and NaLS. As it can be seen on these figures, the proposed models reproduce quite well the TG data. The relative deviation as a function of temperature is calculated according to Eq 2.5.7 and is presented in Fig 3.2.8c) and Fig 3.2.9c) whose maximum is less than 3% for both materials. The identified proportion, activation energy and pre-exponential factor of each pseudo-component are listed in Table 3.2.2 and Table 3.2.3. The last decomposition reaction for MFC may be related to decarboxylation and decarbonylation reactions of the char since CO_2 and CO are the only two volatiles produced in this range of temperature according to MS plots. With regard to the LS sample, the last reaction is more probable to be the thermal decomposition of an intermediate product during pyrolysis -Na_2CO_3[189] since there is a clear emission peak of CO_2 suggested by MS spectra in the same temperature range. However, even with the help of mass spectrometry, it is hard to identify the nature of other pseudo-components since they are normally the sum of several reactions.

Table 3.2.2 Arrhenius parameters for the 4 pseudo-components of MFC

Pseudo-components	1	2	3	4
Proportion	0.22	0.51	0.18	0.09
E_a (KJ/mol)	137	229	46	52
logA (log(s^{-1}))	23.7	40.3	1.5	0.1

Table 3.2.3 Arrhenius parameters for 6 pseudo-components of NaLS

Pseudo-components	1	2	3	4	5	6
Proportion	0.05	0.17	0.19	0.15	0.24	0.20
E_a (KJ/mol)	149	112	132	104	45	72
LogA (log(s^{-1}))	33	21	23	15	1.2	2

3.2.6.3 Comparison between isoconversional and model-fitting methods

The Ea values provided by isoconversional approach (Table 3.2.1) are generally higher than those obtained by the model-fitting approach for both materials regardless of conversion levels. Particularly, for conversion levels higher than 0.8, a clear divergence of *E* values could be perceived for both MFC and NaLS when comparing the two approaches. Furthermore, using even the smallest *E* value from table.1 to model the thermal degradation of pseudo-component 3 or 4 of MFC could not result a fitting as good as the original value does, despite the attempt to adjust the pre-exponential factor value to recompense the peak form change. These observations also hold for NaLS fitting procedure using values from Table 3.2.1.

Due to lack of kinetic data for NaLS pyrolysis in the literature, only MFC kinetic parameters are discussed by comparing them with those of cellulose from already published articles. As shown in Fig 3.2.10. *E* values suggested from literature as well as from this work suffer a great discrepancy depending on biomass types, experimental conditions, the choice of kinetic analysis approaches, *etc.*. The results obtained from isoconversional method are usually higher than those provided by the model-fitting approach, especially for high temperature

range reactions (e.g. pseudo-component 3), which is in agreement with our observation above. Furthermore, the activation energies given by model fitting in this work are quite close and consistent with those reported in literature, which confirms as well the accuracy of such approach being employed in kinetic analysis of MFC/NaLS.

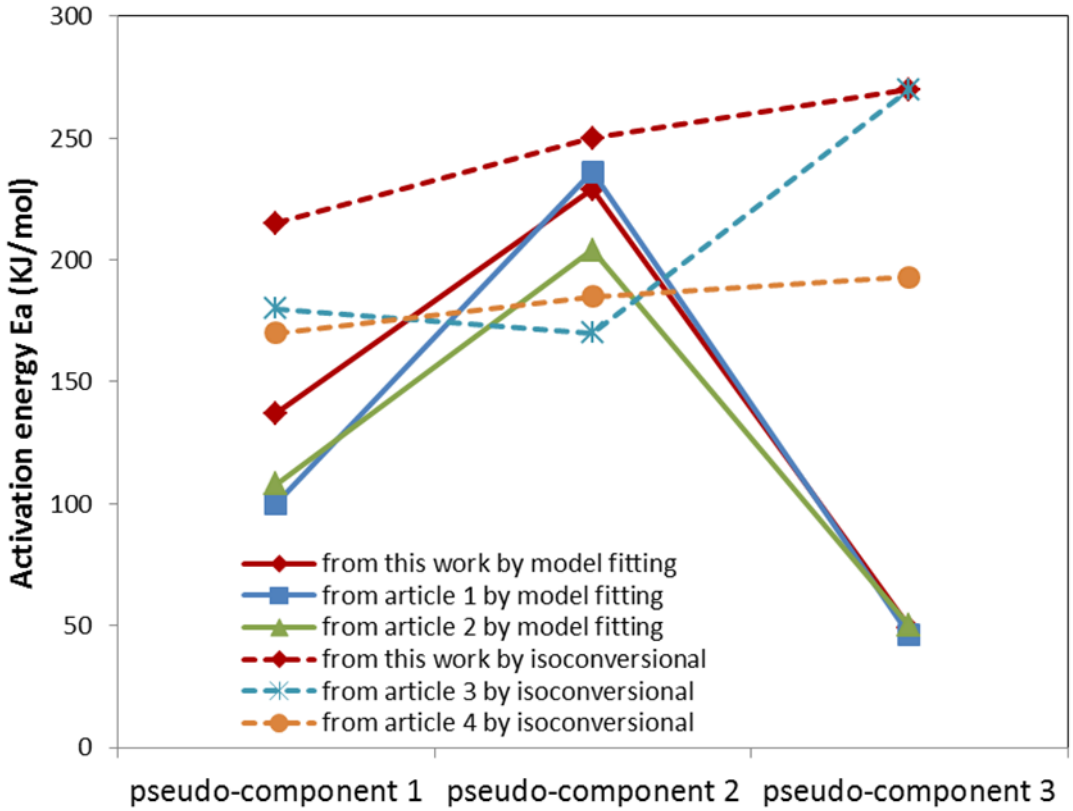

Fig 3.2.10 Comparison of E_a values provided in this work and those from references in terms of two methods: article 1[195]; article 2[196]; article 3[127];article 4[107]

3.2.6.4 Kinetic analysis of MFC/NaLS composites

Kinetics of such composites was analyzed based on single MFC and NaLS model. Consequently, each composite should contain ten pseudo-components whose proportion is determined by multiplying its original value in MFC (or NaLS) by the corresponding fraction of MFC (or NaLS) in the composite. From a kinetic point of view, presence of sodium ions catalyzes cellulose decomposition causing the activation energies of the latter to diminish in composites[102]. Therefore, lower activation energies should be expected for related pseudo-components of MFC in composites, whereas for NaLS they remain unchanged. Besides, pre-exponential factor *A* continues to be the same as in single MFC and NaLS kinetic model. Under these conditions, model-based method still results good fitting for two MFC/NaLS composites with relative deviation less than 3% throughout the whole temperature range, justifying the assumptions of i) linear superposition of MFC and NaLS in the composites and ii) drop of *E* due to catalytic effect. The utilized kinetic parameters are listed in Table 3.2.4.

Table 3.2.4 Kinetic triplets determined by model-fitting for 10 pseudo-components of Composite MFC77%/LS23% and MFC16%/LS84%

MFC77% MFC16%	1	2	3	4	5	6	7	8	9	10
Proportion (10^{-2})	16.94 3.52	39.27 8.16	13.86 2.88	6.93 1.44	1.15 4.20	3.91 14.28	4.37 15.96	3.45 12.60	5.52 20.16	4.60 16.80
E_a (KJ/mol)	132 126	219 197	45 43	52 50	149	112	132	104	45	72
LogA (log(s^{-1}))	23.7	40.3	1.5	0.1	33.0	21.0	23.0	15.0	1.2	2.0

3.2.7 Conclusions

In this work, MFC and LS were characterized in both separate and blended form in terms of morphology, chemical structure and thermal stability. Significant differences have been observed between these two main materials in all aspects owing to their different chemical constitution and structure. MFC degrades intensively within a narrow temperature range between 250°C and 350°C, while NaLS decomposes much more gently within 2 main temperature ranges, 150°C -500°C and 600°C -800°C. Moreover, kinetic analysis of separate MFC and NaLS has been conducted with both model-free and model-based approaches. The former method suggests Arrhenius parameters that are too high to be used to reproduce the experimental curve. However, model-fitting approach results in a quite good reproducibility of the experimental curve by providing MFC thermal degradation parameters that are quite consistent with the bibliographic ones. Kinetic analysis of the thermal degradation of NaLS is conducted for the first time providing a set of kinetic data that allows predicting the thermal behavior of such material. Furthermore, DTG curves, that represent the decomposition of MFC/NaLS composites mixed in various ratios, do not “linearly” combine the characteristic patterns of both materials due to the presence of sodium content. The catalytic effect of sodium is confirmed by a highly correlated relationship between T_p shift and sodium content as well as experimentally by the resulting thermal behavior of a MFC/NaCl blend. From a kinetic point of view, such a diminution of reaction temperatures could be interpreted as a decrease of activation energy of MFC pseudo-components in composites. By using lower E for MFC pseudo-components, successful fitting has been achieved for two MFC/NaLS composites by following a weighted superposition rule.

3.3 Use of MFC/LS blends as carbon precursors: characterization of MFC/LS carbons

3.3.1 Introduction

After rheological and thermal characterization, this part of work investigated the development of electrical conductivity in carbonized carbons from MFC/LS precursors as function of HTTs. MFC/LS carbons were characterized in terms of morphology (scanning electron microscopy), chemical functionalities (infrared spectroscopy), microstructure (Raman spectroscopy and X-ray diffraction) and physical properties (electrical conductivity and density evolution). A descriptive model, based on the progressive conversion of the biomass into conductive engineering carbons and composed of 3 distinguish phases, was thus established to illustrate the electrical conductivity development phenomenon.

3.3.2 Morphology of MFC/LS sheet before and after pyrolysis

Fig 3.3.1 shows the pyrolysis-induced morphological changes of MFC16%/LS84% sheets in the transversal section (a-c) and on the surface (d-f). The bulk structure of the composite is preserved even after a pyrolysis at 1000°C[197], indicating a good morphological stability of the MFC/LS system. This may be related to the slow heating rate adopted in the pyrolysis process which preserves more the initial structure of the biomass than in the case of the fast pyrolysis. Besides, the high percentage of LS which is quite heat-resistant[129] should also be accounted for such a good thermal stability. However, as shown in Fig 3.3.1b), a huge shrinkage in the thickness direction was observed after carbonization at 400°C. This shrinkage was drastic at the initial stages of pyrolysis and did not increase when increasing the HTT to 1000°C. According to the thermogravimetric analysis [157], the devolatilization peak of such composite occurs at around 275°C and by 400°C, 80% of the total mass loss was achieved, which explains the small morphological differences in chars carbonized at 400°C and at 1000°C.

The meso- and micro-porosity are invisible in the present scale of SEM, thus only macro-porosity will be discussed herein. Fissures and pores that appear on the sectional images in Fig 3.3.1a)-c) increases with the pyrolysis temperatures both in size and number. These fissures probably originate from the volatile matter release and internal overpressure during the pyrolysis process. It has to be noted also that some fissures were visible during ambient air drying of the sample (as in Fig 3.3.1a)). However, the macropores density on the surface of the chars (Fig 3.3.1e)&f) is not visibly much higher than non-carbonized one

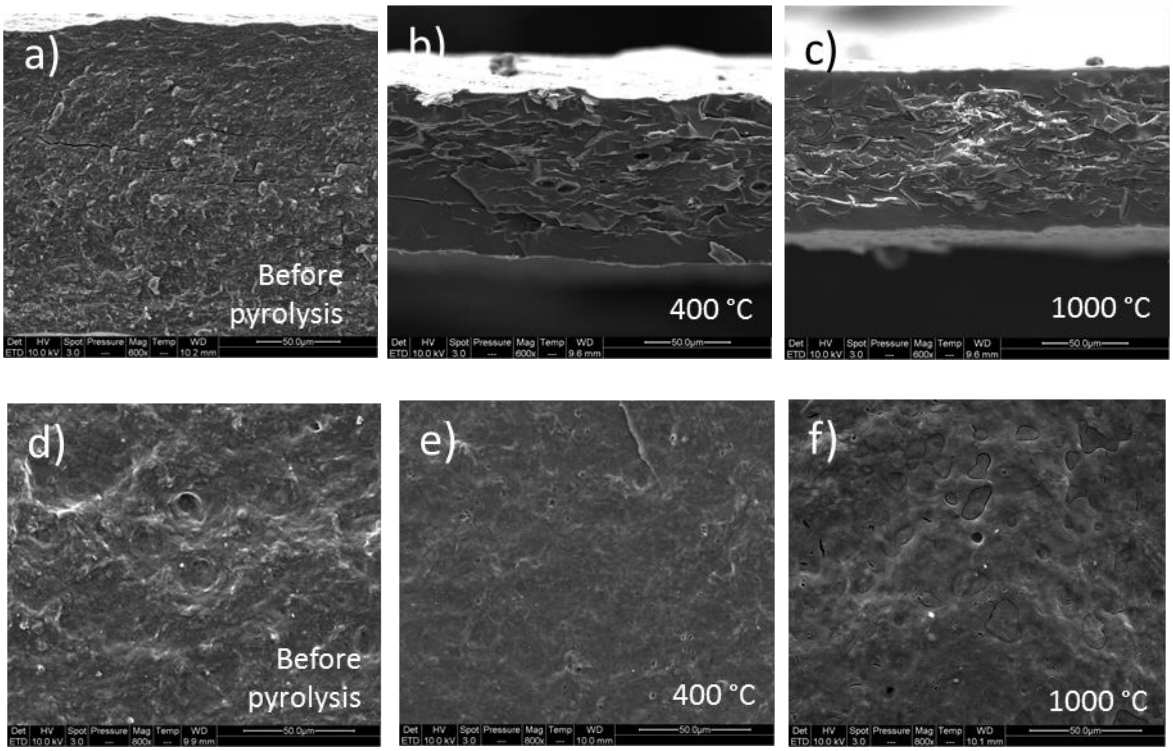

Fig 3.3.1 SEM images of a)-c) the transversal section and d)-f) surface of MFC/LS sheet before and after carbonization at 400 and 1000°C

3.3.3 Chemical characterization by FTIR

The FTIR spectra of MFC/LS chars prepared at 400-1200°C are displayed in Fig 3.3.2. It can be observed that FTIR signals progressively lose their characteristics peaks with increasing HTTs from 400°C. One of the most important reductions occurs in the wavenumber range of 3600-3200cm^{-1}, attributed to the hydrogen bonded O-H stretching vibration[198,199], which corroborates authors' earlier findings by TG/MS that dehydration is the most significant reaction during pyrolysis[157]. Also, it can be observed that the two small peaks at approximately 1510 and 1460 cm^{-1} which are related to the Guaiacyl and Syringyl units in the LS[200], are much less pronounced after pyrolysis at 400°C, indicating the thermal degradation of the former LS material. These two peaks continue to vanish upon heating to higher temperatures. Moreover, aromatic condensation becomes more and more visible for chars carbonized beyond 600°C. This aromatic condensation is accompanied with a decline of the aliphatic C-H groups (3000-2800cm^{-1}), the net decrease of the alkyl sulfonate functionalities (around 1150 cm^{-1}) and C-O functionality (around 1030 cm^{-1}).Besides, the broad band with some sub-bands between 1600-1000cm^{-1} (including the in-plane C-H bending vibrations that interact with various aromatic ring C-C vibrations[198,201]) decreases substantially with the HTT, indicating the progressive aromatization of the formed carbonaceous material. Further evidence of the aromatic ring condensation, as mentioned by several authors[198,202] but not quite obvious in the current results, is the appearance of three bands between 900-700cm^{-1}, assigned to the out-of-plane C-H bending vibrations. For chars obtained from high temperature pyrolysis, *ca.* 1000°C and 1200°C, all characteristic signals are largely reduced, indicating the loss of mostly functional groups as well as the start of graphitization since

graphite has no characteristic infrared bands in the investigated wavenumber range (spectrum of graphite could be found in articles[201,203]) and the FTIR is not sensitive to long-range ordering during graphitization[204].

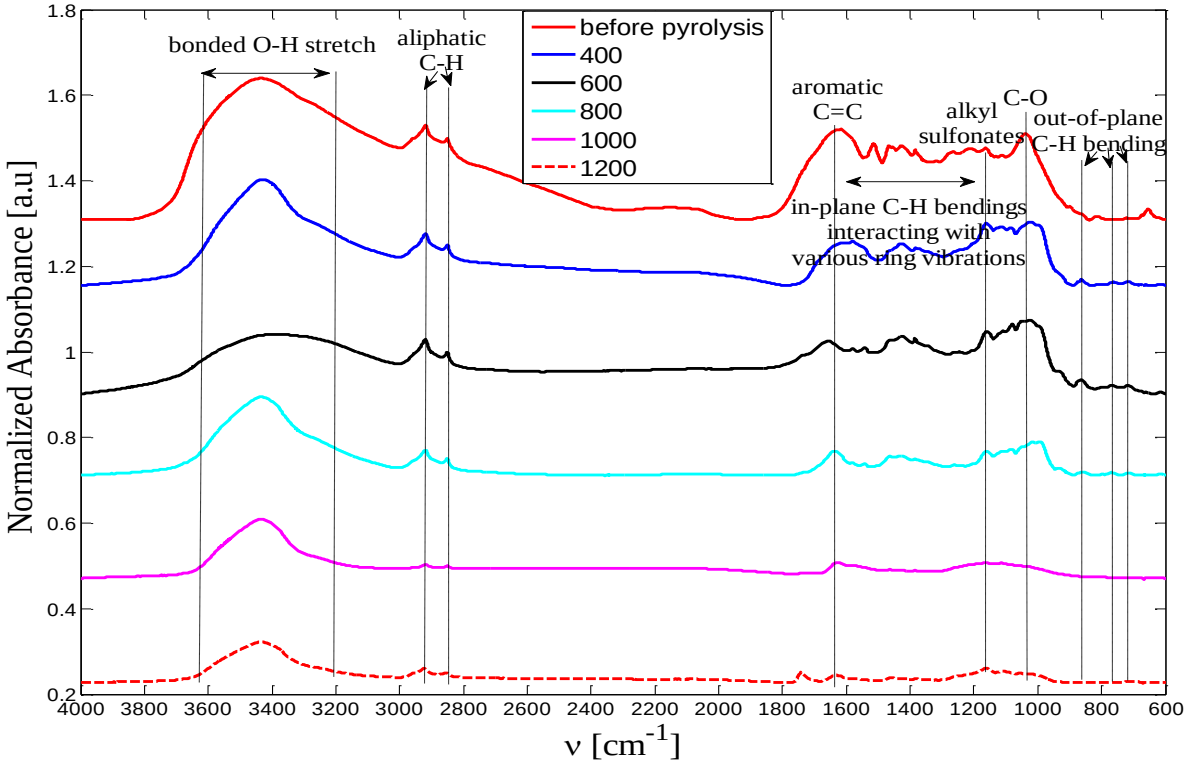

Fig 3.3.2 FTIR spectra of MFC/LS composites before and after pyrolysis to different HTTs

Generally speaking, pyrolysis up to 400-1200°C generates a continuous reduction of functional groups in chars, mainly due to the dehydration[199] and aromatic condensation[150,199,201]. Over 800°C, only some oxygen containing functional groups resist from the pyrolysis and most of the carbon content appears to be incorporated into condensed aromatic structures, making its FTIR spectrum close to that of polycrystalline graphite

3.3.4 Density evolution

Fig 3.3.3 exhibits both bulk and skeletal (true) densities of MFC/LS sheet and those of its derived carbons. Skeletal densities rise from 1.45 to 2.05 for HTT ranged from 400 to 800°C, which is in good agreement with the literature[205–208]. Such increase in true densities is thus considered as reflecting the continuous synthesis of highly organized carbon structures (turbostratic structures) that are more compact and denser than disordered carbon[205,206]. During pyrolysis, non-conjugated molecules either decompose as volatiles or convert into conjugated ones and the chars undergo aromatic condensation. Due to the existence of defects (oxygen components that are heat-resistant) and the randomly oriented graphite crystals (turbostratic nature), the maximum skeletal density of biochars is always below that of graphite (2.25 g/cm^3)[205,208] and within the range of 2-2.1 g/cm^3.[206,208] However, a slight drop of skeletal density to 1.79 g/cm^3 is observed for the sample carbonized at 1000°C which is later followed by a recover up to 1.94 g/cm^3 (1200°C). To authors' best knowledge, such

irregular changes of skeletal density were rarely reported elsewhere and should be associated with the departure of heteroatoms, probably oxygen, while the carbonaceous char is suffering from structural rearrangement.

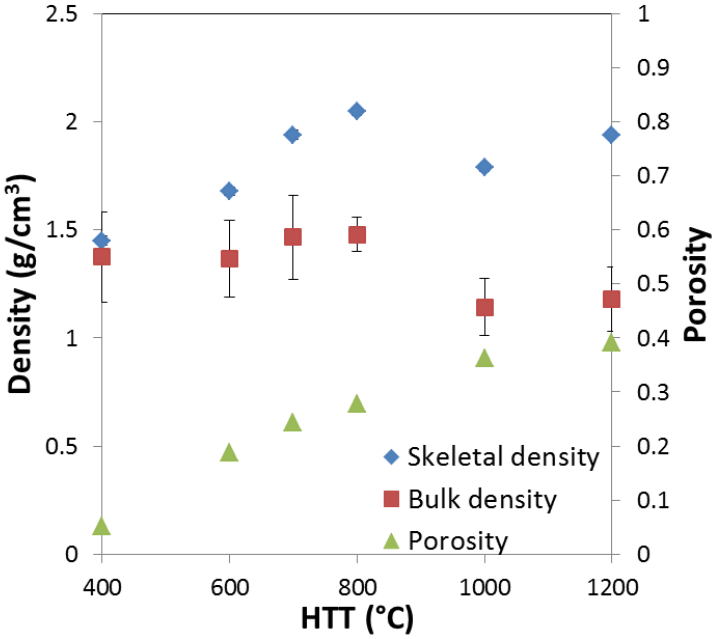

Fig 3.3.3 Bulk and skeletal densities of MFC/LS precursor (23°C) and carbons as well as the calculated porosity

Bulk density of biocarbons is the result of the competition between the HTT-induced weight loss and volumetric shrinkage. It generally follows the evolution profile of the skeletal density although with a lower value because of the existence of the porosity. Bulk densities slightly increase from 1.30 to 1.48 g/cm^3 with elevated HTTs until 800°C (Fig 3.3.3), quite similar to those of biochars as reported elsewhere[156,205,207]. This increase of bulk density is the result of the weight loss that is less important than the volumetric shrinkage throughout this temperature range[207]. Above 800°C, bulk density falls immediately into 1.14-1.18 g/cm^3, as a result of the continuous loss of weight whereas the dimensional shrinkage is quite small[207].

The calculated porosities also increases with HTT (Fig 3.3.3), which is in agreement with the previous SEM observation (Fig 3.3.1) and the literature[206,207]. Compared to wood and grass precursor, chars derived from MFC/LS precursor have significantly lower porosities, ranged from 0.05 to 0.4, corresponding to HTT at 400°C and 1200°C (over 0.6 for wood and grass carbons). This difference was associated to the presence of a continuous LS matrix in the pristine MFC/LS composite.

3.3.5 Electrical conductivity evolution

The evolution of biochars' bulk conductivity as a function of HTT is presented in Fig 3.3.4. According to the measurement, chars of MFC/LS sheets begin to achieve a DC measureable electrical conductivity after carbonization at around 600°C. An extremely important increase of more than 3 orders of magnitude occurs between 600 and 700°C, from 4.86×10^{-4} to 1.29

S/cm, as reported by many other studies concerning biomass pyrolysis[10,156,168,201]. Between 700 and 1000°C, the DC conductivities of MFC/LS chars rise linearly with the heating temperatures, indicating the strongly HTT-dependent conductivity of as-produced carbons. After 1000°C, the temperature effect on electrical conductivity levels off.

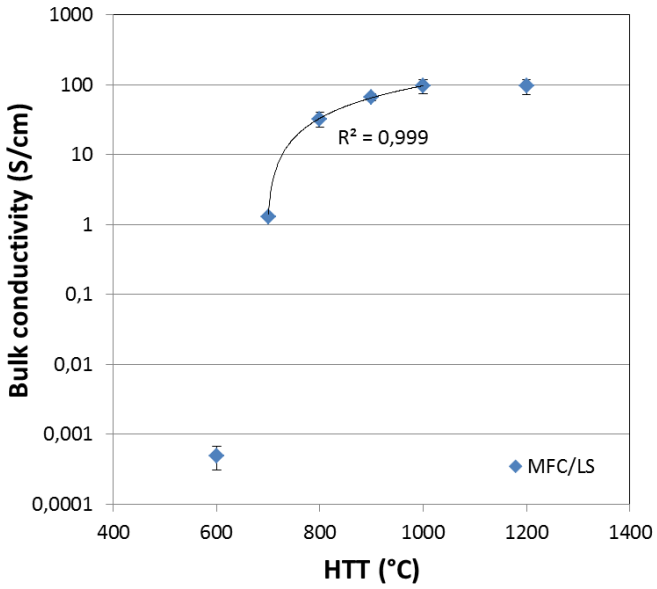

Fig 3.3.4 Evolution of electrical conductivity of chars as a function of HTT

3.3.6 Microstructural evolution

3.3.6.1 Raman analysis

Since Raman spectroscopy is particularly sensitive to sp2 carbon structures and their features measured on the scale of nanometers[167,209], it is widely used to evaluate the development of graphite-like microstructures in disordered or turbostratic carbon materials[210–213]. Normalized Raman spectra of as-carbonized chars are demonstrated in Fig 3.3.5 and the intensities of the most characteristic bands are summarized in Fig 3.3.6. According to Fig 3.3.6, the D band (located approximately at 1300 cm^{-1}) is visibly pronounced, from 0.2064 to 0.4163 when the HTT was increased from 400 to 1200°C. The G band (1600 cm^{-1}) is only slightly enhanced with increasing HTTs. On the contrary, the V band (at around 1500 cm^{-1}) together with S band (1200 cm^{-1}) and Gr band (1800 cm^{-1}) are continuously reduced from over 0.7 to below 0.5. Similar evolution of Raman bands was given in the literature[163,165,214,215]. The most important modifications of bands occur between 400 and 600°C for which the band V, S and Gr are importantly reduced whereas the D and G band are visibly enhanced (more visibly in Fig 3.3.5). Such band changes are supposed to be correlated with the transformation from insulators to conductors for the chars carbonized at 400 and 600°C.

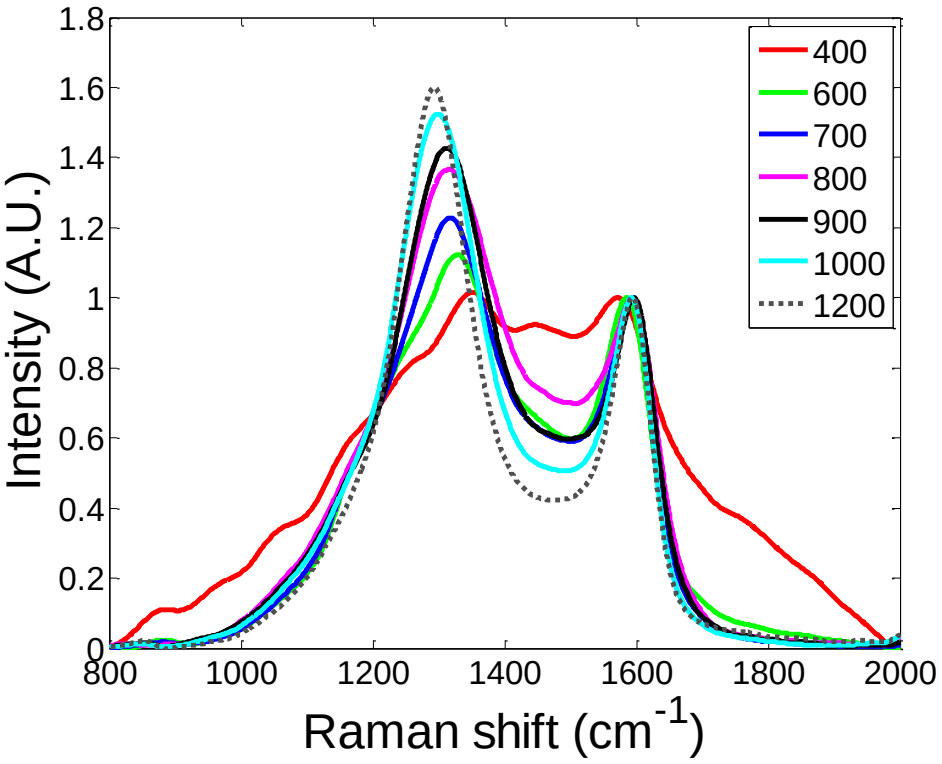

Fig 3.3.5 Raman spectra of MFC/LS chars prepared at 400 to 1000°C, normalized to G band positions

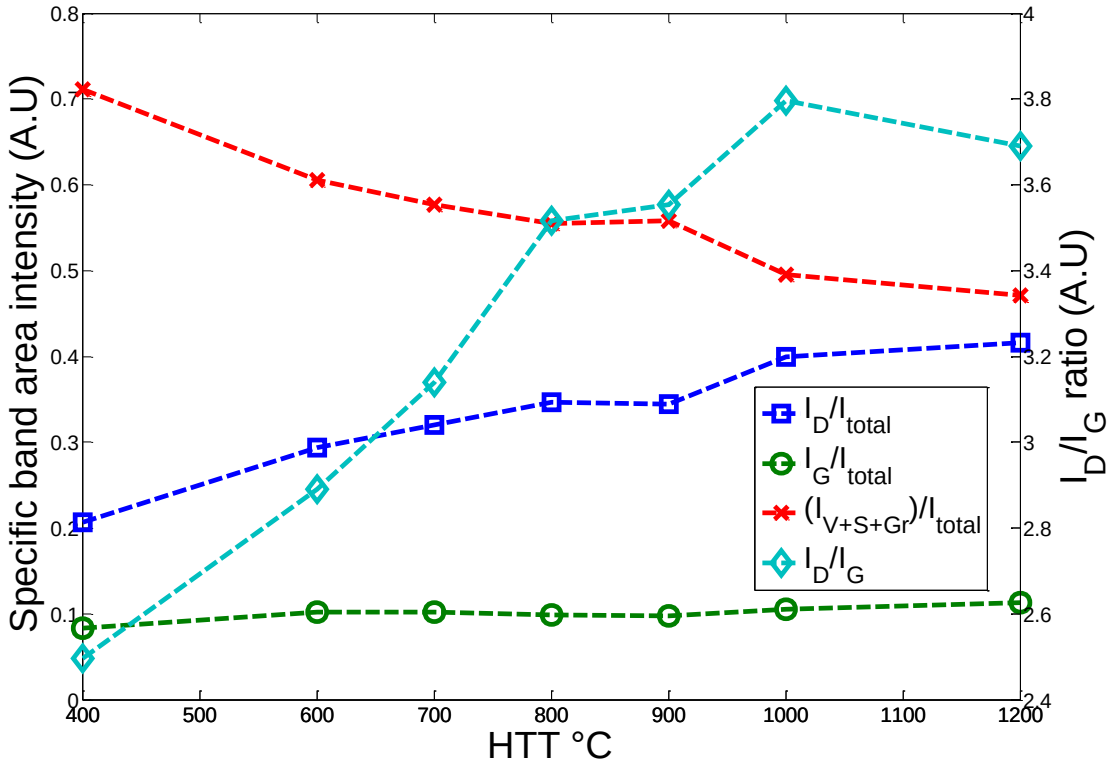

Fig 3.3.6 Calculated area intensities of band D, G, (S+V+Gr) as well as D/G band ratio as function of HTTs

As pointed out in the literature[10,150,211], G band arises from the sp^2 bonded carbon structures and is intensively present in highly ordered carbon structures like graphite whereas D band is attributed to the disorder around sp^2 carbon, such as defects, distortions and the edges of graphite crystals. Therefore, the band ratio of D to G is often used to characterize the structure ordering in carbon materials[168]. An increase of the band area of D over G could be obtained according to the deconvolution results, as shown in Fig 3.3.6. Such an increase reveals a more important rise of defect or edge-bonded graphite-like structures compared to that of graphitization, indicating an increase in the concentrations and/or the size of aromatic clusters[164,166]. More specifically, due to the oxygen-rich precursor as was used in this work, defects, mainly composed of oxygen, are inevitable since oxygen remains even after high temperature pyrolysis (according to FTIR results in Fig 3.3.2). Although D band was named after defects, its appearance does require the presence of ordered carbon structures (≥6 benzene rings) in close proximity[164,166,167].Furthermore, V, S and Gr bands, which are related to the presence of amorphous carbon structures[167] decrease at elevated HTTs. This would imply a continuous removal of amorphous carbon structures during pyrolysis through devolatilization and/or conversion of the amorphous structures into more ordered graphite-like ones[167,216].

It is worth noticing that the D/G ratio is observed to decrease in the bio-carbon obtained after pyrolysis at 1200°C (Fig 3.3.6). The existence of a maximum of the D/G ratio in the temperature range from 580°C to 1500°C is commonly observed in the related studies[10,164,212,217]. With the enlargement of the aromatic ring system that is further enhanced by temperatures over 1000°C, the decrease of the “defects” (band D) with regards to an important growth of regular graphene stacks (band G) is supposed to lead to a decrease of D/G band ratio[164]. The reduction of defects (oxygen-containing) could also be confirmed from FTIR results in Fig 3.3.2 for the sample of 1200°C.

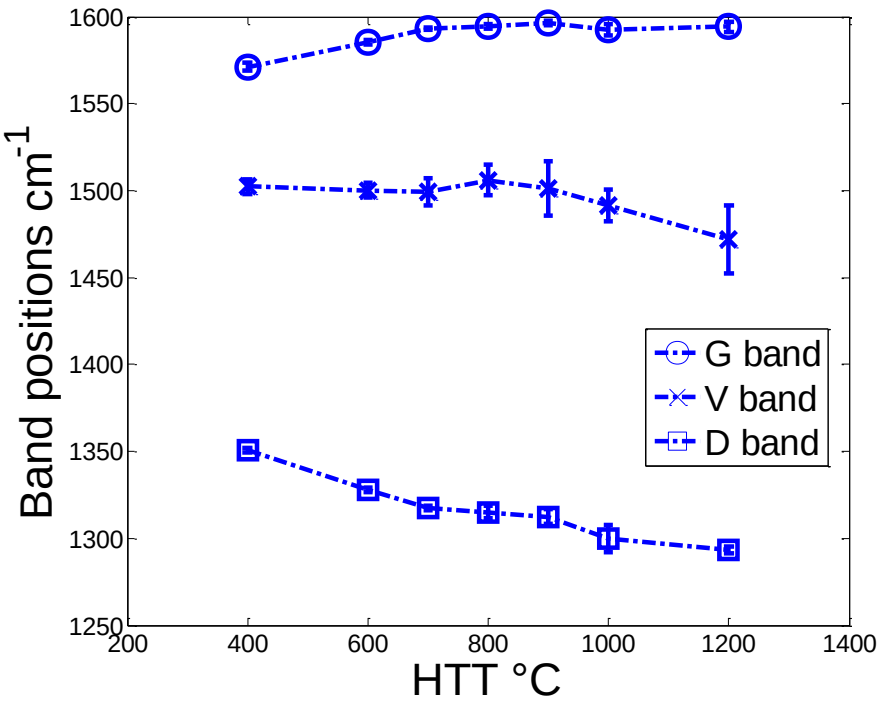

Fig 3.3.7 Band position variations of chars carbonized at different HTTs

In addition to band ratios, band positions could also provide some clues about chars' microstructural modifications. In Fig 3.3.7, G band is found to shift to higher frequencies (blue shift) with elevated HTTs and in contrast to that, D band tends to move towards lower positions (red shift) while V band do not show a noticeable position change. It is believed that G band position is strain-related[218–220]. As aromatic clusters grow larger and more graphite-like during heat treatment, they begin to collide, impinge and/or merge with neighboring clusters within a confined volume by putting themselves under increasing compression[167]. Therefore, such blue shift might be another sign for the growth of ordered carbon clusters. On one hand, D band position red shifting with increasing HTTs could be assumed to be due to the ever increasing tensile strain that the near-edge structures suffer from, in contrast to the blue shift of G band[220]. On the other hand, D band position allows providing information about the most common types of near edge structures around the ordered carbons[167]. For chars prepared at 400°C, their D band is located at around 1350 cm^{-1}, corresponding to that of laser-reduced graphene oxide whose predominant edge structures are amorphous carbon bonded (sp^3 bonded). It also collaborates with the fact that 400°C carbonized char has the most important amorphous carbon content. As HTT increases to 900°C, D band of chars moves gradually towards the D band position of synthetic graphite (around 1316 cm^{-1})[167], indicating that the edges become similar to those in graphite. Then at 1000°C, the curvature of the edges/defects is pronounced and becomes more fullerene-like, which leads its D band position to approach 1300 cm^{-1}.[221]

3.3.6.2 XRD analysis

XRD has been widely used to help estimating the dimensions of graphite –like crystallites in turbostratic carbon materials[8,222–225]. The diffractograms of as-carbonized chars are displayed

in Fig 3.3.8. In the current measuring range, all diffractograms exhibit a broad (002) reflection at $2\theta \approx 25°$ and a dimensional lattice band (100) at 44°, indicating the existence of graphene-layer stacks in the chars[150,223,225]. The interlayer spacing d_{002}, stack thickness L_c and the lateral size of stacks L_a were as-calculated and shown in Table 3.3.1.

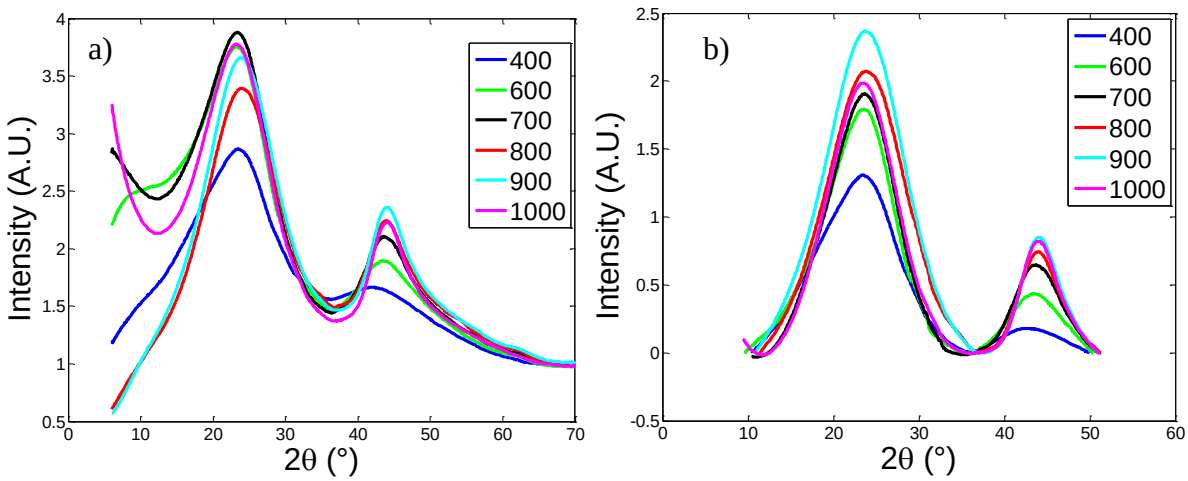

Fig 3.3.8 Normalized XRD diffractograms of chars a) before and b) after linear-subtraction

Table 3.3.1 Crystal parameters in MFC/LS carbons

HTT (°C)	400	600	700	800	900	1000
d_{002} (nm)	0.38	0.39	0.38	0.37	0.37	0.38
L_c (nm)	0.74	0.86	0.87	0.75	0.75	0.86
L_a (nm)	2.14	2.49	2.78	3.14	3.34	3.40
N	2.95	3.23	3.29	3.02	3.02	3.24

A general rise of lateral size of crystallites, from 2.135 nm to 3.395 nm can be observed when the carbonization temperature increases from 400 to 1000°C. Quite similar values were reported in pitch-based carbon fibers[212] and pine wood chars[159]. The interlayer spacing values of MFC/LS chars fall in the typical range of 0.37-0.41 nm for cellulose-based chars carbonized between 400 and 1000°C[158,199,201]. The thickness of the stacks of graphene layers varies between 0.74-0.89 nm, signifying that each stack consists mainly of 3 graphene sheets (the number of layers was calculated according to Eq 2.6.4). The resulting crystal parameters are displayed in Table 3.3.1, which are in good agreement with the data provided in the literature[150,201].

3.3.7 Discussion

3.3.7.1 Development of electrical conductivity during pyrolysis: impact of porosity

As highlighted by the SEM images (Fig 3.3.1), MFC/LS carbons present stable bulk structures consisting of a hard carbon matrix and crack-like pores. The conductivity of the bulk structure is thus supposed to be reduced by the presence of porosity. In order to eliminate the porosity effect, skeletal conductivity that represents only the conductivity of the hard carbon was calculated according to Eq 3.3.1. Such expression is based on an open carbon foam model[226], where σ and ρ represent the conductivity and the density of the material, respectively, and the subscript s denotes skeletal properties (hard carbon) whereas the terms without it indicate bulk foam properties.

Eq 3.3.1 $$\frac{\sigma}{\sigma_s} = \frac{1}{3}\left(\frac{\rho}{\rho_s}\right) + \frac{2}{3}\left(\frac{\rho}{\rho_s}\right)^{1.5}$$

As expected in Fig 3.3.9, the skeletal conductivities display higher values than bulk ones but roughly follow the profile of the latter with regards to HTTs. After carbonization at 1200°C, MFC/LS biochar could achieve an electrical conductivity as high as 186 S/cm, which is about one order of magnitude lower than that of polycrystalline graphite (1250 S/cm)[18,156] and in line with the presence of defect or edge-bonded graphite-like structures after carbonization at 1200°C.

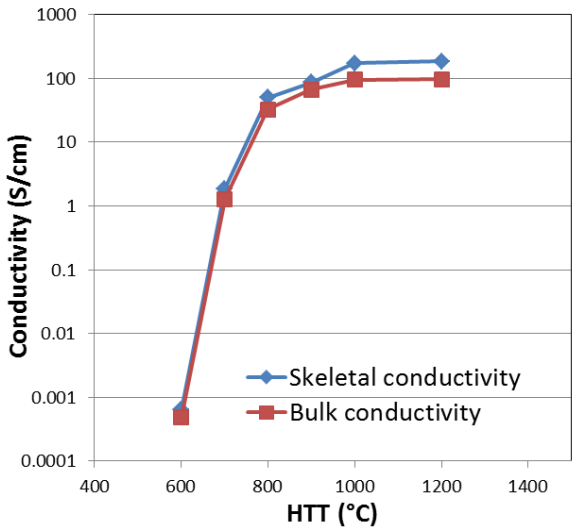

Fig 3.3.9 Skeletal conductivity as function of HTTs

3.3.7.2 Development of electrical conductivity during pyrolysis: impact of microstructures and HTTs

Leaving aside the porosity effect, the conductivity of MFC/LS hard carbon is still strongly HTT-dependent (Fig 3.3.9) and must be correlated to the mutual evolution of the conductive and insulating phases in the chars[10,150]. McDonald-Wharry *et al.*[150] proposed a phenomenological model for illustrating the microstructural changes during pyrolysis for non-graphitizing precursors. Based on this model as well as the present results, a model describing

the electrical conductivity development in MFC/LS carbons was derived, as show in Fig 3.3.10.

By combining the results concerning microstructure evolution with that of electrical property, the conductivity development of MFC/LS carbons is supposed to pass through several different regimes as function of HTTs:

i. 400°C ≤ HTTs≤ 600°C: chars at this period already possess regular graphene stacks in small size (2,135 nm), as evidenced by XRD results. However, they are completely isolated by defected graphene structures (detected by Raman band D) and amorphous structures (Raman band V, S and Gr) with the latter far more importantly present in the chars. Thereby, electron hopping and tunneling is prevented or largely reduced. Consequantly, DC conductivity of chars is undetectable or quite low (Fig 3.3.10a)).

ii. 600°C <HTTs< 700°C: with the amorphous phase continuously reducing or incorporating into structured phases, the latter, regardless of regular graphene stacks or defected ones, is growing and approaching to each other. Upon a percolation threshold, they get in mutual contact thus largely favoring electrons' movement. In hence, the DC conductivity is sharply improved. Since the defected graphene phase is far more important than the regular one in MFC/LS carbons, which is evidenced by Raman D/G ratio that is always more than 1, it is supposed that the electrical pathways are constructed more probably by contacts between defected graphene clusters (Fig 3.3.10b)).

iii. 700°C ≤HTTs≤ 1000°C: during this period, both regular and defected graphene structures continue to grow in size and in number, intensifying the mutual contacts between conductive clusters. As a result, electrical conductivity is strengthened (Fig 3.3.10c)).

iv. HTTs>1000°C: once the current pathway has been established, further graphitization or reduction of defects will not lead to important increase in contacts between conductive phases, thus the HTT-induced development of electrical conductivity slowed down (Fig 3.3.10d)).

Fig 3.3.11 displays the relationship between the skeletal conductivity of MFC/LS carbons and the Raman ratio of band D and G over the total band area as well as graphene crystal size L_a. It could be found that the conductivity is quite positively correlated to the crystal size and the D+G band ratio, confirming that the conductivity improves with strong relationship to the growth of both regular graphene stacks' and defected graphene structures. Furthermore, since MFC/LS carbons have defected-graphene-dominated structure (ID/IG is always more than 1), the growth of the defected graphene phase is more significant, compared to regular one, in terms of ensuring the conductivity of the resulting hard carbon.

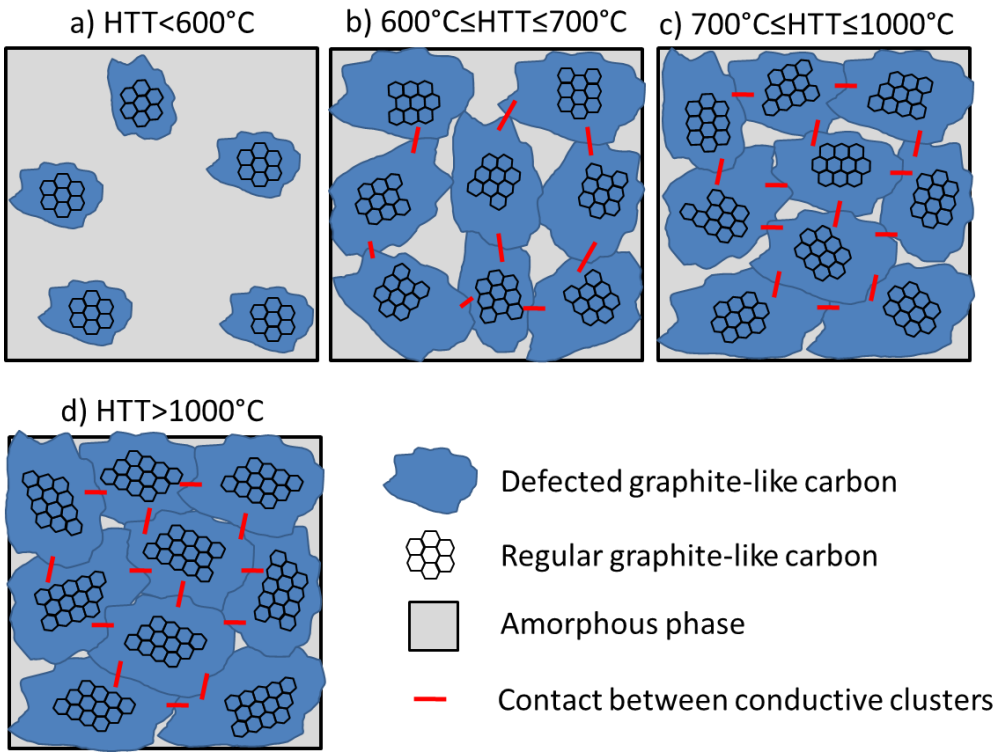

Fig 3.3.10 Illustrative schema for describing the conductivity development in MFC/LS carbons

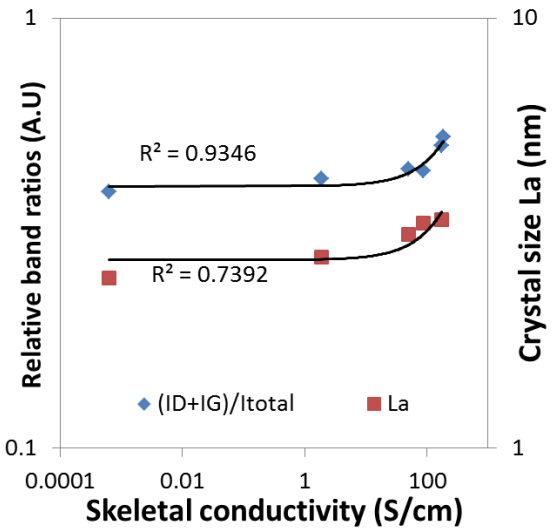

Fig 3.3.11 Correlation between skeletal conductivities and band ratio I_{D+G}/I_{total} as well as crystal size L_a

3.3.7.3 Comparison of biocarbons from various precursors in terms of electrical property

After one step casting and carbonization at 1000°C, MFC/LS sheets could achieve a surprisingly high electrical conductivity of 95 S/cm with a relatively low density 1.14 g/cm^3, even compared to polycrystalline graphite (1250 S/cm and 1.6 g/cm^3)[18]. A comparison with other biocarbons in terms of physical properties was made and presented in Table 3.3.2.

Although different compositions and physical forms that make it hard to compare directly the specific electrical conductivity between the listed biocarbons, authors can still remark the mutual promotion between MFC and LS in terms of carbon quality: i) compared to MCC carbon, MFC/LS contains also micro-scaled cellulose fibers but could achieve nearly double conductivity at the same carbonization temperature mainly because of its LS content that is heat-resistant and contributes significantly the carbon yield so as the electrical property; ii) without MFC that constructed a micro-scaled web that tightly cross-linked LS molecules, LS solely could not form self-standing sheet that is later thermally stable.

Table 3.3.2 Comparison of biocarbons from various precursors

Ref	Bulk conductivity (S/cm)	Bulk density (g/cm^3)	Physical form	Precursor
This work	95 (1000°C)	1.14	Self-standing sheet	MFC/LS blend
Rhim *et al.*[10]	50 (1000°C)	1.17	Bulk pellet	Microcrystalline cellulose (MCC)
Kercher *et al.*[156]	20 (1000°C)	0.595	Monolith	Fiberboard
Deraman *et al.*[180]	4.9 (1000°C)	1.05	Bulk pellet	Lignin/precarbonized carbon
Lu *et al.*[181a]	0.9-20	0.065-0.6	Monolithic aerogel	Polycondensed resorcinol-formaldehyde
Sanchez-Gonzalez *et al.*[182a]	0.44-2.15	0.25-0.7	Compressed carbon black	Carbon black

[a] Carbons from precursors other than biomass, given for comparison

3.3.8 Conclusions

This part of work characterized the biocarbons elaborated by slow pyrolysis of MFC/LS precursors. A wide range of heat treatment temperatures (HTTs: 400-1200°C) was explored for biocarbons' synthesis in order to better understand the improvement of their morphological, physicochemical and microstructural properties, and the most importantly, the electrical properties. MFC/LS carbons have been proved to be heat-resistant and morphologically stable to slow pyrolysis. FTIR results provided evidences concerning the loss of the majority of functional groups during heat treatment in MFC/LS carbons and only a few oxygen-containing structures were retained from high-temperature pyrolysis. Microstructural

characterization by Raman revealed that the resulting carbons are composed of i) defect-free (regular) graphene stacks (3 layers of graphene, according to XRD); ii) defected (mainly oxygen) graphene structures and iii) amorphous phases. XRD results allow to perceiving directly the growth of regular graphene stacks with elevated HTTs whereas Raman ratios help understanding the relative changes of all three phases. As a result of the growing of conductive phases (regular and defected) in addition to the reduction of the insulating ones (amorphous), a general increase of electrical conductivity was observed in MFC/LS hard carbons as function of HTTs although the mechanisms for the conductivity development are not the same in different HTT ranges. Based on that, a model describing the electrical conductivity development in MFC/LS hard carbons was proposed. By accounting the porosity effect, the bulk conductivities of MFC/LS carbons are also strongly HTT-enhanced which are resulted from the competition between the conductivity strengthening in hard carbons and the porosity development.

After carbonization at 1000°C, biocarbons from MFC/LS precursors are still self-standing sheets and could achieve quite interesting electrical conductivity (95 S/cm) compared to their relatively low density of 1.14 g/cm^3. The resulting physical properties are really outstanding in comparison with previously reported biocarbons.

3.4 Optimization of the formulation of carbon precursors for 3D printing and carbon quality

3.4.1 Introduction

The work in section 3.1 reveals that add of LS into MFC hydrogels leads to either a disruption of the hydrogels' stability after 3D printing due to lack of viscosity (with 10%-30% LS), or a loss of shape definition because of the long restauration time (with 50% LS). Nevertheless, LS is an essential component to the composite since it largely contributes to the carbon yield after pyrolysis which is important to ensure the conductivity of as-elaborated bio-carbons. One solution to improving the hydrogels' printability while keeping using large quantity of LS in the formulation is to add appropriate additives. In the frame of this work that is to use bio-sourced materials, cellulose powder was chosen.

In section 3.4, the impact of cellulose powder added into the formulation of MFC/LS blends was investigated in terms of rheology and the resulting 3D printing, using the same methodology as described in section 3.1. Furthermore, the pyrolysis procedure of MFC/LS/CP composite was monitored using TGA, referring to section 3.2. Carbons elaborated from MFC/LS/CP precursor were also compared to those from MFC/LS precursors according to the microstructure, density, conductivity (section 3.3). In addition to that, MFC/LS/CP carbons were characterized especially in mechanical strength.

3.4.2 Rheological properties of MFC/LS/CP hydrogel

The improvement of rheological properties by the addition of CP is shown in Fig 3.4.1. The viscosity still keeps the shear-thinning profile but is strengthened by 2-3 magnitudes due to 22% of CP (w/w+water) added into the pristine MFC/LS hydrogel. More importantly, the time for network restauration is largely shortened, from 27s to 4s (since MFC/LS/CP is quite similar to pure MFC behavior)[15], with the presence of CP. The printing results (Fig 3.4.1a)) confirmed the usability of as-formulated hydrogel.

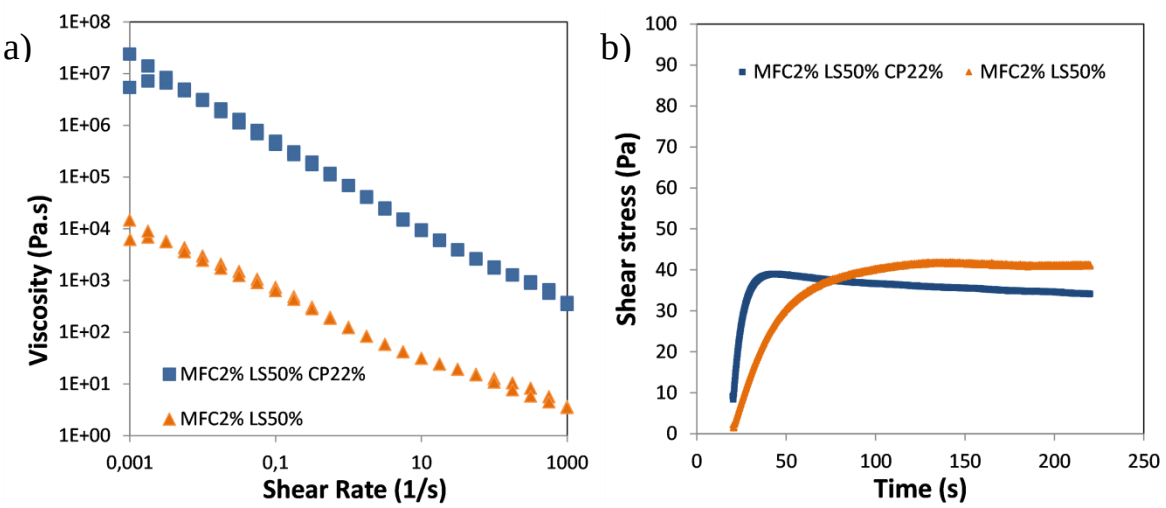

Fig 3.4.1 Viscosity a) and b) thixotropic property of the MFC/LS/CP hydrogel, compared to the corresponding binary one (MFC/LS)

3.4.3 Macro- and micro-morphology of MFC/LS/CP precursor and the resulting carbons

The photographs of 3D-printed MFC/LS/CP precursor composites are displayed in Fig 3.4.2a). After air-drying at ambient temperature, the dry objects still maintain their original shape and definition without visible defects due to the evaporation of water. Carbons derived from their corresponding precursor are surprisingly well-shaped and also without major surface and sectional irregularities although a rather important shrinkage occurred during the pyrolysis (Fig 3.4.2b)). As a result, the excellent morphological stability of the MFC/LS/CP carbon precursor could be concluded, that is the cornerstone of further characterizations of as-elaborated carbons.

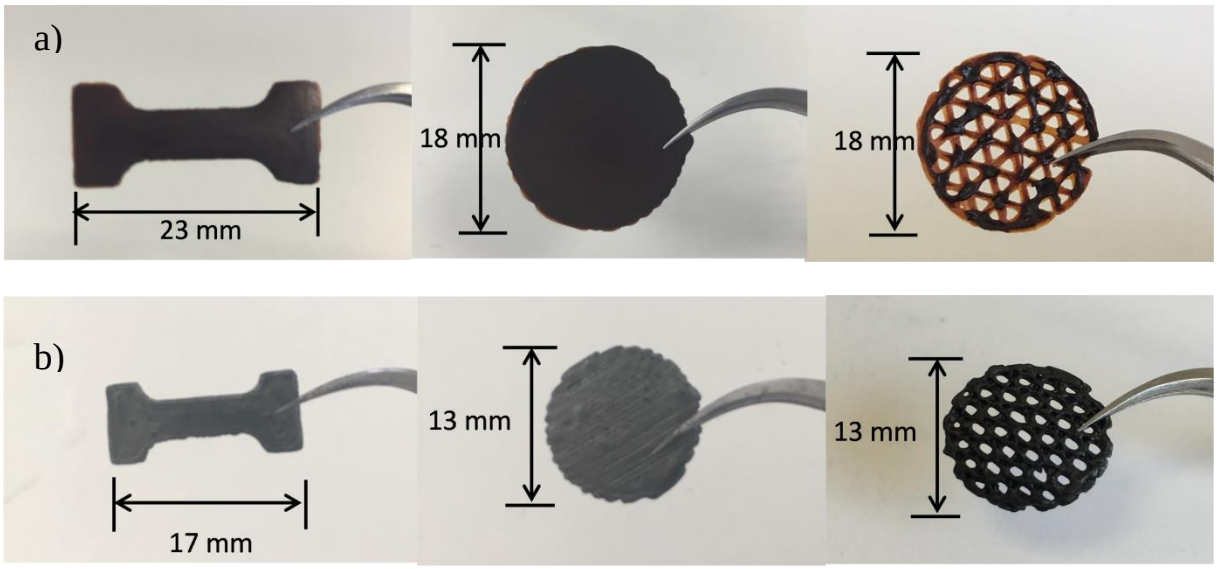

Fig 3.4.2 Photographs of: a) 3D-printed objects from MFC/LS/CP hydrogel after air-drying; b) after pyrolysis at 1000°C

The micro-scaled morphology of the samples is presented in Fig 3.4.3 using a SEM. The used cellulose powder (CP) particles (Fig 3.4.3a)) have an average length of 50µm and look like pieces cut from the much longer cotton linters. Its presence in the MFC/LS/CP composite can be clearly seen from the surface of the latter (Fig 3.4.3.b)). Such composite has a typically "almond chocolate" construction in which CP is more like the tiny pieces of almond wrapped by the "chocolate" surrounding that is made of MFC/LS. Since MFC was included in the composite in very small quantity and also because of its tiny dimension, it is less visualized than LS in the "chocolate-like" MFC/LS background. Furthermore, pyrolysis leads to limited changes on the sample surface except largely broadening and intensifying the fissures among which some seem already existed after drying (Fig 3.4.3b) & c)). Besides, it "smooths" the surface due to the low residue of CP at 1000°C (confirmed by Fig 3.4.4c)). However, images of samples' section (Fig 3.4.3d) & e)) reveal an important appearance of macro-pores that is very likely to be the result of CP decomposition during pyrolysis by accounting the dimensions of pores (multi-diameters, up to 50µm) as well as the fact that CP was wrapped randomly in three-dimension by the MFC/LS surrounding. The significant improvement of

the porosity by the addition of CP in the formulation (compared to MFC/LS composite) will lead to a more promising use of the studied bio-carbons in energy storage devices. In addition to that, it is worth noticing that although the sample was constructed with printed filaments(diameter=500µm), no single filament was identified from the section image in micro-scale (Fig 3.4.3d)), signifying that all filament were molten together after deposition and the samples is rather homogeneous in terms of the distribution of the matter.

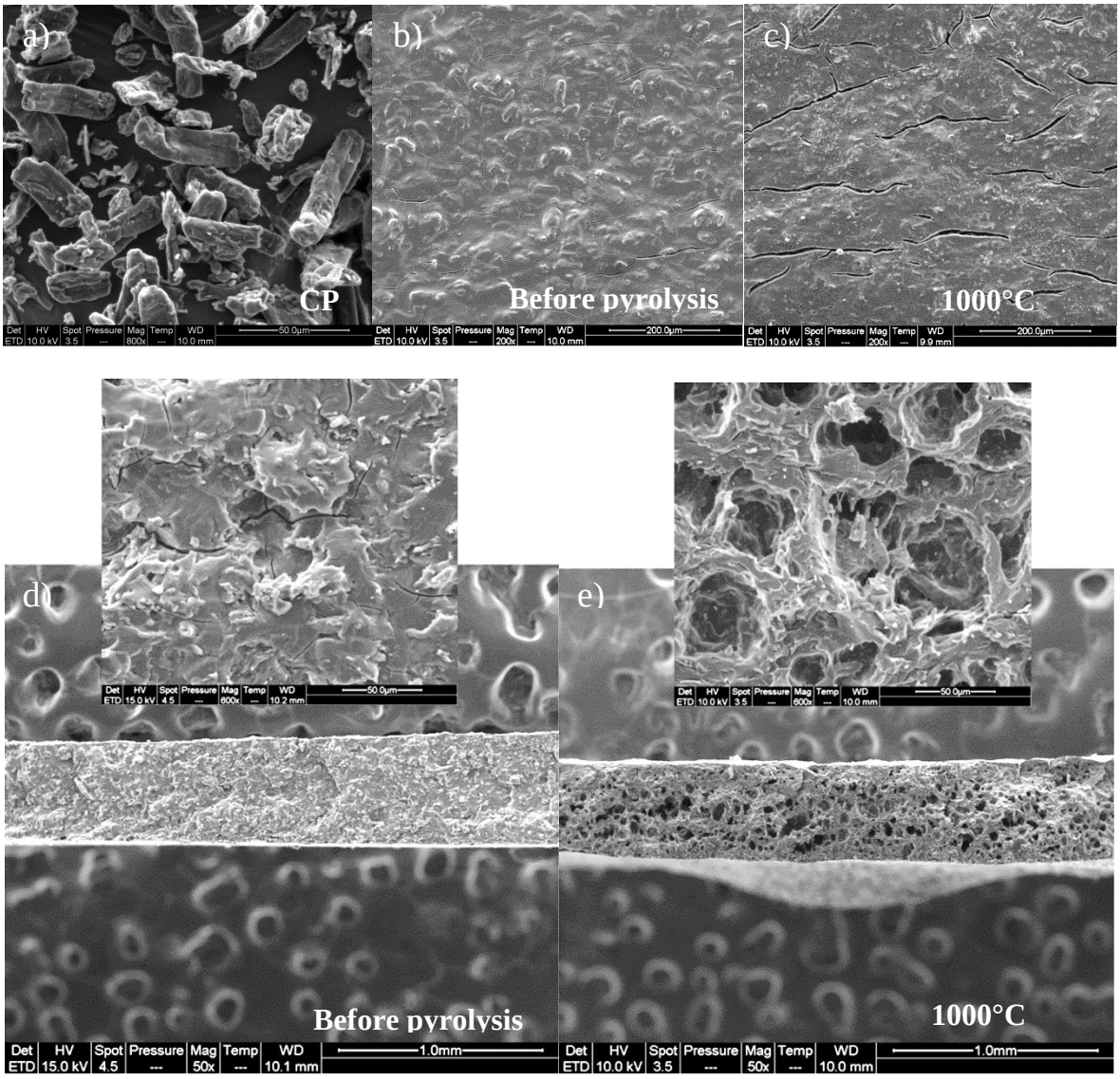

Fig 3.4.3 SEM observation of: a) as-received cellulose powder (CP); b) &c) surface of MFC/LS/CP precursor composite and its carbon after pyrolysis at 1000°C, respectively; d)&e) transversal section of samples corresponding to b) and c), respectively

3.4.4 Analysis of pyrolytic process of MFC/LS/CP composite

The TGA and DTG patterns of the tri-component composite are presented in Fig 3.4.4a) & b) and are compared to those of its constituents: cellulose powder and the binary composite of MFC/LS. CP exhibits a typical cellulose degradation peak at around 325°C with the maximum reaction rate reaching 13.2%/min (or 2.64%/°C). Its thermal degradation profile shows no difference compared to the published one in [123] where CP of the same origin

(Aldrich, 50µm) was examined. One remarkable phenomenon is that the used cellulose powder (powder form) decomposes much more intensively than microfibrillated cellulose (in the form of a fibrillated web), 13.2%/min compared to 6.1%/min and reaches the maximum reaction rate at a slightly lower temperature (325°C with regard to 334°C, respectively), as shown in Fig 3.4.4c). MFC is composed of smaller cellulose fibrils (L≈10 µm, D≈2-50 nm[12]) than CP. Due to the huge quantity of inter-fibril hydrogen bonds that construct the MFC "web", MFC decomposition is more or less inhibited[227–229]. As a result, MFC is thermally more stable than the powder formed CP. However, in the range of 230°C-300°C, MFC degrades slightly stronger than CP, probably due to its hemicellulose component[230] whose decomposition normally occurs at this temperatures[124]. In addition to that, many other factors may also affect thermal degradation of cellulosic products, such as cellulose source[231], bleaching degree[232], crystallinity[233] and impurities[234].

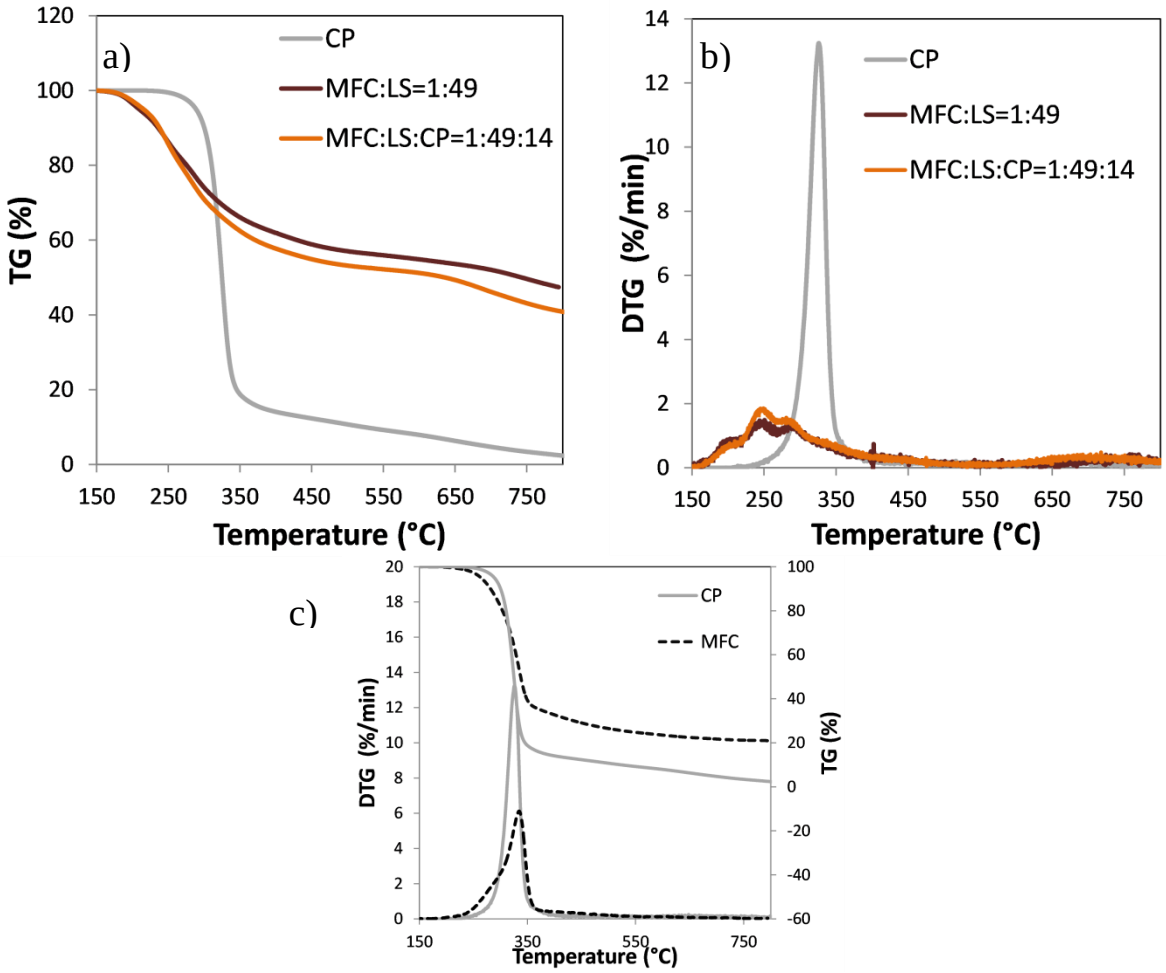

Fig 3.4.4 TG (a)) and DTG (b)) curves of the composite MFC/LS/CP and its constituents (cellulose powder and the composite MFC/LS); c) a comparison of thermal degradation between CP and MFC

Furthermore, it is remarkable that the triplet is rather thermally stable by generally following the thermal profile of its most important constituent, the binary composite, except for the region between 200°C and 280°C. Throughout this temperature range, the reaction rate of the

triplet is slightly higher than the binary composite, possibly due to the proportion of CP whose decomposition was catalyzed by the presence of Na from the binary composite by shifting to lower temperatures, as was proved in an earlier study[157]. The temperature shift of CP could be quantified from Fig 3.4.5a) where the theoretically calculated curve assuming an additivity law is obtained using Eq 3.4.1. The sodium-induced temperature shift of cellulose powder is consistent with the previously determined linear relationship describing how sodium content influences MFC decomposition in MFC/LS composites[157], as shown in Fig 3.4.5b).

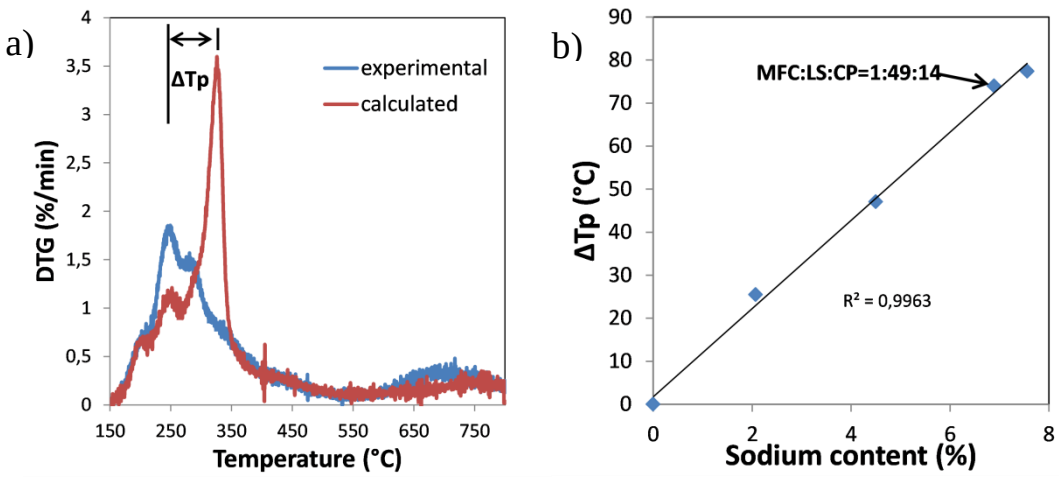

Fig 3.4.5 a) experimental and calculated DTG curves of the ternary composite MFC/LS/CP; b) the relationship of ΔTp with regard to the sodium content (the point representing the triple composite is indicated by a flash whereas the others represent MFC/LS composites

Eq 3.4.1 $$DTG(T)_{calculated} = \%\,CP \times DTG(T)_{CP} + \%binary\ composite \times DTG(T)_{binary\ composite}$$

3.4.5 Characterization of MFC/LS/CP carbons

3.4.5.1 Density evolution

Fig 3.4.6 exhibits both bulk and skeletal (true) densities of printed MFC/LS/CP "disk" and those of its derived carbons. According to it, the skeletal density of MFC/LS/CP carbon precursor is only slightly higher than the bulk one, 1.53 compared to 1.31 g/cm^3. It should be attributed to the low porosity that exists in such composite, *ca.* 0.146, induced by air-drying (as shown in Fig 3.4.3). During pyrolysis when HTT increases from 400 to 1200°C, quite different evolutions are observed for skeletal and bulk density.

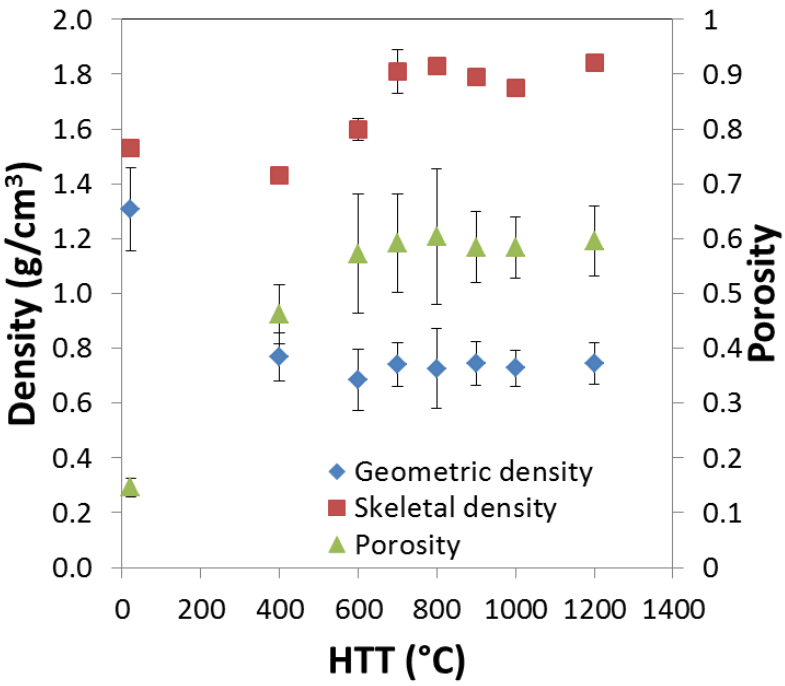

Fig 3.4.6 Density and porosity evolution of MFC/LS/CP carbons

Skeletal density of the obtained carbons globally rises from 1.43 to 1.84 g/cm^3 for a HTT increase from 400 to 1200°C, except for 900 and 1000°C, for which a slight density drop is observed. As commonly reported in the literature[205–208], such an increase of skeletal density with HTTs is considered as reflecting the continuous synthesis of highly organized carbon structures (turbostratic structures) that are more compact and denser than disordered carbon[205,206]. During pyrolysis, non-conjugated molecules either decompose as volatiles or convert into conjugated ones and the chars undergo aromatic condensation. Due to the existence of defects (oxygen components that are heat-resistant) and the randomly oriented graphite crystals (turbostratic nature), the maximum skeletal density of biochars is always below that of graphite (2.25 g/cm^3)[205,208].

Bulk density of biocarbons is the result of the competition between the HTT-induced weight loss and volumetric shrinkage. Bulk density importantly drops from 1.31 to 0.77 g/cm^3 when HTT increased at 400°C. After 400°C, the bulk densities of MFC/LS/CP carbons fluctuate within the range of 0.68 and 0.73 g/cm3, which seems to be less HTT-influenced.

The calculated porosities also increases with HTTs (Fig 3.4.6) at early stage of pyrolysis before stabilizing after 600°C, which is in agreement with the previous SEM observation (Fig 3.4.3) and the literature[206,207]. Compared to MFC/LS carbons, those derived from MFC/LS/CP precursor have significantly higher porosities, *ca.* 0.6 with regard to 0.37 at 1200°C. This value is approaching the result that was reported for wood chars[205]. The distinguished porosity between MFC/LS and MFC/LS/CP carbons is associated with the presence of CP in the formulation of the latter. According to its thermal degradation pattern in Fig 3.4.4c) as well as the SEM observation in Fig 3.4.3e), CP nearly disappears after 600°C (carbon yield <5%) thus leading to the formation of the pores whose dimensions are visibly similar to those of CP

particles. Thereby, a controlled porosity in the resulting carbons could be expected by simply a good dosage of CP quantity in the formulation of carbon precursor.

3.4.5.2 Microstructural evolution

The mutual evolution of the 3 identified phases (defect-free and defected graphene stacks as well as amorphous structures)[150] in the as-elaborated carbons provides essential information to understand the changes of their electrical and mechanical properties. As shown in Fig 3.4.7 and Table 3.4.1, both carbons present similar profiles in Raman spectra and XRD diffractograms, owing to their same fundamental constituents. Nevertheless, the small difference in proportions between LS-based precursor and cellulose-based precursors (MFC and CP) as well as their different aromatic condensation mechanisms during pyrolysis still led to a slight distinction in microstructural parameters as shown in Table 3.4.1. At 1000°C, MFC/LS/CP carbon contains less LS, 76.6% compared to 84% in MFC/LS carbon, which resulted the smaller size of graphene stacks and higher content of ordered structures (D+G ratio) although to a very limited degree.

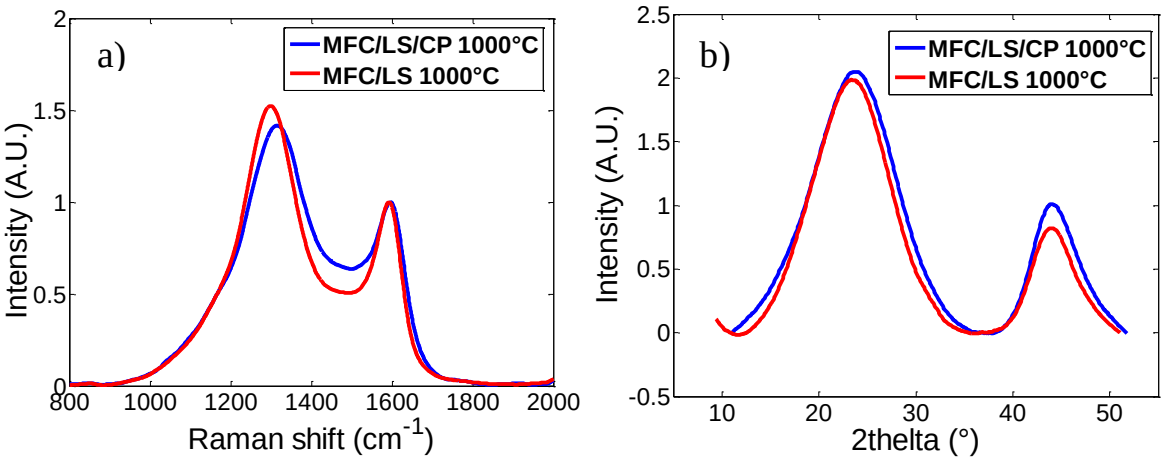

Fig 3.4.7 a) Raman spectrum and b) XRD diffractogram of 1000°C-synthesed MFC/LS/CP carbon, compared to the corresponding MFC/LS carbon

Table 3.4.1 Comparison of Raman and XRD characteristics between MFC/LS/CP and MFC/LS carbon of 1000°C

Precursor	LS proportion (%)	d_{002} (nm)	L_c (nm)	L_a (nm)	N	Raman band I_{D+G}/I_{total}
MFC:LS:CP=1:49:14	76.6	0.37	0.81	3.22	3.2	0.4768
MFC:LS=1:5.25	84	0.38	0.86	3.39	3.2	0.5047

3.4.5.3 Electrical conductivity

The bulk and the calculated skeletal conductivities (Eq 3.3.1) of MFC/LS/CP carbons are displayed in Fig 3.4.8. According to it, both skeletal and bulk conductivity of MFC/LS/CP carbons are highly HTT-depended and present 3 different regions as deeply interpreted in section 3.3.6.2: i) the appearance of mutual contacts between conductive carbon clusters when

600°C≤HTT≤700°C for which the skeletal electrical conductivity underdoes a sharp rise of 3 orders of magnitude, *ca.* from 0.001 to 1.054 S/cm; ii) the steady intensification of such contacts which arises from the growth of the conductive clusters for 700≤HTT≤1000, leading to a continuous improvement of the electrical conductivity from 1.054 to 164.58 S/cm ; iii) the slowed-down increase of the conductivity due to the already established current pathways that will be less-influence by the growth of conductive clusters for HTT>1000°C. Moreover, the difference between the bulk and skeletal density that increases at elevated HTT confirms the fact that the resulting carbons possess a more and more important porosity during pyrolysis, as revealed by density measurement (Fig 3.4.6). At 1000°C, MFC/LS carbon has a slightly higher skeletal conductivity than MFC/LS/CP carbon, 173.51 S/cm with regard to 164.58 S/cm. Such a difference collaborates with the previous observations in Table 3.4.1 that MFC/LS owns slightly larger size of graphene stacks and higher structural ordering (represented by D+G band ratio), that have been proved to be positively correlated with the electrical conductivity that is developed in engineering carbons during pyrolysis (section 3.3.6.2).

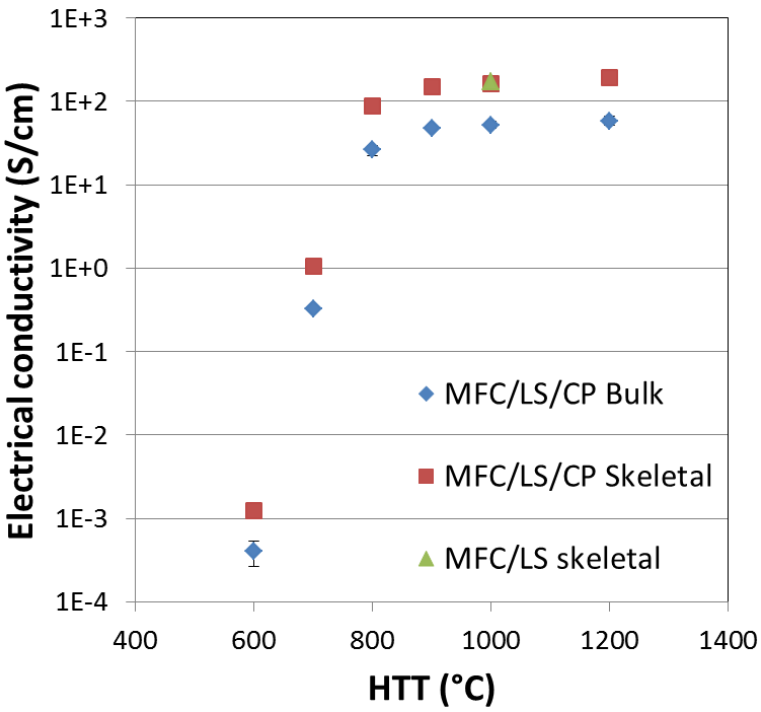

Fig 3.4.8 Bulk and calculated skeletal electrical conductivity of MFC/LS/CP carbons at corresponding HTTs (MFC/LS carbon at 1000°C given for comparison)

3.4.5.4 Mechanical properties

Pyrolysis-induced modifications of the mechanical strength of MFC/LS/CP samples were characterized by 3-point bending test. Despite the occasionally important deviation which is caused by the commonly reported heterogeneity[2,160,199] of engineering carbons (due to disordered or turbostratic carbon structures), the results shown in Fig 3.4.9 display a strongly HTT-dependent mechanical behavior for as-produced carbons whether carbonized or not, MFC/LS/CP are elasticity-dominated materials with no plastic zone except for non-

carbonized ones for which a short plastic zone just before rupture was observed. The slope, known as elastic modulus E_f, and the peak stress from each stress-strain curve are exhibited as function of HTTs in Fig 3.4.9a) and b).

MFC/LS/CP carbon precursor exhibits a flexural elastic modulus of 4.05 GPa and a peak stress of 23.53 Mpa, according to Fig 3.4.9. Compared to the precursor, the carbonaceous char obtained at 400°C lose much mechanical strength reflecting in both elastic modulus and peak stress. It is associated with the intensive mass loss due to devolatilization that the char suffers from during this temperature range. The diminished mechanical property also coincides with the decrease of the skeletal and bulk density of MFC/LS/CP at 400°C (Fig 3.4.6). When HTT increases to 600-900°C, the temperature-strengthened mechanical properties become visible. Both flexural modulus and peak stress rise quite linearly with HTTs and reach their maximum (6.62 GPA and 29.79 MPa, respectively) at 900°C. After 900°C, further carbonization is found to lower the mechanical strength of the carbons.

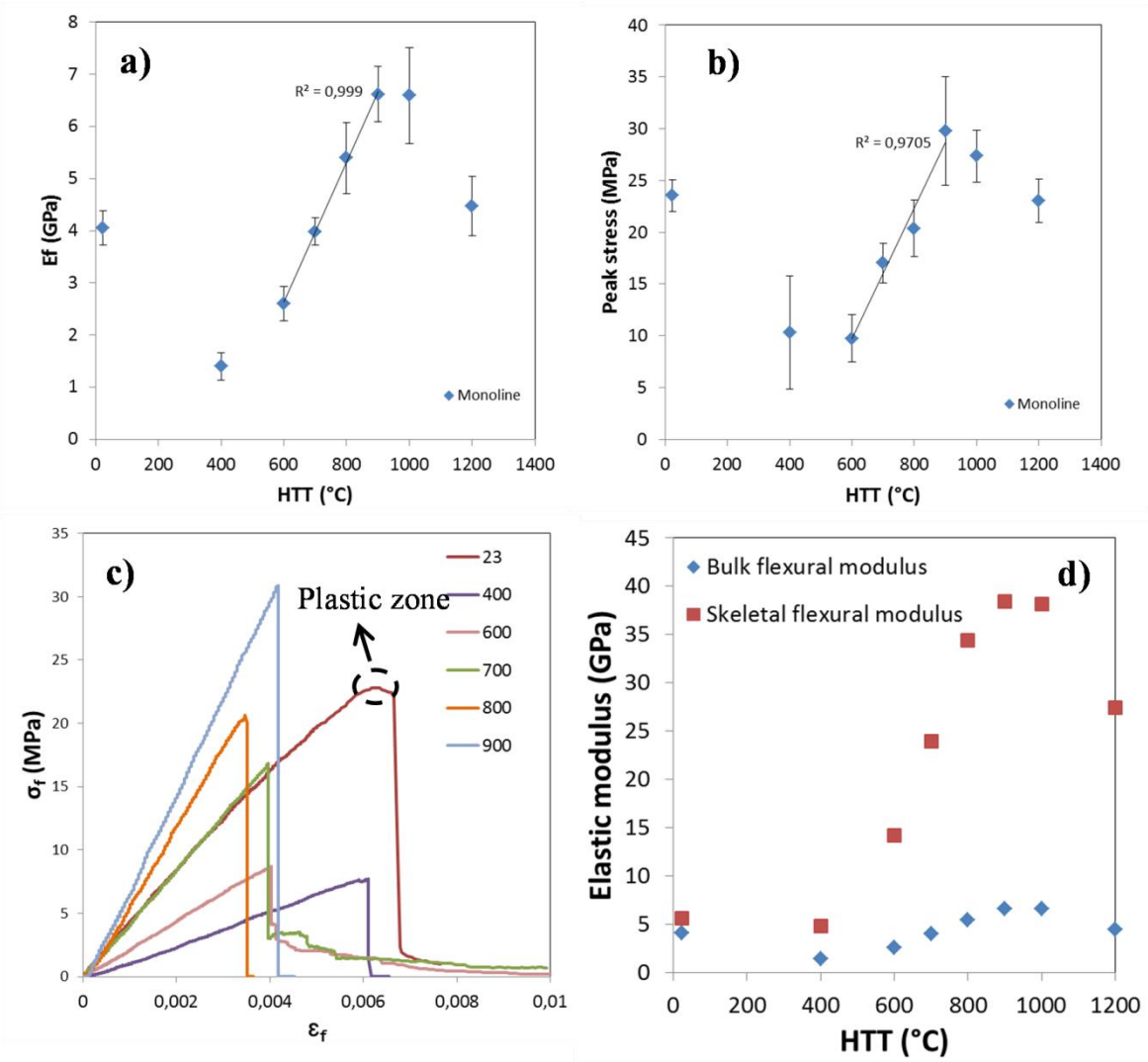

Fig 3.4.9 a) Elastic modulus and b) peak stress of MFC/LS/CP monolines pyrolyzed at different HTTs from 3-point bending tests; c) the flexural stress-strain profile of the samples; d) calculated skeletal elastic modulus with comparison to bulk ones

A linear-elastic beam deflection model was used to approximate the flexural modulus of the hard carbon of MFC/LS/CP[156,235], as shown in Eq 3.4.2:

Eq 3.4.2 $$\frac{E}{E_s} = (\frac{\rho}{\rho_s})^2$$

Where E and E_s correspond to the bulk and skeletal elastic modulus of the carbon; ρ and ρ_s are respectively the bulk and skeletal density. The approximate Young's modulus data of the MFC/LS/CP hard carbon are displayed in Fig 3.4.9d). Because of the porosity effect, the skeletal modulus is found to be higher than the bulk one and the difference between them is largely pronounced throughout the HTT range of 600-1200°C where the porosity is also intensively present. The resulting hard carbon achieves the best Young's modulus as high as 38.4 GPa at 900°C, that is nearly 1.5 higher than that of polycrystalline graphite (27GPa[156,235]).

3.4.6 Conclusions

The last part of the thesis examined the feasibility of manufacturing electrically conductive and mechanically resistant carbon structures by 3D printing and subsequent pyrolysis using MFC/LS/CP formulation. MFC, LS and CP are purely bio-sourced materials. Their water-processing and interesting rheological properties (high viscosity, shear-thinning profile and the short relaxation duration) account for the success of manufacturing well-shaped hydrogels by 3D printing. The printed MFC/LS/CP hydrogels were proved to be morphologically stable to air drying and to the subsequent pyrolysis. Owing to the presence of CP that is thermally less-stable, the resulting carbons exhibit improved porosity at elevated HTTs, compared to MFC/LS carbons. Such an increase in porosity is supposed to promote the use of MFC/LS/CP carbons in energy storage devices. At 900°C, MFC/LS/CP carbons not only result in a high electrical conductivity of 47.8 S/cm together with a low bulk density of 0.74 g/cm^3 as well as an important porosity of 0.58, but also achieve an elastic modulus maximum of 6.62 Gpa. It is believed by authors that the interesting electrical and mechanical results obtained will lead to a promising application as electrode materials for MFC/LS/CP biocarbons in close future.

4. Conclusions and perspectives

4 Conclusions and perspectives

Nowadays, the ever increasing environmental issues require the valorization of green materials in all domains. The current work elaborated biocarbons by slow pyrolysis from MFC/LS and MFC/LS/CP precursors that are purely lignocellulosic materials. The studies conducted in previous sections evaluate the usability of such blends as engineering carbon precursors in terms of rheology, thermal and kinetic characterization as well as carbon properties.

The study of rheological properties of MFC/LS hydrogels revealed that adding LS into MFC hydrogels led to either a disruption of the hydrogels' stability after 3D printing due to lack of viscosity (with 10%-30% LS), or a loss of shape definition because of the long restauration time (with 50% LS). The improved formulation by using CP as additive obtained not only a strengthened viscosity by 2-3 magnitudes but also a largely shorted restoration duration from 27s to 4s while keeping the shear-thinning profile. The objects printed using MFC/LS/CP formulation had good definition, which also collaborate with the rheological conclusions.

The TG/DTG analysis showed hierarchically thermal degradation patterns between LS, MFC and CP. Cellulose degrades intensively within a narrow temperature range between 250°C and 350°C, while LS decomposes much more gently within 2 main temperature ranges, 150°C-500°C and 600°C -800°C. However, despite the same chemical composition, CP decomposes much more intensively than MFC due to lack of huge quantity of hydrogen bonds. Furthermore, the catalytic effect of sodium has been confirmed in both MFC/LS and MFC/LS/CP blends by a highly correlated relationship between T_p shift and sodium content.

MFC/LS biocarbons elaborated from a wide range of heat treatment temperatures (HTTs: 400-1200°C) were characterized in the morphological, physicochemical and microstructural properties. They have been proved to be heat-resistant and morphologically stable to slow pyrolysis. FTIR results provided evidences concerning the loss of the majority of functional groups during heat treatment and only a few oxygen-containing structures were retained from high-temperature pyrolysis. Microstructural characterization by Raman revealed that the resulting carbons are composed of i) defect-free (regular) graphene stacks (3 layers of graphene, according to XRD); ii) defected (mainly oxygen) graphene structures and iii) amorphous phases. As a result of the growing of conductive phases (regular and defected) in addition to the reduction of the insulating ones (amorphous), a general increase of electrical conductivity was observed in MFC/LS hard carbons as function of HTTs although the mechanisms for the conductivity development are not the same in different HTT ranges. Based on that, a model describing the electrical conductivity development in MFC/LS hard carbons was proposed. After carbonization at 1000°C, biocarbons from MFC/LS precursors are still self-standing sheets and could achieve quite interesting electrical conductivity (95 S/cm) compared to their relatively low density 1.14 g/cm^3. The resulting physical properties are really outstanding in comparison with previously reported biocarbons.

Based on the previous conclusions, an improved formulation of using MFC/LS/CP blends accounts for a final success of elaborating electrically conductive and mechanically resistant carbon structures. Owing to the presence of CP that yields nearly nothing after 600°C, a controllable porosity in the resulting carbons could be expected by simply a good dosage of CP quantity in the formulation of carbon precursor. Such a controllable porosity is supposed to promote the use of MFC/LS/CP carbons in energy storage devices. At 900°C, MFC/LS/CP carbons not only result in a high electrical conductivity of 47.8 S/cm together with a low bulk density of 0.74 g/cm^3 as well as an important porosity of 0.58, but also achieve an elastic modulus maximum of 6.62 Gpa.

Clearly, physical properties of engineering carbons could be optimized by the control of the carbonization process and the carbon precursor formulation. Due to specific thermal degradation patterns of each component, a controllable porosity could be resulted at different temperature ranges. Moreover, a low heating rate is essential to obtain carbonaceous char with a good morphological stability. It is believed by authors that the interesting electrical and mechanical results obtained will lead to a promising application as electrode materials for MFC/LS/CP biocarbons in close future. In all, it is believed that this work proposes a new way to elaborate electrodes by 3D printing. It also verifies and could promote the use of lignocellulosic materials as active materials in energy storage devices after simply a slow pyrolysis process. The synthesized host material could promise the future electrodes a high specific capacity and a good cycling safety owing to its controllable porosity and low density.

Furthermore, the experiences of using 3D printing in this work make it possible to produce samples with flexible forms and dimensions in order to meet different characterization purposes. In the scale of laboratory, small objects in the form of single line or thin film could be elaborated for the corresponding mechanical or electrical characterization. From a point of view of applications, larger objects could be manufactured after an appropriate formulation in order to meet rheological requirements. More excitingly, electrodes of energy storage devices (*i.e.* Li-ion battery) could be directly printed using a two-head printer with one head firstly printing a host material then another filling with other types of hydrogel (probably electrochemistry-strengthen components). As a result, 3D printing not only amplifies the potential applications of MFC/LS/CP as a printable hydrogel but also proposes an unexplored way to elaborate electrodes of next generation. In future, work will be focused on more advanced formulations of 3D printing “ink” by including, for instance, UV-curing components for fast manufacturing. Functional materials could also be formed by 3D printing using carbon/metal formulations.

5. References

5 References

1. Pandolfo, A. G. & Hollenkamp, A. F. Carbon properties and their role in supercapacitors. *J. Power Sources* **157,** 11–27 (2006).
2. Burchell, T. D. *Carbon Materials for Advanced Technologies*. (Elsevier, 1999).
3. Lehmann, J. & Joseph, S. *Biochar for Environmental Management: Science, Technology and Implementation*. (Routledge, 2015).
4. Liu, W.-J., Jiang, H. & Yu, H.-Q. Development of Biochar-Based Functional Materials: Toward a Sustainable Platform Carbon Material. *Chem. Rev.* **115,** 12251–12285 (2015).
5. Ippolito, J. A., Laird, D. A. & Busscher, W. J. Environmental Benefits of Biochar. *J. Environ. Qual.* **41,** 967–972 (2012).
6. Perepelkin, K. E. Carbon fibres with specific physical and physicochemical properties based on hydrated cellulose and polyacrylonitrile precursors. A review. *Fibre Chem.* **34,** 271–280 (2002).
7. Liu, W.-J., Tian, K., He, Y.-R., Jiang, H. & Yu, H.-Q. High-Yield Harvest of Nanofibers/Mesoporous Carbon Composite by Pyrolysis of Waste Biomass and Its Application for High Durability Electrochemical Energy Storage. *Environ. Sci. Technol.* **48,** 13951–13959 (2014).
8. Jin, J., Yu, B., Shi, Z., Wang, C. & Chong, C. Lignin-based electrospun carbon nanofibrous webs as free-standing and binder-free electrodes for sodium ion batteries. *J. Power Sources* **272,** 800–807 (2014).
9. Wang, Y., Zou, Y., Chen, J., Li, G.-D. & Xu, Y. A flexible and monolithic nanocomposite aerogel of carbon nanofibers and crystalline titania: fabrication and applications. *RSC Adv.* **3,** 24163 (2013).
10. Rhim, Y.-R. *et al.* Changes in electrical and microstructural properties of microcrystalline cellulose as function of carbonization temperature. *Carbon* **48,** 1012–1024 (2010).
11. Mun, S. P., Cai, Z. & Zhang, J. Fe-catalyzed thermal conversion of sodium lignosulfonate to graphene. *Mater. Lett.* **100,** 180–183 (2013).
12. Lavoine, N., Desloges, I., Dufresne, A. & Bras, J. Microfibrillated cellulose – Its barrier properties and applications in cellulosic materials: A review. *Carbohydr. Polym.* **90,** 735–764 (2012).
13. González, I. *et al.* From paper to nanopaper: evolution of mechanical and physical properties. *Cellulose* **21,** 2599–2609 (2014).
14. Myrvold, B. O. A new model for the structure of lignosulphonates: Part 1. Behaviour in dilute solutions. *Ind. Crops Prod.* **27,** 214–219 (2008).
15. Shao, Y., Chaussy, D., Grosseau, P. & Beneventi, D. Use of Microfibrillated Cellulose/Lignosulfonate Blends as Carbon Precursors: Impact of Hydrogel Rheology on 3D Printing. *Ind. Eng. Chem. Res.* (2015). doi:10.1021/acs.iecr.5b02763
16. Shao, Y., Guizani, C., Grosseau, P., Chaussy, D. & Beneventi, D. Thermal characterization and kinetic analysis of microfibrillated cellulose/lignosulfonate blends. *J. Anal. Appl. Pyrolysis* doi:10.1016/j.jaap.2017.03.001
17. Mauter, M. S. & Elimelech, M. Environmental Applications of Carbon-Based Nanomaterials. *Environ. Sci. Technol.* **42,** 5843–5859 (2008).
18. Michio, I. & Kang, F. *Carbon Materials Science and Engineering: From Fundamentals to Applications*. (清华大学出版社有限公司, 2006).
19. Baker, D. A. & Rials, T. G. Recent advances in low-cost carbon fiber manufacture from lignin. *J. Appl. Polym. Sci.* **130,** 713–728 (2013).
20. Norberg, I. Carbon fibres from kraft lignin. (KTH Royal, 2012).
21. Dumitriu, S. *Polysaccharides: Structural Diversity and Functional Versatility, Second Edition*. (CRC Press, 2004).
22. Higuchi, T. *Biosynthesis and biodegradation of wood components*. (Elsevier, 2012).

23. Barnett, J. R. & Bonham, V. A. Cellulose microfibril angle in the cell wall of wood fibres. *Biol. Rev.* **79,** 461–472 (2004).
24. Klemm, D., Heublein, B., Fink, H.-P. & Bohn, A. Cellulose: Fascinating Biopolymer and Sustainable Raw Material. *Angew. Chem. Int. Ed.* **44,** 3358–3393 (2005).
25. Habibi, Y., Lucia, L. A. & Rojas, O. J. Cellulose Nanocrystals: Chemistry, Self-Assembly, and Applications. *Chem. Rev.* **110,** 3479–3500 (2010).
26. Jarvis, M. Chemistry: Cellulose stacks up. *Nature* **426,** 611–612 (2003).
27. Mazeau, K. & Heux, L. Molecular Dynamics Simulations of Bulk Native Crystalline and Amorphous Structures of Cellulose. *J. Phys. Chem. B* **107,** 2394–2403 (2003).
28. Azizi Samir, M. A. S., Alloin, F. & Dufresne, A. Review of Recent Research into Cellulosic Whiskers, Their Properties and Their Application in Nanocomposite Field. *Biomacromolecules* **6,** 612–626 (2005).
29. Goring, D. A. I. & Timell, T. E. Molecular weight of native celluloses. *Tappi* **45,** 454–460 (1962).
30. Pettersen, R. C. The chemical composition of wood. *Chem. Solid Wood* **207,** 57–126 (1984).
31. Ebringerová, A. Structural Diversity and Application Potential of Hemicelluloses. *Macromol. Symp.* **232,** 1–12 (2005).
32. Belgacem, M. N. & Gandini, A. *Monomers, Polymers and Composites from Renewable Resources*. (Elsevier, 2011).
33. Kadla, J. F. *et al.* Lignin-based carbon fibers for composite fiber applications. *Carbon* **40,** 2913–2920 (2002).
34. Lora, J. H. & Glasser, W. G. Recent industrial applications of lignin: a sustainable alternative to nonrenewable materials. *J. Polym. Environ.* **10,** 39–48 (2002).
35. Hu, B. *et al.* Engineering Carbon Materials from the Hydrothermal Carbonization Process of Biomass. *Adv. Mater.* **22,** 813–828 (2010).
36. Wang, L., Schütz, C., Salazar-Alvarez, G. & Titirici, M.-M. Carbon aerogels from bacterial nanocellulose as anodes for lithium ion batteries. *RSC Adv.* **4,** 17549 (2014).
37. Tarascon, J.-M. & Armand, M. Issues and challenges facing rechargeable lithium batteries. *Nature* **414,** 359–367 (2001).
38. Dunn, B., Kamath, H. & Tarascon, J.-M. Electrical energy storage for the grid: a battery of choices. *Science* **334,** 928–935 (2011).
39. Schalkwijk, W. A. van. & Scrosati, B. *Advances in lithium-ion batteries*. (Kluwer Academic/Plenum Publishers, 2002).
40. Jabbour, L., Bongiovanni, R., Chaussy, D., Gerbaldi, C. & Beneventi, D. Cellulose-based Li-ion batteries: a review. *Cellulose* **20,** 1523–1545 (2013).
41. Jabbour, L. Utilisation de procédés papetiers et de fibres cellulosiques pour l'élaboration de batteries Li-ion Elaboration of Li-ion batteries using cellulose fibers and papermaking techniques. (Université de Grenoble, 2012).
42. Wakihara, M. & Yamamoto, O. *Lithium Ion Batteries: Fundamentals and Performance*. (John Wiley & Sons, 2008).
43. Araki, J., Wada, M., Kuga, S. & Okano, T. Flow properties of microcrystalline cellulose suspension prepared by acid treatment of native cellulose. *Colloids Surf. Physicochem. Eng. Asp.* **142,** 75–82 (1998).
44. Araki, J., Wada, M., Kuga, S. & Okano, T. Birefringent Glassy Phase of a Cellulose Microcrystal Suspension. *Langmuir* **16,** 2413–2415 (2000).
45. Dong, X. M., Kimura, T., Revol, J.-F. & Gray, D. G. Effects of Ionic Strength on the Isotropic−Chiral Nematic Phase Transition of Suspensions of Cellulose Crystallites. *Langmuir* **12,** 2076–2082 (1996).

46. Gama, M., Gatenholm, P. & Klemm, D. *Bacterial NanoCellulose: A Sophisticated Multifunctional Material*. (CRC Press, 2012).
47. Nimeskern, L. *et al.* Mechanical evaluation of bacterial nanocellulose as an implant material for ear cartilage replacement. *J. Mech. Behav. Biomed. Mater.* **22,** 12–21 (2013).
48. Klemm, D. *et al.* Nanocelluloses: A New Family of Nature-Based Materials. *Angew. Chem. Int. Ed.* **50,** 5438–5466 (2011).
49. Wågberg, L. *et al.* The Build-Up of Polyelectrolyte Multilayers of Microfibrillated Cellulose and Cationic Polyelectrolytes. *Langmuir* **24,** 784–795 (2008).
50. Fleming, K., Gray, D., Prasannan, S. & Matthews, S. Cellulose Crystallites: A New and Robust Liquid Crystalline Medium for the Measurement of Residual Dipolar Couplings. *J. Am. Chem. Soc.* **122,** 5224–5225 (2000).
51. Alemdar, A. & Sain, M. Isolation and characterization of nanofibers from agricultural residues – Wheat straw and soy hulls. *Bioresour. Technol.* **99,** 1664–1671 (2008).
52. Dufresne, A., Cavaille, J.-Y. & Vignon, M. R. Mechanical behavior of sheets prepared from sugar beet cellulose microfibrils. *J. Appl. Polym. Sci.* **64,** 1185–1194 (1997).
53. Roux, J. C. & Mayade, T. L. Modeling of the particle breakage kinetics in the wet mills for the paper industry. *Powder Technol.* **105,** 237–242 (1999).
54. Turbak, A. F., Snyder, F. W. & Sandberg, K. R. Microfibrillated Cellulose, a New Cellulose Product: Properties, Uses, and Commercial Potential. *J Appl Polym Sci Appl Polym Symp U. S.* **37,** (1983).
55. Nakagaito, A. N. & Yano, H. The effect of morphological changes from pulp fiber towards nano-scale fibrillated cellulose on the mechanical properties of high-strength plant fiber based composites. *Appl. Phys. A* **78,** 547–552 (2003).
56. Hamad, W. Y. Some microrheological aspects of wood-pulp fibres subjected to fatigue loading. *Cellulose* **4,** 51–56
57. Eriksen, O., Syverud, K. & Gregersen, O. The use of microfibrillated cellulose produced from kraft pulp as strength enhancer in TMP paper. *Nord. Pulp Pap. Res. J.* **23,** 299–304 (2008).
58. Lindström, T. & Ankerfors, M. Seventh International Paper and Coating Chemistry Symposium. *Hamilt. Can. June* 10–12 (2009).
59. Pääkkö, M. *et al.* Enzymatic Hydrolysis Combined with Mechanical Shearing and High-Pressure Homogenization for Nanoscale Cellulose Fibrils and Strong Gels. *Biomacromolecules* **8,** 1934–1941 (2007).
60. Isogai, A., Saito, T. & Fukuzumi, H. TEMPO-oxidized cellulose nanofibers. *Nanoscale* **3,** 71–85 (2011).
61. Wågberg, L., Winter, L., Ödberg, L. & Lindström, T. On the charge stoichiometry upon adsorption of a cationic polyelectrolyte on cellulosic materials. *Colloids Surf.* **27,** 163–173 (1987).
62. Henriksson, M., Henriksson, G., Berglund, L. A. & Lindström, T. An environmentally friendly method for enzyme-assisted preparation of microfibrillated cellulose (MFC) nanofibers. *Eur. Polym. J.* **43,** 3434–3441 (2007).
63. Eichhorn, S. J. *et al.* Review: current international research into cellulose nanofibres and nanocomposites. *J. Mater. Sci.* **45,** 1 (2009).
64. Horvath, A. E. & Lindström, T. The influence of colloidal interactions on fiber network strength. *J. Colloid Interface Sci.* **309,** 511–517 (2007).
65. Nechyporchuk, O., Belgacem, M. N. & Pignon, F. Rheological properties of micro-/nanofibrillated cellulose suspensions: Wall-slip and shear banding phenomena. *Carbohydr. Polym.* **112,** 432–439 (2014).
66. Jia, X. *et al.* Rheological properties of an amorphous cellulose suspension. *Food Hydrocoll.* **39,** 27–33 (2014).

67. Iotti, M., Gregersen, Ø. W., Moe, S. & Lenes, M. Rheological Studies of Microfibrillar Cellulose Water Dispersions. *J. Polym. Environ.* **19,** 137–145 (2010).
68. Agoda-Tandjawa, G. *et al.* Rheological characterization of microfibrillated cellulose suspensions after freezing. *Carbohydr. Polym.* **80,** 677–686 (2010).
69. Karppinen, A. *et al.* Flocculation of microfibrillated cellulose in shear flow. *Cellulose* **19,** 1807–1819 (2012).
70. Karppinen, A., Vesterinen, A.-H., Saarinen, T., Pietikäinen, P. & Seppälä, J. Effect of cationic polymethacrylates on the rheology and flocculation of microfibrillated. *Cellulose* **18,** 1381–1390 (2011).
71. Barnes, H. A. Thixotropy—a review. *J. Non-Newton. Fluid Mech.* **70,** 1–33 (1997).
72. Rees, A. *et al.* 3D bioprinting of carboxymethylated-periodate oxidized nanocellulose constructs for wound dressing applications. *BioMed Res. Int.* (2014).
73. Kumar, V. *et al.* Comparison of nano- and microfibrillated cellulose films. *Cellulose* **21,** 3443–3456 (2014).
74. Sehaqui, H., Liu, A., Zhou, Q. & Berglund, L. A. Fast Preparation Procedure for Large, Flat Cellulose and Cellulose/Inorganic Nanopaper Structures. *Biomacromolecules* **11,** 2195–2198 (2010).
75. Henriksson, M., Berglund, L. A., Isaksson, P., Lindström, T. & Nishino, T. Cellulose Nanopaper Structures of High Toughness. *Biomacromolecules* **9,** 1579–1585 (2008).
76. Sehaqui, H. Nanofiber networks, aerogels and biocomposites based on nanofibrillated cellulose from wood. (2011).
77. Spence, K. L., Venditti, R. A., Rojas, O. J., Habibi, Y. & Pawlak, J. J. A comparative study of energy consumption and physical properties of microfibrillated cellulose produced by different processing methods. *Cellulose* **18,** 1097–1111 (2011).
78. Baez, C., Considine, J. & Rowlands, R. Influence of drying restraint on physical and mechanical properties of nanofibrillated cellulose films. *Cellulose* **21,** 347–356 (2014).
79. Jentzen, C. A. The effect of stress applied during drying on some of the properties of individual pulp fibers. *Tappi* **47,** 412–418 (1964).
80. Moon, R. J., Martini, A., Nairn, J., Simonsen, J. & Youngblood, J. Cellulose nanomaterials review: structure, properties and nanocomposites. *Chem. Soc. Rev.* **40,** 3941–3994 (2011).
81. Virtanen, S., Vartianen, J., Setälä, H., Tammelin, T. & Vuoti, S. Modified nanofibrillated cellulose–polyvinyl alcohol films with improved mechanical performance. *RSC Adv.* **4,** 11343 (2014).
82. Klemm, D. *et al.* Nanocelluloses as Innovative Polymers in Research and Application. in *Polysaccharides II* (ed. Klemm, D.) 49–96 (Springer Berlin Heidelberg, 2006). doi:10.1007/12_097
83. Jabbour, L. *et al.* Microfibrillated cellulose–graphite nanocomposites for highly flexible paper-like Li-ion battery electrodes. *J. Mater. Chem.* **20,** 7344 (2010).
84. Chiappone, A. *et al.* Microfibrillated cellulose as reinforcement for Li-ion battery polymer electrolytes with excellent mechanical stability. *J. Power Sources* **196,** 10280–10288 (2011).
85. Kenneth, A. E. B. Lignosulfonate/urea binder for particulate composites. (1987).
86. Browning, W. C. Lignosulfonate Challenge. in *Applied Polymer Symposia* **28,** 109–124 (DTIC Document, 1975).
87. Gardon, J. L. & Mason, S. G. Physicochemical Studies of Ligninsulphonates: I. Preparation and Properties of Fractionated Samples. *Can. J. Chem.* **33,** 1477–1490 (1955).
88. Heikkila, H. Production of pure sugars and lignosulfonates from sulfite spent liquor.
89. Fredheim, G. E. & Christensen, B. E. Polyelectrolyte Complexes: Interactions between Lignosulfonate and Chitosan. *Biomacromolecules* **4,** 232–239 (2003).

90. Lemes, A. P., Soto-Oviedo, M. A., Waldman, W. R., Innocentini-Mei, L. H. & Durán, N. Effect of Lignosulfonate on the Thermal and Morphological Behavior of Poly(3-hydroxybutyrate-co-3-hydroxyvalerate). *J. Polym. Environ.* **18,** 250–259 (2010).
91. Kauppi, A., Andersson, K. M. & Bergström, L. Probing the effect of superplasticizer adsorption on the surface forces using the colloidal probe AFM technique. *Cem. Concr. Res.* **35,** 133–140 (2005).
92. Shulga, G., Rekner, F. & Varslavan, J. SW—Soil and Water. *J. Agric. Eng. Res.* **78,** 309–316 (2001).
93. Huang, J., Zhang, L. & Chen, F. Effects of lignin as a filler on properties of soy protein plastics. I. Lignosulfonate. *J. Appl. Polym. Sci.* **88,** 3284–3290 (2003).
94. Vainio, U., Lauten, R. A. & Serimaa, R. Small-Angle X-ray Scattering and Rheological Characterization of Aqueous Lignosulfonate Solutions. *Langmuir* **24,** 7735–7743 (2008).
95. Barnes, H. A. & Hutton, J. F. *An Introduction to Rheology*. (Elsevier, 1989).
96. Marcus, Y. The sizes of molecules—revisited. *J. Phys. Org. Chem.* **16,** 398–408 (2003).
97. Werff, J. C. van der & Kruif, C. G. de. Hard-sphere Colloidal Dispersions: The Scaling of Rheological Properties with Particle Size, Volume Fraction, and Shear Rate. *J. Rheol. 1978-Present* **33,** 421–454 (1989).
98. Luckham, P. F. & Ukeje, M. A. Effect of Particle Size Distribution on the Rheology of Dispersed Systems. *J. Colloid Interface Sci.* **220,** 347–356 (1999).
99. Branca, C. & Blasi, C. D. A lumped kinetic model for banana peel combustion. *Thermochim. Acta* **614,** 68–75 (2015).
100. Koufopanos, C. A., Lucchesi, A. & Maschio, G. Kinetic modelling of the pyrolysis of biomass and biomass components. *Can. J. Chem. Eng.* **67,** 75–84 (1989).
101. Branca, C., Di Blasi, C. & Horacek, H. Analysis of the Combustion Kinetics and Thermal Behavior of an Intumescent System. *Ind. Eng. Chem. Res.* **41,** 2107–2114 (2002).
102. White, J. E., Catallo, W. J. & Legendre, B. L. Biomass pyrolysis kinetics: A comparative critical review with relevant agricultural residue case studies. *J. Anal. Appl. Pyrolysis* **91,** 1–33 (2011).
103. Galwey, A. K. & Brown, M. E. Application of the Arrhenius equation to solid state kinetics: can this be justified? *Thermochim. Acta* **386,** 91–98 (2002).
104. Atkins, P. W. *Physical Chemistry. 6th*. (Oxford University Press, 1998).
105. Garn, P. D. Kinetics of thermal decomposition of the solid state: II. Delimiting the homogeneous-reaction model. *Thermochim. Acta* **160,** 135–145 (1990).
106. Amutio, M. *et al.* Kinetic study of lignocellulosic biomass oxidative pyrolysis. *Fuel* **95,** 305–311 (2012).
107. Anca-Couce, A., Berger, A. & Zobel, N. How to determine consistent biomass pyrolysis kinetics in a parallel reaction scheme. *Fuel* **123,** 230–240 (2014).
108. Antal, M. J. J. & Varhegyi, G. Cellulose pyrolysis kinetics: the current state of knowledge. *Ind. Eng. Chem. Res.* **34,** 703–717 (1995).
109. Raghavan, V., Cohen, M. & Hannay, N. B. Treatise on Solid State Chemistry. *Vol 5Plenum N. Y.* 96 (1975).
110. Le Claire, A. D. & Hannay, N. B. Treatise on Solid State Chemistry. *Vol 4* 1 (1975).
111. Vyazovkin, S. & Wight, C. A. Isothermal and non-isothermal kinetics of thermally stimulated reactions of solids. *Int. Rev. Phys. Chem.* **17,** 407–433 (1998).
112. Bruzs, B. Velocity of Thermal Decomposition of Carbonates. *J. Phys. Chem.* **30,** 680–693 (1925).
113. Hüttig, G. F., Meller, A. & Lehmann, E. Die geschwindigkeit des zerfalls von zinkcarbonat in zinkoxyd und kohlendioxyd. *Z Phys Chem B* **19,** 1–21 (1932).
114. Koga, N. & Šesták, J. Kinetic compensation effect as a mathematical consequence of the exponential rate constant. *Thermochim. Acta* **182,** 201–208 (1991).

115. Kujirai, T. & Akahira, T. Effect of temperature on the deterioration of fibrous insulating materials. *Sci Pap Inst Phys Chem Res* **2,** 223–52 (1925).
116. Flynn, J. H. The 'Temperature Integral' — Its use and abuse. *Thermochim. Acta* **300,** 83–92 (1997).
117. Flynn, J. H. & Wall, L. A. General treatment of the thermogravimetry of polymers. *J Res Nat Bur Stand* **70,** 487–523 (1966).
118. Ozawa, T. A new method of analyzing thermogravimetric data. *Bull. Chem. Soc. Jpn.* **38,** 1881–1886 (1965).
119. Doyle, C. D. Estimating isothermal life from thermogravimetric data. *J. Appl. Polym. Sci.* **6,** 639–642 (1962).
120. Vyazovkin, S. & Dollimore, D. Linear and Nonlinear Procedures in Isoconversional Computations of the Activation Energy of Nonisothermal Reactions in Solids. *J. Chem. Inf. Comput. Sci.* **36,** 42–45 (1996).
121. Cai, J. M. & Bi, L. S. Kinetic analysis of wheat straw pyrolysis using isoconversional methods. *J. Therm. Anal. Calorim.* **98,** 325–330 (2009).
122. Cagnon, B., Py, X., Guillot, A., Stoeckli, F. & Chambat, G. Contributions of hemicellulose, cellulose and lignin to the mass and the porous properties of chars and steam activated carbons from various lignocellulosic precursors. *Bioresour. Technol.* **100,** 292–298 (2009).
123. Yang, H., Yan, R., Chen, H., Lee, D. H. & Zheng, C. Characteristics of hemicellulose, cellulose and lignin pyrolysis. *Fuel* **86,** 1781–1788 (2007).
124. Yang, H. *et al.* In-Depth Investigation of Biomass Pyrolysis Based on Three Major Components: Hemicellulose, Cellulose and Lignin. *Energy Fuels* **20,** 388–393 (2006).
125. Worasuwannarak, N., Sonobe, T. & Tanthapanichakoon, W. Pyrolysis behaviors of rice straw, rice husk, and corncob by TG-MS technique. *J. Anal. Appl. Pyrolysis* **78,** 265–271 (2007).
126. Stefanidis, S. D. *et al.* A study of lignocellulosic biomass pyrolysis via the pyrolysis of cellulose, hemicellulose and lignin. *J. Anal. Appl. Pyrolysis* **105,** 143–150 (2014).
127. Kim, S. & Eom, Y. Estimation of kinetic triplet of cellulose pyrolysis reaction from isothermal kinetic results. *Korean J. Chem. Eng.* **23,** 409–414 (2006).
128. Müller-Hagedorn, M., Bockhorn, H., Krebs, L. & Müller, U. A comparative kinetic study on the pyrolysis of three different wood species. *J. Anal. Appl. Pyrolysis* **68–69,** 231–249 (2003).
129. Jakab, E., Faix, O., Till, F. & Székely, T. Thermogravimetry/Mass Spectrometry of Various Lignosulfonates as well as of a Kraft and Acetosolv Lignin. *Holzforsch. - Int. J. Biol. Chem. Phys. Technol. Wood* **45,** 355–360 (2009).
130. Jakab, E., Faix, O., Till, F. & Székely, T. Proceedings of the 10th International Conference on Fundamental Aspects, Processes and Applications of PyrolysisThe effect of cations on the thermal decomposition of lignins. *J. Anal. Appl. Pyrolysis* **25,** 185–194 (1993).
131. Li, B., Lv, W., Zhang, Q., Wang, T. & Ma, L. Pyrolysis and catalytic pyrolysis of industrial lignins by TG-FTIR: Kinetics and products. *J. Anal. Appl. Pyrolysis* **108,** 295–300 (2014).
132. Liu, Q., Zhong, Z., Wang, S. & Luo, Z. Interactions of biomass components during pyrolysis: A TG-FTIR study. *J. Anal. Appl. Pyrolysis* **90,** 213–218 (2011).
133. Wang, S., Guo, X., Wang, K. & Luo, Z. Influence of the interaction of components on the pyrolysis behavior of biomass. *J. Anal. Appl. Pyrolysis* **91,** 183–189 (2011).
134. Hosoya, T., Kawamoto, H. & Saka, S. Cellulose–hemicellulose and cellulose–lignin interactions in wood pyrolysis at gasification temperature. *J. Anal. Appl. Pyrolysis* **80,** 118–125 (2007).

135. Rao, T. R. & Sharma, A. Pyrolysis rates of biomass materials. *Energy* **23,** 973–978 (1998).
136. Manyà, J. J., Velo, E. & Puigjaner, L. Kinetics of Biomass Pyrolysis: a Reformulated Three-Parallel-Reactions Model. *Ind. Eng. Chem. Res.* **42,** 434–441 (2003).
137. Orfao, J. J. M., Antunes, F. J. A. & Figueiredo, J. L. Pyrolysis kinetics of lignocellulosic materials—three independent reactions model. *Fuel* **78,** 349–358 (1999).
138. Raveendran, K., Ganesh, A. & Khilar, K. C. Influence of mineral matter on biomass pyrolysis characteristics. *Fuel* **74,** 1812–1822 (1995).
139. Nassar, M. M. Thermal Analysis Kinetics of Bagasse and Rice Straw. *Energy Sources* **20,** 831–837 (1998).
140. Varhegyi, G., Antal, M. J., Szekely, T., Till, F. & Jakab, E. Simultaneous thermogravimetric-mass spectrometric studies of the thermal decomposition of biopolymers. 1. Avicel cellulose in the presence and absence of catalysts. *Energy Fuels* **2,** 267–272 (1988).
141. Brunner, P. H. & Roberts, P. V. The significance of heating rate on char yield and char properties in the pyrolysis of cellulose. *Carbon* **18,** 217–224 (1980).
142. Ahmed, I. I. & Gupta, A. K. Pyrolysis and gasification of food waste: Syngas characteristics and char gasification kinetics. *Appl. Energy* **87,** 101–108 (2010).
143. Dumanlı, A. G. & Windle, A. H. Carbon fibres from cellulosic precursors: a review. *J. Mater. Sci.* **47,** 4236–4250 (2012).
144. Gao, M., Ling, B., Yang, S. & Zhao, M. Flame retardance of wood treated with guanidine compounds characterized by thermal degradation behavior. *J. Anal. Appl. Pyrolysis* **73,** 151–156 (2005).
145. Zeng, F., Pan, D. & Pan, N. Choosing the Impregnants by Thermogravimetric Analysis for Preparing Rayon-Based Carbon Fibers. *J. Inorg. Organomet. Polym. Mater.* **15,** 261–267 (2005).
146. Lysenko, A. A., Piskunova, I. A. & Astashkina, O. V. Effect of Inorganic and Organosilicon Additives on Pyrolysis of Hydrated Cellulose Fibre Materials. *Fibre Chem.* **35,** 189–192 (2003).
147. Kim, D.-Y., Nishiyama, Y., Wada, M. & Kuga, S. High-yield Carbonization of Cellulose by Sulfuric Acid Impregnation. *Cellulose* **8,** 29–33 (2001).
148. Ishida, O., Kim, D.-Y., Kuga, S., Nishiyama, Y. & Brown, R. M. Microfibrillar carbon from native cellulose. *Cellulose* **11,** 475–480 (2004).
149. Sevilla, M. & Fuertes, A. B. Graphitic carbon nanostructures from cellulose. *Chem. Phys. Lett.* **490,** 63–68 (2010).
150. McDonald-Wharry, J. S., Manley-Harris, M. & Pickering, K. L. Reviewing, Combining, and Updating the Models for the Nanostructure of Non-Graphitizing Carbons Produced from Oxygen-Containing Precursors. *Energy Fuels* (2016). doi:10.1021/acs.energyfuels.6b00917
151. Radovic, L. R. *Chemistry & Physics of Carbon*. (CRC Press, 2000).
152. Guerrero, M., Ruiz, M. P., Millera, Á., Alzueta, M. U. & Bilbao, R. Characterization of Biomass Chars Formed under Different Devolatilization Conditions: Differences between Rice Husk and Eucalyptus. *Energy Fuels* **22,** 1275–1284 (2008).
153. Xin, S. *et al.* Chemical structure evolution of char during the pyrolysis of cellulose. *J. Anal. Appl. Pyrolysis* **116,** 263–271 (2015).
154. Oschatz, M. *et al.* Nanostructure characterization of carbide-derived carbons by morphological analysis of transmission electron microscopy images combined with physisorption and Raman spectroscopy. *Carbon* **105,** 314–322 (2016).

155. Pré, P. *et al.* A new approach to characterize the nanostructure of activated carbons from mathematical morphology applied to high resolution transmission electron microscopy images. *Carbon* **52,** 239–258 (2013).
156. Kercher, A. K. & Nagle, D. C. Evaluation of carbonized medium-density fiberboard for electrical applications. *Carbon* **40,** 1321–1330 (2002).
157. Shao, Y., Guizani, C., Grosseau, P., Chaussy, D. & Beneventi, D. Thermal characterization and kinetic analysis of microfibrillated cellulose/lignosulfonate blends. *J. Anal. Appl. Pyrolysis* **124,** 25–34 (2017).
158. Rhim, Y.-R. *et al.* Changes in the thermophysical properties of microcrystalline cellulose as function of carbonization temperature. *Carbon* **48,** 31–40 (2010).
159. Parfen'eva, L. S. *et al.* Thermal conductivity of high-porosity biocarbon preforms of beech wood. *Phys. Solid State* **52,** 1115–1122 (2010).
160. Tzeng, S.-S. & Chr, Y.-G. Evolution of microstructure and properties of phenolic resin-based carbon/carbon composites during pyrolysis. *Mater. Chem. Phys.* **73,** 162–169 (2002).
161. Smits, F. . Measurement of sheet resistivities with the four-point probe. *Bell Syst. Tech. J.* **37,** 711–718 (1958).
162. Tsai, W.-T., Liu, S.-C., Chen, H.-R., Chang, Y.-M. & Tsai, Y.-L. Textural and chemical properties of swine-manure-derived biochar pertinent to its potential use as a soil amendment. *Chemosphere* **89,** 198–203 (2012).
163. Yamauchi, S. & Kurimoto, Y. Raman spectroscopic study on pyrolyzed wood and bark of Japanese cedar: temperature dependence of Raman parameters. *J. Wood Sci.* **49,** 235–240
164. Li, X., Hayashi, J. & Li, C.-Z. FT-Raman spectroscopic study of the evolution of char structure during the pyrolysis of a Victorian brown coal. *Fuel* **85,** 1700–1707 (2006).
165. Li, X., Hayashi, J. & Li, C.-Z. Volatilisation and catalytic effects of alkali and alkaline earth metallic species during the pyrolysis and gasification of Victorian brown coal. Part VII. Raman spectroscopic study on the changes in char structure during the catalytic gasification in air. *Fuel* **85,** 1509–1517 (2006).
166. Zhao, Y., Feng, D., Zhang, Y., Huang, Y. & Sun, S. Effect of pyrolysis temperature on char structure and chemical speciation of alkali and alkaline earth metallic species in biochar. *Fuel Process. Technol.* **141, Part 1,** 54–60 (2016).
167. McDonald-Wharry, J., Manley-Harris, M. & Pickering, K. Carbonisation of biomass-derived chars and the thermal reduction of a graphene oxide sample studied using Raman spectroscopy. *Carbon* **59,** 383–405 (2013).
168. Kim, C. *et al.* Raman spectroscopic evaluation of polyacrylonitrile-based carbon nanofibers prepared by electrospinning. *J. Raman Spectrosc.* **35,** 928–933 (2004).
169. Manoj, B. & Kunjomana, A. G. Study of stacking structure of amorphous carbon by X-ray diffraction technique. *Int J Electrochem Sci* **7,** 3127–3134 (2012).
170. Takagi, H., Maruyama, K., Yoshizawa, N., Yamada, Y. & Sato, Y. XRD analysis of carbon stacking structure in coal during heat treatment. *Fuel* **83,** 2427–2433 (2004).
171. Lewis, J. A., Smay, J. E., Stuecker, J. & Cesarano, J. Direct Ink Writing of Three-Dimensional Ceramic Structures. *J. Am. Ceram. Soc.* **89,** 3599–3609 (2006).
172. Sorvari, A. *et al.* Modifying the flocculation of microfibrillated cellulose suspensions by soluble polysaccharides under conditions unfavorable to adsorption. *Carbohydr. Polym.* **106,** 283–292 (2014).
173. Charani, P. R., Dehghani-Firouzabadi, M., Afra, E. & Shakeri, A. Rheological characterization of high concentrated MFC gel from kenaf unbleached pulp. *Cellulose* **20,** 727–740 (2013).

174. Mewis, J. & Wagner, N. J. Thixotropy. *Adv. Colloid Interface Sci.* **147–148,** 214–227 (2009).
175. Zhao, R. H. & Kerekes, R. J. The effect of suspending liquid viscosity on fiber flocculation. *Tappi J.* **76,** 183–188 (1993).
176. Deville, S., Saiz, E. & Tomsia, A. P. Ice-templated porous alumina structures. *Acta Mater.* **55,** 1965–1974 (2007).
177. Deville, S., Saiz, E. & Tomsia, A. P. Freeze casting of hydroxyapatite scaffolds for bone tissue engineering. *Biomaterials* **27,** 5480–5489 (2006).
178. Teng, N.-Y., Dallmeyer, I. & Kadla, J. F. Incorporation of Multiwalled Carbon Nanotubes into Electrospun Softwood Kraft Lignin-Based Fibers. *J. Wood Chem. Technol.* **33,** 299–316 (2013).
179. Snowdon, M. R., Mohanty, A. K. & Misra, M. A Study of Carbonized Lignin as an Alternative to Carbon Black. *ACS Sustain. Chem. Eng.* **2,** 1257–1263 (2014).
180. Deraman, M., Zakaria, S., Omar, R. & Aziz, A. A. Electrical Conductivity of Carbon Pellets from Mixtures of Pyropolymer from Oil Palm Bunch and Cotton Cellulose. *Jpn. J. Appl. Phys.* **39,** L1236 (2000).
181. Lu, X., Nilsson, O. & Pekala, J. F. R. W. Thermal and electrical conductivity of monolithic carbon aerogels. *J. Appl. Phys.* **73,** 581–584 (1993).
182. Sánchez-González, J., Macías-García, A., Alexandre-Franco, M. F. & Gómez-Serrano, V. Electrical conductivity of carbon blacks under compression. *Carbon* **43,** 741–747 (2005).
183. Henriksson, M. & Berglund, L. A. Structure and properties of cellulose nanocomposite films containing melamine formaldehyde. *J. Appl. Polym. Sci.* **106,** 2817–2824 (2007).
184. Quiévy, N. *et al.* Influence of homogenization and drying on the thermal stability of microfibrillated cellulose. *Polym. Degrad. Stab.* **95,** 306–314 (2010).
185. Aulin, C., Gällstedt, M. & Lindström, T. Oxygen and oil barrier properties of microfibrillated cellulose films and coatings. *Cellulose* **17,** 559–574 (2010).
186. Poletto, M., Pistor, V., Zeni, M. & Zattera, A. J. Crystalline properties and decomposition kinetics of cellulose fibers in wood pulp obtained by two pulping processes. *Polym. Degrad. Stab.* **96,** 679–685 (2011).
187. Hokkanen, S., Bhatnagar, A., Repo, E., Lou, S. & Sillanpää, M. Calcium hydroxyapatite microfibrillated cellulose composite as a potential adsorbent for the removal of Cr(VI) from aqueous solution. *Chem. Eng. J.* **283,** 445–452 (2016).
188. Ge, Y., Li, Z., Pang, Y. & Qiu, X. Influence of molecular mass of lignosulfonates on the resulting surface charges of solid particles. *Int. J. Biol. Macromol.* **52,** 300–304 (2013).
189. Jakab, E., Faix, O., Till, F. & Székely, T. The effect of cations on the thermal decomposition of lignins. *J. Anal. Appl. Pyrolysis* **25,** 185–194 (1993).
190. Wang, J. *et al.* Catalytic effects of six inorganic compounds on pyrolysis of three kinds of biomass. *Thermochim. Acta* **444,** 110–114 (2006).
191. Amen-Chen, C., Pakdel, H. & Roy, C. Production of monomeric phenols by thermochemical conversion of biomass: a review. *Bioresour. Technol.* **79,** 277–299 (2001).
192. Várhegyi, G., Till, F. & Székely, T. Software for a mass spectrometer-thermobalance system. *Thermochim. Acta* **102,** 115–124 (1986).
193. van Loon, W. M. G. M., Boon, J. J. & de Groot, B. Qualitative analysis of chlorolignins and lignosulphonates in pulp mill effluents entering the river Rhine using pyrolysis—mass spectrometry and pyrolysis—gas chromatography/mass spectrometry. *J. Anal. Appl. Pyrolysis* **20,** 275–302 (1991).
194. van Loon, W. M. G. M., Boon, J. J. & de Groot, B. Quantitative analysis of sulfonic acid groups in macromolecular lignosulfonic acids and aquatic humic substances by

temperature-resolved pyrolysis-mass spectrometry. *Environ. Sci. Technol.* **27,** 2387–2396 (1993).
195. Grønli, M. G., Várhegyi, G. & Di Blasi, C. Thermogravimetric Analysis and Devolatilization Kinetics of Wood. *Ind. Eng. Chem. Res.* **41,** 4201–4208 (2002).
196. Várhegyi, G., Antal Jr., M. J., Jakab, E. & Szabó, P. Kinetic modeling of biomass pyrolysis. *J. Anal. Appl. Pyrolysis* **42,** 73–87 (1997).
197. McDonald-Wharry, J., Manley-Harris, M. & Pickering, K. A comparison of the charring and carbonisation of oxygen-rich precursors with the thermal reduction of graphene oxide. *Philos. Mag.* **95,** 4054–4077 (2015).
198. Lin-Vien, D., Colthup, N. B., Fateley, W. G. & Grasselli, J. G. *The Handbook of Infrared and Raman Characteristic Frequencies of Organic Molecules*. (Elsevier, 1991).
199. Keiluweit, M., Nico, P. S., Johnson, M. G. & Kleber, M. Dynamic Molecular Structure of Plant Biomass-Derived Black Carbon (Biochar). *Environ. Sci. Technol.* **44,** 1247–1253 (2010).
200. Bohn Lima, R. *et al.* Direct lignin fuel cell for power generation. *RSC Adv.* **3,** 5083–5089 (2013).
201. Mochidzuki, K. *et al.* Electrical and Physical Properties of Carbonized Charcoals. *Ind. Eng. Chem. Res.* **42,** 5140–5151 (2003).
202. Guo, Y. & Bustin, R. M. FTIR spectroscopy and reflectance of modern charcoals and fungal decayed woods: implications for studies of inertinite in coals. *Int. J. Coal Geol.* **37,** 29–53 (1998).
203. McKee, D. W., Spiro, C. L. & Lamby, E. J. The inhibition of graphite oxidation by phosphorus additives. *Carbon* **22,** 285–290 (1984).
204. Mapelli, C., Castiglioni, C., Meroni, E. & Zerbi, G. Graphite and graphitic compounds: vibrational spectra from oligomers to real materials. *J. Mol. Struct.* **480–481,** 615–620 (1999).
205. Brewer, C. E. *et al.* New approaches to measuring biochar density and porosity. *Biomass Bioenergy* **66,** 176–185 (2014).
206. Lehmann, J. *Biochar for Environmental Management: Science and Technology*. (Earthscan, 2012).
207. Kercher, A. K. & Nagle, D. C. Microstructural evolution during charcoal carbonization by X-ray diffraction analysis. *Carbon* **41,** 15–27 (2003).
208. Brown, R. A., Kercher, A. K., Nguyen, T. H., Nagle, D. C. & Ball, W. P. Production and characterization of synthetic wood chars for use as surrogates for natural sorbents. *Org. Geochem.* **37,** 321–333 (2006).
209. Ferrari, A. C. & Robertson, J. Raman spectroscopy of amorphous, nanostructured, diamond–like carbon, and nanodiamond. *Philos. Trans. R. Soc. Lond. Math. Phys. Eng. Sci.* **362,** 2477–2512 (2004).
210. shimodaira, N. Raman spectroscopic investigations of activated carbon materials. *J. Appl. Phys.* **92,** 902–909 (2002).
211. Cuesta, A., Dhamelincourt, P., Laureyns, J., Martínez-Alonso, A. & Tascón, J. M. D. Raman microprobe studies on carbon materials. *Carbon* **32,** 1523–1532 (1994).
212. Zickler, G. A., Smarsly, B., Gierlinger, N., Peterlik, H. & Paris, O. A reconsideration of the relationship between the crystallite size La of carbons determined by X-ray diffraction and Raman spectroscopy. *Carbon* **44,** 3239–3246 (2006).
213. Mattevi, C. *et al.* Evolution of Electrical, Chemical, and Structural Properties of Transparent and Conducting Chemically Derived Graphene Thin Films. *Adv. Funct. Mater.* **19,** 2577–2583 (2009).

214. Liu, X.-Q., Ding, H.-S., Wang, Y.-Y., Liu, W.-J. & Jiang, H. Pyrolytic Temperature Dependent and Ash Catalyzed Formation of Sludge Char with Ultra-High Adsorption to 1-Naphthol. *Environ. Sci. Technol.* **50,** 2602–2609 (2016).
215. Guizani, C., Haddad, K., Limousy, L. & Jeguirim, M. New insights on the structural evolution of biomass char upon pyrolysis as revealed by the Raman spectroscopy and elemental analysis. *Carbon* doi:10.1016/j.carbon.2017.04.078
216. Okumura, Y., Hanaoka, T. & Sakanishi, K. Effect of pyrolysis conditions on gasification reactivity of woody biomass-derived char. *Proc. Combust. Inst.* **32,** 2013–2020 (2009).
217. Paris, O., Zollfrank, C. & Zickler, G. A. Decomposition and carbonisation of wood biopolymers—a microstructural study of softwood pyrolysis. *Carbon* **43,** 53–66 (2005).
218. Frank, O. *et al.* Compression Behavior of Single-Layer Graphenes. *ACS Nano* **4,** 3131–3138 (2010).
219. Huang, M. *et al.* Phonon softening and crystallographic orientation of strained graphene studied by Raman spectroscopy. *Proc. Natl. Acad. Sci.* **106,** 7304–7308 (2009).
220. del Corro, E., de la Roza, A. O., Taravillo, M. & Baonza, V. G. Raman modes and Grüneisen parameters of graphite under compressive biaxial stress. *Carbon* **50,** 4600–4606 (2012).
221. Harris, P. J. F., Liu, Z. & Suenaga, K. Imaging the atomic structure of activated carbon. *J. Phys. Condens. Matter* **20,** 362201 (2008).
222. Liu, T., Luo, R., Qiao, W., Yoon, S.-H. & Mochida, I. Microstructure of carbon derived from mangrove charcoal and its application in Li-ion batteries. *Electrochimica Acta* **55,** 1696–1700 (2010).
223. Aso, H., Matsuoka, K., Sharma, A. & Tomita, A. Structural analysis of PVC and PFA carbons prepared at 500–1000 °C based on elemental composition, XRD, and HRTEM. *Carbon* **42,** 2963–2973 (2004).
224. Li, Z. Q., Lu, C. J., Xia, Z. P., Zhou, Y. & Luo, Z. X-ray diffraction patterns of graphite and turbostratic carbon. *Carbon* **45,** 1686–1695 (2007).
225. Sakintuna, B., Yürüm, Y. & Çetinkaya, S. Evolution of Carbon Microstructures during the Pyrolysis of Turkish Elbistan Lignite in the Temperature Range 700−1000 °C. *Energy Fuels* **18,** 883–888 (2004).
226. Ashby, M. F. *et al. Metal Foams: A Design Guide*. (Elsevier, 2000).
227. Roig, F., Dantras, E., Dandurand, J. & Lacabanne, C. Influence of hydrogen bonds on glass transition and dielectric relaxations of cellulose. *J. Phys. Appl. Phys.* **44,** 045403 (2011).
228. Chen, W. *et al.* Individualization of cellulose nanofibers from wood using high-intensity ultrasonication combined with chemical pretreatments. *Carbohydr. Polym.* **83,** 1804–1811 (2011).
229. Jonoobi, M., Harun, J., Mishra, M. & Oksman, K. Chemical composition, crystallinity and thermal degradation of bleached and unbleached kenaf bast (Hibiscus cannabinus) pulp and nanofiber. *BioResources* **4,** 626–639 (2009).
230. Hokkanen, S. *et al.* Adsorption of Ni(II), Cu(II) and Cd(II) from aqueous solutions by amino modified nanostructured microfibrillated cellulose. *Cellulose* **21,** 1471–1487 (2014).
231. Jonoobi, M., Khazaeian, A., Tahir, P. M., Azry, S. S. & Oksman, K. Characteristics of cellulose nanofibers isolated from rubberwood and empty fruit bunches of oil palm using chemo-mechanical process. *Cellulose* **18,** 1085–1095 (2011).
232. Rosa, M. F. *et al.* Cellulose nanowhiskers from coconut husk fibers: Effect of preparation conditions on their thermal and morphological behavior. *Carbohydr. Polym.* **81,** 83–92 (2010).

233. Lu, H., Gui, Y., Zheng, L. & Liu, X. Morphological, crystalline, thermal and physicochemical properties of cellulose nanocrystals obtained from sweet potato residue. *Food Res. Int.* **50,** 121–128 (2013).
234. Eyholzer, C. *et al.* Preparation and characterization of water-redispersible nanofibrillated cellulose in powder form. *Cellulose* **17,** 19–30 (2010).
235. Gibson, L. J. & Ashby, M. F. *Cellular Solids: Structure and Properties*. (Cambridge University Press, 1999).

6. Appendices

6 Appendices

A: Elemental analysis data of the used NaLS

Element	Concentration (%)
C	40.651
O	44.628
Na	9.043
S	5.325
Others: Mg, Al, Si, Cl, K, Ca	0.353

B.Elemental analysis data of MFC

Element	Molar percentage (%)
C	33.05
H	0.44
N	
O	66.51

(copyright Hokkanen *et al.*[187])

7. Published/submitted papers

7 Published/submitted papers

[1] **Y. Shao**, D. Chaussy, P. Grosseau, D. Beneventi, Use of Microfibrillated Cellulose/Lignosulfonate Blends as Carbon Precursors: Impact of Hydrogel Rheology on 3D Printing, Ind. Eng. Chem. Res. (2015). doi:10.1021/acs.iecr.5b02763.

[2] **Y. Shao**, C. Guizani, P. Grosseau, D. Chaussy, D. Beneventi, Thermal characterization and kinetic analysis of microfibrillated cellulose/lignosulfonate blends, J. Anal. Appl. Pyrolysis. 124 (2017) 25–34. doi:10.1016/j.jaap.2017.03.001.

[3] **Y. Shao**, C. Guizani, P. Grosseau, D. Chaussy, D. Beneventi, Biocarbons from microfibrillated cellulose/lignosulfonate precursors: a study of electrical conductivity development during slow pyrolysis, Carbon, *Under review*

[4] **Y. Shao**, C. Guizani, P. Grosseau, D. Chaussy, D. Beneventi, Use of purely lignocellulosic materials and 3D printing for the development of functional host materials in electrodes of energy storage devices, Bioresource Technol., *Submission*

8. French abstract

8 French abstract

Cette thèse a pour l'objectif d'élaborer, à partir de technologie additive 3D (extrusion de gel), des structures conductrices (électriquement) et résistantes (mécaniquement) en utilisant exclusivement des matériaux lignocellulosiques. Les matériaux sélectionnés sont des microfibrilles de cellulose (MFC), du lignosulfonate de sodium (LS ou NaLS) et de la cellulose en poudre (CP). Ces trois constituants peuvent être utilisés pour élaborer des hydrogels aqueux compatibles avec l'impression 3D (extrusion). De plus, ce procédé d'impression permet la mise en forme avec une excellente définition de structures à base de précurseurs de carbone dont les géométries peuvent être adaptées aux différentes techniques de caractérisation sélectionnées.

Cette thèse a été divisée en 4 parties distinctes

La première concerne l'étude des propriétés rhéologiques des hydrogels de mélanges MFC/LS et leur compatibilité avec le procédé d'extrusion ainsi que la stabilité dimensionnelle des structures 3D imprimées.

Le comportement rhéologique des hydrogels de MFC/LS est présenté sur la Figure 1. En général, les hydrogels sont rhéofluidifiants, ce qui est très favorable pour ce type d'impression 3D. En effet, afin de pouvoir facilement extruder le gel au niveau de la buse d'impression, il est nécessaire que la viscosité du fluide diminue lorsqu'il est sujet à un cisaillement.

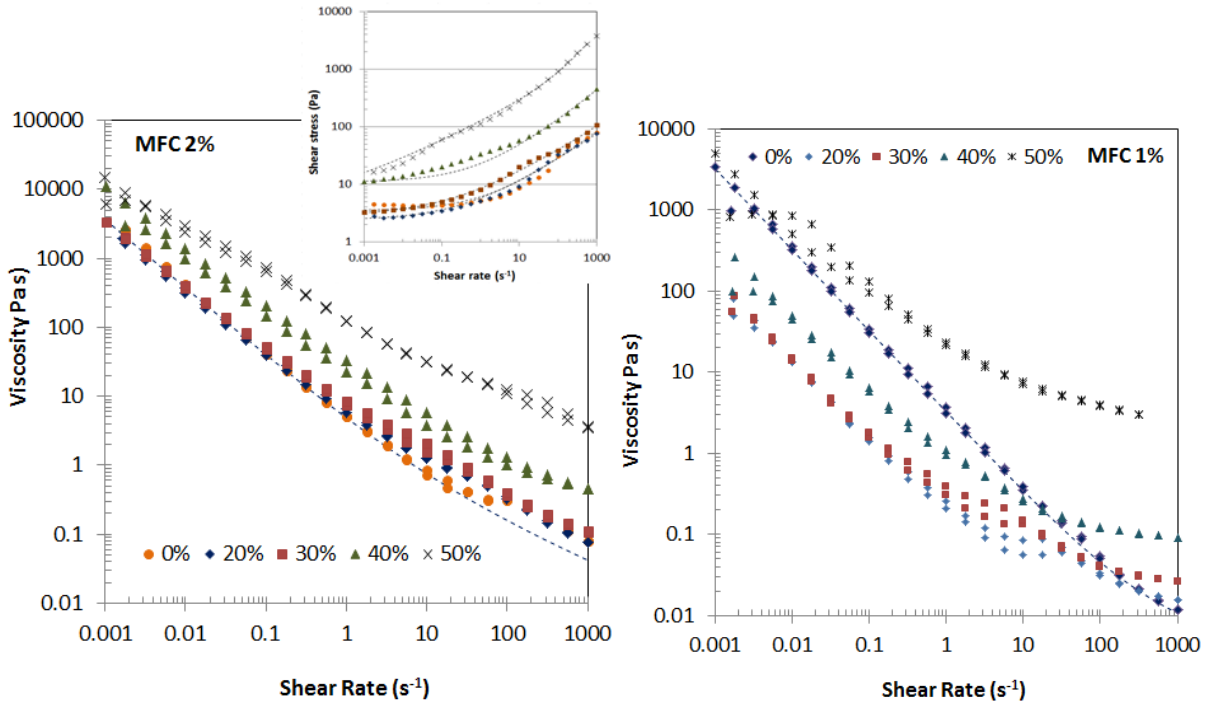

Figure 1 Viscosité en fonction du taux de cisaillement des hydrogels de MFC/LS : a) Série à 2% MFC, la figure insérée représente la contrainte en fonction du taux de cisaillement; b) Série à 1% MFC. Les lignes pointillées représentent les modèles obtenus à partir d'Équation 1et Équation 2.

Équation 1 $$\sigma = \sigma_y + K\dot{\gamma}^n + \eta_s\dot{\gamma}$$

Équation 2 $$\eta = \frac{\sigma_y}{\dot{\gamma}} + nK\dot{\gamma}^{n-1} + \eta_s$$

Dans les conditions d'extrusion, le taux de cisaillement subit par l'hydrogel est d'environ 300 s^{-1}. Pour cette valeur de cisaillement la viscosité correspondante se doit d'être faible. Lorsque l'hydrogel a été déposé sur le substrat et que le cisaillement a disparu, l'hydrogel doit récupérer sa viscosité immédiatement afin d'avoir un comportant solide et éviter un étalement de la matière. Autrement dit, il doit acquérir une viscosité assez élevée quand le cisaillement qu'il subit est petit.

La thixotropie des hydrogels de MFC/LS est présentée sur la Figure 2. Le profil décrit un comportement de restauration du réseau de matière dans l'hydrogel après un changement brutal du taux de cisaillement (i.e. diminution de 1000 à 0.1s^{-1}). La figure 2 montre que pour les hydrogels dont la concentration de LS est inférieure à 30%, la contrainte de cisaillement présente une diminution rapide traduisant une réponse viscoélastique du réseau de MFC à une brusque variation du taux de cisaillement. La constante de temps, obtenue à partir d'Équation 3 , augmente progressivement de 4 à 7 s quand la concentration de LS augmente de 0% à 30%, ce qui signifie que la thixotropie du réseau de MFC diminue lorsque le taux de LS augmente.

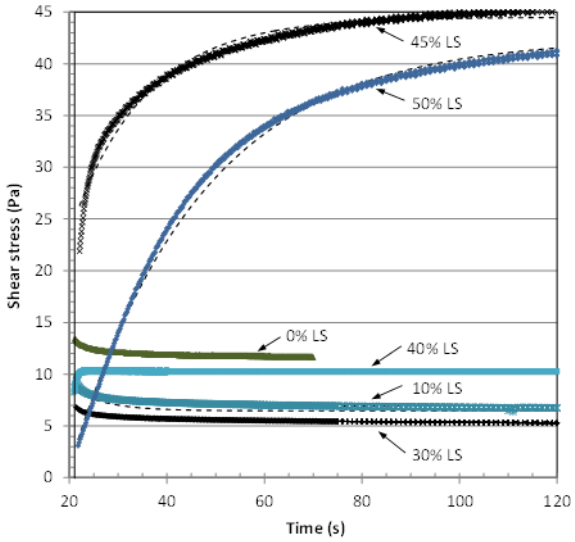

Figure 2 La réponse de la contrainte de cisaillement après une chute brutale du taux de cisaillement de 1000 à 0.1 s^{-1} pour la série de 2% MFC. Les lignes pointillées représentent les résultats de fitting selon Équation 3.

Équation 3 $$\sigma(t) = \sigma_0 + (\sigma_\infty - \sigma_0)\left(1 - e^{-\frac{t}{\tau}}\right) + \eta_s\dot{\gamma}$$

La diminution de la contrainte de cisaillement et son augmentation jusqu'à la stabilisation, observée pour des concentrations de LS au-dessus de 40%, révèle une transition du comportement viscoélastique vers un comportement thixotropique dominé par la composante visqueuse. En raison de la viscosité accrue de la solution de LS, la reconstruction du réseau

MFC est retardée. L'augmentation de la concentration en LS jusqu'à 45% et 50% souligne la réponse thixotropique avec un accroissement de la constante de temps de 0,7 à 14 et 27 s pour des concentration respectives en LS de 40%, 45% et 50%.

Comme l'illustre la Figure 3, des structures cubiques avec une bonne définition spatiale (c'est-à-dire des arêtes vives et sans étalement de la base du cube sur le substrat) ont été imprimées à l'aide de l'hydrogel pur de MFC 2%. Les ajouts de LS ont entraîné une dégradation progressive de la forme souhaitée. Lorsque la concentration en LS augmente de 0 à 30%, la base du cube a tendance à s'étaler et sa hauteur à diminuer d'environ 9 à 2 mm, respectivement. Selon les données expérimentales présentées en Figure 2, ce comportement a été associé à une diminution de la viscosité (de 130 à 60 Pa s) à des taux de cisaillement faibles. Avec 40% de LS, la suspension MFC/LS s'est complètement étalée sur le substrat et l'épaisseur du film liquide final est inférieure à 1 mm. Cette tendance est attribuée à la transition du comportement thixotropique viscoélastique à inélastique. En effet, après le cisaillement dans l'aiguille de l'extrudeuse et la destruction du réseau MFC, la cinétique de reconstruction du réseau est trop lente et la viscosité du fluide trop faible pour empêcher la suspension MFC / LS de se répandre sur le substrat d'impression. Avec 50% de LS, les structures cubiques sont facilement imprimées sans déformations majeures. Cependant, leurs arêtes présentent des profils arrondis, indiquant un phénomène de fluage au sein de la suspension MFC/LS.

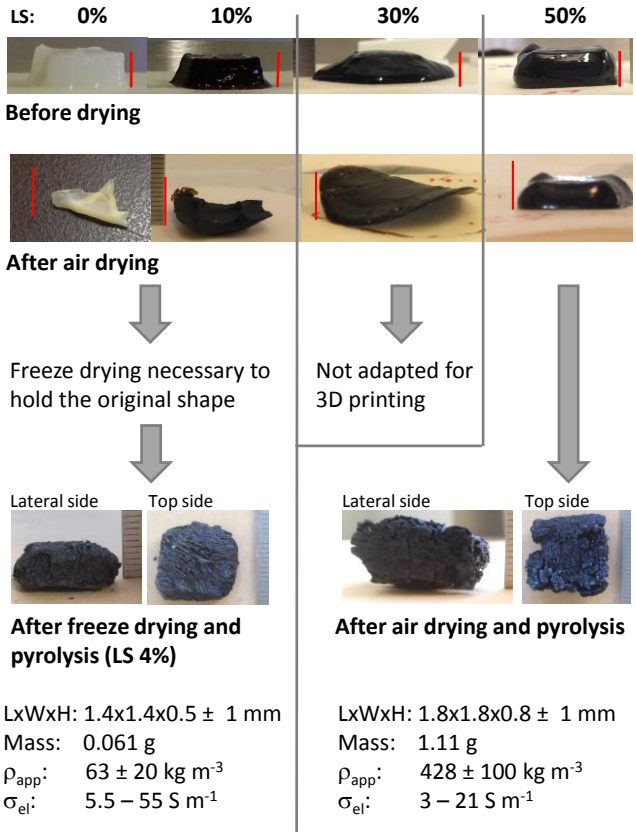

Figure 3 : Photographies et principales caractéristiques des structures cubiques avant et après séchage et pyrolyse.

La seconde partie de cette étude s'intéresse à l'analyse de la dégradation thermique des précurseurs de carbone de MFC/LS ainsi qu'à leur cinétique de décomposition durant la pyrolyse à haute température qui permet d'amorcer la formation de structure de graphite.

Au cours de cette étude les MFC et NaLS ont été caractérisés séparément et en mélanges en termes de morphologie, de structure chimique et de stabilité thermique. Des différences importantes ont été observées entre ces deux matériaux dans tous les domaines principalement en raison de leur composition et de leur structure chimique différente. Selon la Figure 4a) et b), les MFC se dégradent intensivement dans une plage de température étroite comprise entre 250 °C et 350 °C, tandis que le NaLS se décompose beaucoup plus doucement dans 2 gammes de températures principales, 150°C- 500°C et 600°C - 800°C.

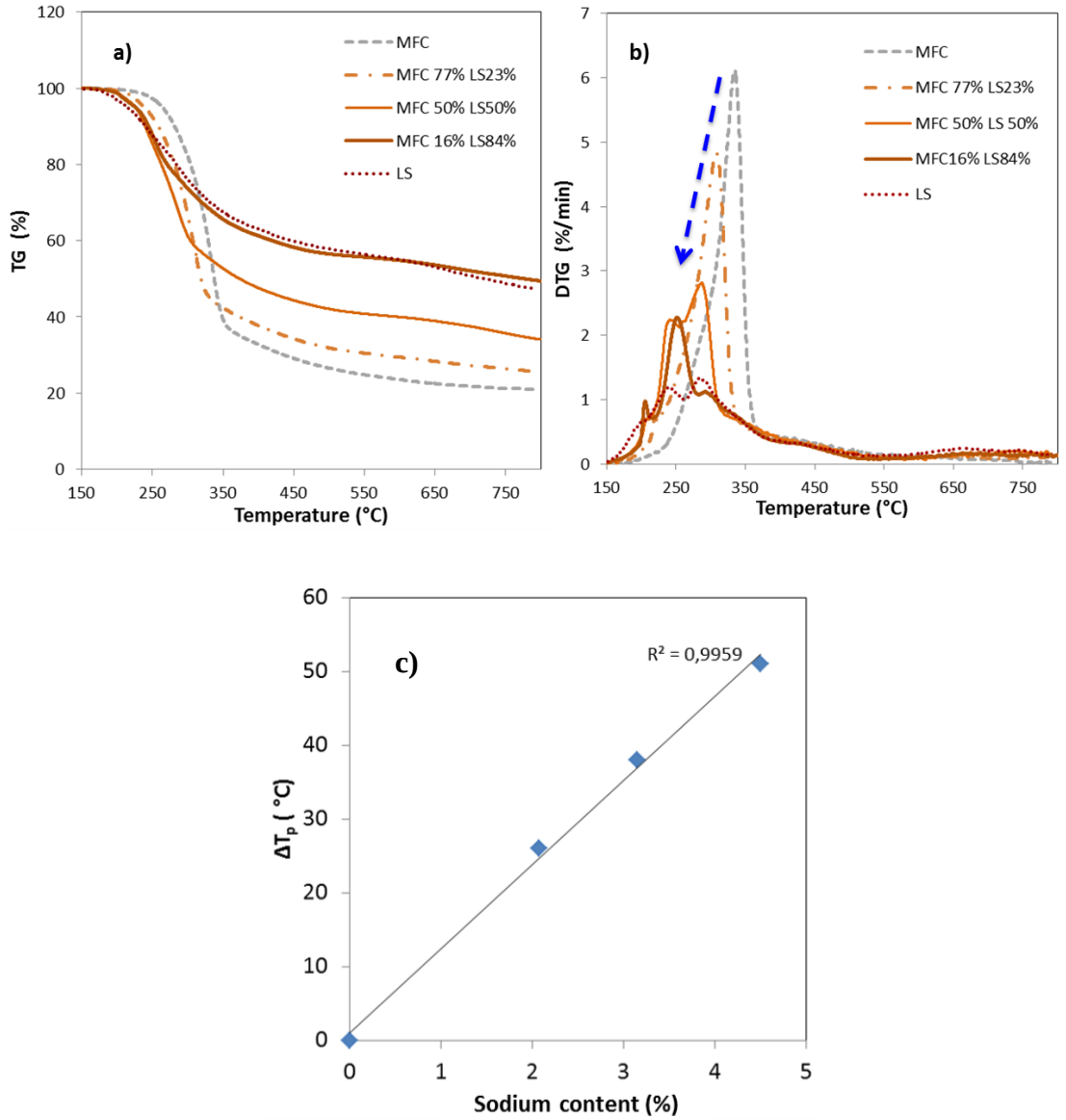

Figure 4 : a) TG et b) DTG de MFC, NaLS (ou LS) et des mélanges (la flèche indique le décalage du pic caractéristique de la cellulose ; c) Influence de la teneur en sodium sur ΔT_p pour les mélanges MFC/LS.

En outre, l'analyse cinétique des MFC et du NaLS a été menée avec deux approches basées sur le modèle et sans modèle. Ce dernier suggère des paramètres d'Arrhenius trop élevés pour être utilisés afin de reproduire la courbe expérimentale. Cependant, l'approche avec le modèle permet de reproduire correctement la courbe expérimentale en fournissant des paramètres de dégradation thermique des MFC tout à fait compatibles avec les données de la littérature (Table. 1). L'analyse cinétique de la dégradation thermique de NaLS est réalisée ici pour la première fois en fournissant un ensemble de données cinétiques qui permettent de prédire le comportement thermique de ce matériau (Table. 2). De plus, les courbes DTG, qui représentent la décomposition des composés MFC / NaLS mélangés dans divers rapports, ne combinent pas "linéairement" les modèles des deux matériaux en raison de la présence de la teneur en sodium. L'effet catalytique du sodium est confirmé par une relation fortement corrélée entre ΔT_p et la teneur en sodium (Figure 4c)) ainsi qu'expérimentalement par le comportement thermique du mélange MFC/NaCl. D'un point de vue cinétique, une telle diminution des températures de réaction pourrait être interprétée comme une diminution de l'énergie d'activation des pseudo-composants de MFC dans les composés. En utilisant des pseudo-composants moins élevé pour MFC, un fitting efficace a été atteint pour deux composites MFC / NaLS en suivant une règle de superposition pondérée.

Table. 1: Paramètres d'Arrhenius pour les 4 pseudo-composants de MFC

Pseudo-composants	1	2	3	4
Proportion	0.22	0.51	0.18	0.09
E_a (KJ/mol)	137	229	46	52
logA (log(s^{-1}))	23.7	40.3	1.5	0.1

Table. 2 Paramètres d'Arrhenius pour les 6 pseudo-composants de NaLS

Pseudo-composants	1	2	3	4	5	6
Proportion	0.05	0.17	0.19	0.15	0.24	0.20
E_a (KJ/mol)	149	112	132	104	45	72
LogA (log(s^{-1}))	33	21	23	15	1.2	2

Une troisième étude est destinée à la caractérisation des bio-carbones de MFC/LS en fonction de la température de la pyrolyse. En effet, cette dernière joue un rôle essentiel sur certaines propriétés des carbones, telle que la densité, la microstructure et la conductivité électrique.

Un large éventail de températures de traitement thermique (HTT de 400 à 1200 °C) a été exploré pour la synthèse des biocarbones afin de mieux comprendre l'évolution de leurs propriétés morphologiques et microstructurales et, plus important, leurs propriétés électriques. Les carbones MFC / LS se sont révélés résistants à la chaleur et morphologiquement stables à la pyrolyse lente. Les résultats de FTIR sur les carbones MFC / LS ont fourni des éléments tangibles concernant la perte de la majorité des groupes fonctionnels pendant le traitement thermique. De plus, seulement quelques structures contenant de l'oxygène ont été retenues à partir de la pyrolyse à haute température. La caractérisation microstructurale par Raman a révélé que les carbones résultants sont composés de : i) des grappes de graphène (régulières) sans défaut (3 couches de graphène, selon les mesures XRD); ii) des structures de graphène avec défauts (principalement oxygène) et iii) des phases amorphes. Les résultats XRD permettent de percevoir directement la croissance de grappes de graphène régulières avec des HTT élevées tandis que les rapports de Raman (I_D/I_{total}, I_G/I_{total} et I_D/I_G) permettent de comprendre les changements relatifs des trois phases. En raison de la croissance des phases conductrices (régulières et avec défauts) en plus de la réduction des phases isolantes (amorphe), une augmentation générale de la conductivité électrique a été observée dans les carbones durs de MFC / LS en fonction des HTT bien que les mécanismes pour le développement de la conductivité ne soit pas identiques pour les différentes gammes de température (Figure 5):

i : 400 °C ≤ HTT ≤ 600 °C: les chars possèdent à cet état déjà des grappes de graphène réguliers en petite taille (2.135 nm), comme en témoignent les résultats de XRD. Cependant, ils sont complètement isolés par des structures de graphéne 'défectueuses' (détectées par la bande de Raman D) et les structures amorphes (bande de Raman V, S et Gr). Cette dernière est plus importante par rapport aux deux antérieures. Ainsi, les sauts d'électrons et l'effet tunnel sont empêchés ou largement réduits. Par conséquent, la conductivité est indétectable ou assez faible (Figure 5a)).

ii : 600 °C <HTT <700 °C: la phase amorphe continue de se réduire et participe ainsi au développement des phases structurées. Atteignant un seuil de percolation, cettes dernières se mettent en contact, ce qui favorise le mouvement des électrons en grande partie. Par conséquent, la conductivité est nettement améliorée. Cependant, la phase de graphène 'défectueuse' étant beaucoup plus importante que celle de la phase de graphène régulière dans les carbones MFC / LS (ce qui est attesté par le rapport Raman D / G toujours supérieur à 1), on peut supposer que les voies électriques sont construites plus probablement par des contacts entre les grappes de graphène défectueux (Figure 5b)).

iii : 700 °C ≤ HTT ≤ 1000 °C: pendant cette période, les structures de graphène régulières et défectueuses continuent de croître en taille et en nombre, en intensifiant les contacts mutuels entre les grappes conductrices. Par conséquent, la conductivité électrique est renforcée (Figure 5c)).

iv : HTTs> 1000 ° C: une fois la connexion électrique établie, une graphitisation renforcée ou une réduction supplémentaire des défauts n'entraînera pas d'augmentation importante des contacts entre les phases conductrices et un palier de la conductivité électrique induite par HTT sera atteint (Figure 5d).

Malgré l'augmentation de la porosité pendant le traitement thermique (>400°C), les conductivités apparentes des carbones MFC/LS sont fortement améliorées. Cet effet montre bien que l'augmentation de la conductivité intrinsèque de carbone domine sur le développement de la porosité.

Après la carbonisation à 1000 ° C, les biocarbones des précurseurs de MFC / LS sont toujours sous la forme de feuilles autoportées et peuvent présenter une conductivité électrique assez intéressante (95 S / cm) par rapport à leur densité relativement faible de 1,14 g / cm^3. Les propriétés physiques mentionnées ci-dessus sont nettement supérieures par rapport aux propriétés de biocarbones publiées dans la littérature.

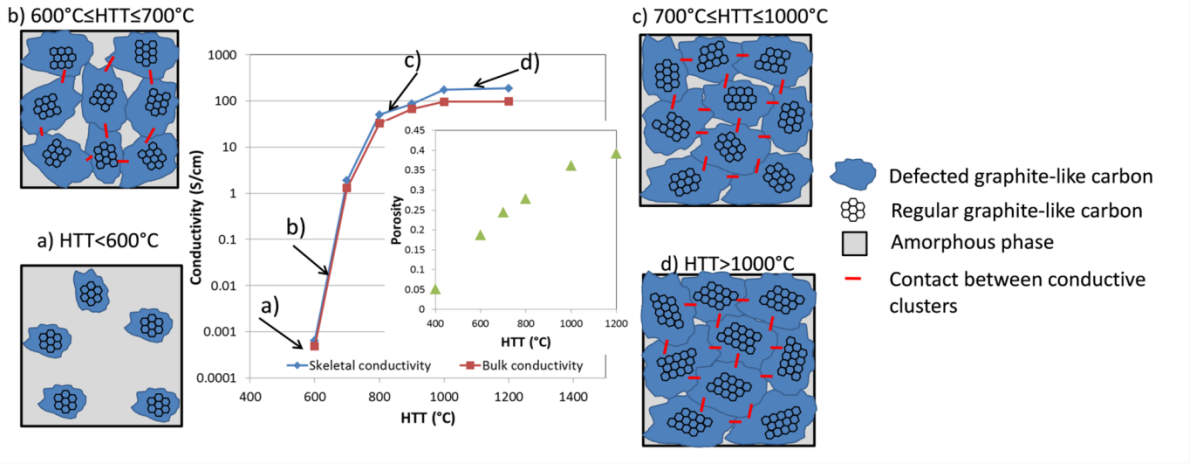

Figure 5 : Modèle permettant d'interpréter le développement de la conductivité électrique dans les carbones MFC/LS.

La dernière étude de cette thèse résume les 3 études précédentes et examine l'utilisation de mélanges de microfibrilles de cellulose / Lignosulfonate / poudre de cellulose référencés MFC/LS/CP en tant que précurseur de carbone aussi bien en termes de comportement rhéologique durant le procédé d'extrusion que de dégradation thermique durant la pyrolyse. Les carbones issus des mélanges MFC/LS/CP sont alors caractérisés comme dans la section précédente. La figure 6 synthétise l'ensemble des opérations réalisées dans cette section.

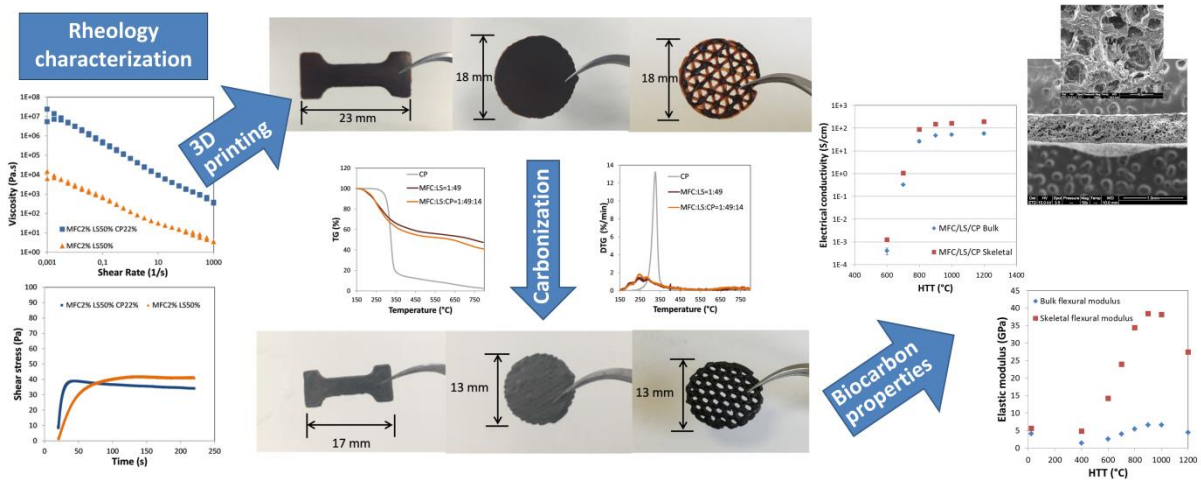

Figure 6 Utilisation de systèmes MFC/LS/CP comme précurseur de carbone : caractérisation du comportement rhéologique jusqu'aux propriétés finales des carbones

Comme précédemment, des structures de carbone conductrices (électriquement) et résistantes (mécaniquement) ont été élaborées par impression 3D puis pyrolysées. La processabilité des 'slurry' de MFC / LS / CP par l'impression en 3D a été examinée par des tests rhéologiques en mode flow et thixotropique. Les objets imprimées sont autoportés avec une définition d'impression élevée et se sont avérés morphologiquement stables au séchage à l'air ainsi qu'après l'opération de pyrolyse. Des mesures de TGA / DTG ont été effectuées pour caractériser la dégradation thermique des composants individualisés ainsi que des mélanges MFC / LS / CP. Les carbones résultants ont été ensuite caractérisés en termes de morphologie, de microstructure et de propriétés physiques (comme la densité, la conductivité électrique et la résistance mécanique). À 900 °C, les carbones MFC / LS / CP présentaient une conductivité électrique élevée de 47,8 S / cm avec une faible densité de 0,74 g / cm^3 ainsi qu'une porosité importante de 58%. Ils ont également atteint un module d'élasticité maximal de 6,62 GPa. Ces propriétés électriques et mécaniques peuvent ainsi conduire à utiliser dans un proche avenir ces biocarbones dans des dispositifs de stockage d'énergie, en tant que matériaux actifs d'électrode.

En conclusion, ces trois années de travail ont permis l'élaboration de structures de carbone fonctionnelles qui pourraient être utilisées commet réseau conducteur dans les électrodes de dispositif de stockage d'énergie. Grâce à une porosité contrôlable, une faible densité ainsi qu'une conductivité électrique élevée, ce matériau apparait comme un candidat idéal pour la fabrication d'électrodes structurées à haute capacité spécifique. En outre, ce travail propose une nouvelle façon d'élaborer des électrodes en utilisant le procédé d'impression 3D. À

l’avenir, les électrodes pourraient être imprimées directement en utilisant une imprimant 3D à deux têtes : l’une pour imprimer le matériau ‘d’accueil’ l’autre pour déposer des composants actifs. Par ailleurs, ces travaux de thèse permettent de promouvoir l’utilisation de matériaux lignocellulosiques dans les dispositifs de stockage d’énergie comme ‘matériaux actifs’.